Helicopter-borne ground-penetrating radar surveying of temperate Alpine glaciers

Doctoral Thesis

Author(s):
Langhammer, Lisbeth

Publication date:
2018

Permanent link:
https://doi.org/10.3929/ethz-b-000328361

DISS. ETH NO. 25412

Helicopter-borne ground-penetrating radar surveying of temperate Alpine glaciers

A thesis submitted to attain the degree of

DOCTOR OF SCIENCES of ETH ZURICH
(Dr. sc. ETH Zurich)

presented by

LISBETH LANGHAMMER

Master of Science in Geosciences, University of Oslo
born on 23.08.1988
citizen of Germany

accepted on the recommendation of

Prof. Hansruedi Maurer	ETH Zurich	Examiner
Dr. Andreas Bauder	ETH Zurich	Co-Examiner
Dr. Lasse Rabenstein	Drift & Noise Polar Services	Co-Examiner
Prof. Johan O.A. Robertsson	ETH Zurich	Co-Examiner
Dr. Jack Kohler	Norwegian Polar Institute	Co-Examiner

2018

Abstract

Alpine glaciers are considered to be persisting formations in high mountain landscapes. However, they are in a constant state of motion and transformation. To understand the past, present and future change of glaciers, gaining knowledge about surface and subsurface glacier structures is fundamentally important. Geophysical methods, such as ground-penetrating radar (GPR), are excellent to investigate these structures. By utilizing electromagnetic wave propagation, GPR systems record changes in the geophysical subsurface properties. For example, GPR radargrams can be interpreted to infer the ice thickness. In this study, I demonstrate how traditional GPR methods can be advanced to survey Alpine glacier more efficiently, and how the recorded data can be exploited to derive three-dimensional ice thickness maps.

To investigate the discrepancies in bedrock reflection quality of the GPR data recorded in previous glacier campaigns, I performed an extensive ground-based test with different GPR systems, center frequencies and antenna dipole orientations on the Otemma Glacier in Switzerland. The comparison of the individual setups revealed that independent of the GPR system or center frequencies used in the test campaign, the quality of the bedrock reflection changes with the orientation of the dipole axis. Results of numerical models of the Otemma Glacier with homogeneous glacier ice display very similar behavior. A more coherent and enhanced bedrock reflection can be observed when the dipole antennas are aligned parallel to the strike direction of the surrounding valley walls. In the glacier tongue area, the general subsurface topography can be well predicted, and the axis of GPR antennas can be orientated appropriately, but in saddle regions and convergence zones with undulating subsurface topography the shape is less predictable. Therefore, I recommend multi-component recordings using two orthogonal antenna pairs in broadside configuration.

Depending on the electromagnetic properties of the material surrounding the dipole antennas, the radiation pattern of the electromagnetic waves exhibits a high degree of directionality. I assessed analytically and numerically the radiation patterns for different heights of the GPR antennas above an ice-air interface to reconstruct how airborne GPR acquisition influences the signal amplitude distribution. By lifting low-frequency antennas of the ground up to an average flight height of below 40 m, the radiation pattern neither correspond to a full-space nor a half space analytical solution and high amplitude lobes persist. The directionality can be decreased by summing the received GPR signals of a multicomponent antenna system, as suggested by the pseudo-scalar wave field approach.

Based on these observations and with the aim of reducing cost and extensive manual labor for ground-based field work, the dual-polarization, helicopter-borne AIR-ETH (Airborne Ice Radar) GPR system was developed. It is equipped with two sets of low-frequency antennas mounted perpendicular to each other. The system is built with commercial components and thus fully reproducible. With this novel helicopter-based acquisition system more than 600 km of GPR profiles have been recorded over the Swiss glaciers during the past two years. This large data set has been analyzed with custom-built Matlab processing routines, which are based on standard processing steps and specifically improved to support the helicopter-borne recorded data. Using the example of the Plaine Morte and Oberaletsch Glacier, I demonstrate that summing the data of both GPR channels of the AIR-ETH system enhances the coherency and visibility of the bedrock reflections in comparison to traditional single direction antenna configurations.

To utilize the recorded GPR ice thickness data to its full potential, the GlaTE (Glacier Thickness Estimation) inversion algorithm was developed. The method combines physical modeling and data constraints to derive the three-dimensional ice thickness distribution of the surveyed glaciers. The GPR measurements constrain the absolute thickness and a glaciological mass conservation model is used to force the overall distribution. Smoothing constraints and glacier boundaries complement the inversion. With this methodology, I calculate the ice thickness distribution of the Morteratsch, Oberaletsch, Plaine Morte and smaller glaciers in the Dom region as an example for the varying glacier types in the Swiss Alps. When the comprehensive GlaTE inversion output is compared to the traditional glaciological mass conservation model results, it becomes apparent that the results of the GlaTE inversion are more precise because it incorporates observational data as constraints.

Often, the trajectory of GPR survey profiles are chosen arbitrarily before a field campaign. This procedure can be improved with the GlaTE inversion and sequential optimized experimental design (SOED). The SOED results show that less than half of the previously acquired GPR profiles are necessary to constrain the inversion so that an appropriate representation of the comprehensive thickness model can be produced. For narrow valley-glaciers longitudinal profiles are essential and outperform the sole recording of several across profile. However, in wider section of the glacier, additional across profiles add valuable ground-truth information.

The presented investigations and achieved results in this study substantially impact the field of ground-penetrating radar research on Alpine glaciers. With the novel helicopter-borne GPR acquisition unit, the optimized survey planning, advanced processing routines and the ice thickness estimation inversion, a complete set of tools have been developed to assess the glacier mass in the Swiss Alps and in other high-mountain regions.

Zusammenfassung

Alpengletscher gelten als beständige Giganten in der Hochgebirgslandschaft der Schweiz, jedoch verändern und prägen sie ihre unmittelbare Umgebung und sind in ständiger Bewegung. Um die Veränderungen der Gletscher in der Vergangenheit, Gegenwart und Zukunft zu verstehen, ist es von grundlegender Bedeutung, Kenntnisse über ihre Oberflächen- und Untergrundstruktur zu gewinnen. Geophysikalische Methoden wie das Bodenradar eignen sich hervorragend, um die Dicke von Gletschern zu messen. Bodenradarsysteme erfassen die Veränderungen in den geophysikalischen Eigenschaften des Untergrundes, die durch Schwankungen in der Amplitude von elektromagnetischen Wellen sichtbar werden. In dieser Arbeit stelle ich vor, wie traditionelle Bodenradarmethoden weiterentwickelt werden können, um Alpengletscher effizient zu untersuchen. Darüber hinaus wird gezeigt, wie boden- und luftgestützte Radardaten genutzt werden können, um dreidimensionale Eisdickenkarten zu erstellen.

In vorangegangenen Studien wurde festgestellt, dass die Amplituden der reflektierten elektromagnetischen Wellen von der Unterseite des Gletschereises starke räumliche Unterschiede aufweisen können. Zur Analyse dieser Aussagen führte ich einen umfangreichen bodengestützten Test mit verschiedenen Bodenradarsystemen, Mittenfrequenzen und Antennendipolorientierungen auf dem Otemma Gletscher in der Schweiz durch. Der Vergleich der einzelnen Komponenten ergab, dass sich die Qualität der Untergrundreflexion mit der Ausrichtung der Dipolantennenachse unabhängig von den verwendeten Bodenradarsystemen bzw. Mittenfrequenzen signifikant verändert. Resultate von numerischen Modellen des Otemma Gletschers mit homogenem Gletschereis bestätigen diese Beobachtung. Wenn die Dipolantennen parallel zur Streichrichtung der den Gletscher umgebenden Talwände ausgerichtet sind, kann eine kohärentere und verstärkte Reflexion des Gesteins beobachtet werden. Um die Datenqualität im Bereich der Gletscherzunge zu verbessern, sollte die Achse der Bodenradarantennen parallel zur Gletscherfließrichtung ausgerichtet werden. In Sattelregionen und Konvergenzzonen mit unebener Topographie ist die Untergrundtopographie weniger genau vorhersagbar. Für diese Bereiche empfehle ich den Einsatz eines Bodenradarsystems mit mehreren Antennenkonfigurationen und unterschiedlichen Dipolausrichtungen.

In Abhängigkeit von den elektromagnetischen Eigenschaften des Materials, das die Dipolantennen umgibt, weist das Strahlungsmuster der elektromagnetischen Wellen eine hohe Richtungsabhängigkeit auf. Bestandteil der vorliegenden Arbeit ist die Datenanalyse und die numerische Modellierung des Strahlungsmusters für verschiedene Höhen der Bodenradarantennen über einer Eis-

Luft-Grenzfläche, um zu rekonstruieren, wie luftgestütztes Bodenradar die Amplitudenverteilung beeinflusst. Werden niederfrequente Bodenantennen bis auf eine niedrige Flughöhe angehoben, entspricht das Strahlungsmuster weder einer vollräumigen noch einer halbräumigen analytischen Lösung und ausgeprägte Bereiche mit sehr hoher Amplitude bleiben bestehen. Die inhomogene Amplitudenverteilung kann reduziert werden, indem die empfangenen Bodenradarsignale eines Mehrkomponentenantennensystems mit Hilfe des pseudoskalaren Wellenfeldprinzips summiert werden.

Ausgehend von diesen Beobachtungen und mit dem Ziel, Kosten und Zeit für Bodenradar-Felduntersuchungen zu reduzieren, wurde das hubschraubergestützte Doppelpolarisationssystem AIR-ETH (Airborne Ice Radar) entwickelt. Es ist mit zwei senkrecht zueinander montierten Niederfrequenzantennen ausgestattet. Das System besteht aus kommerziellen Komponenten und kann vollständig reproduziert werden. Mit der hubschrauberbasierten Datenaufnahme wurden allein in den letzten zwei Jahren mehr als 600 km Bodenradarprofile über den Schweizer Gletschern erfasst. Für die vorliegende Arbeit wurde der umfangreiche Datensatz dieser Messungen mit adaptierten MATLAB-Verarbeitungsroutinen analysiert. Die Prozessierungsschritte basieren auf Standardverfahren und wurden speziell für die Analyse der hubschraubergestützten Daten erweitert. Am Beispiel des Plaine Morte und des Oberaletsch Gletschers wird demonstriert, dass die Addition der Signale von beiden Radarkanälen des AIR-ETH Systems die Kohärenz und die Sichtbarkeit der Untergrundreflexionen im Vergleich zu herkömmlichen Konfigurationen mit einem Antennenpaar verbessert.

Zur Beschreibung und Darstellung einer dreidimensionalen Eisdickenverteilung der Schweizer Gletscher wurde der GlaTE (Glacier Thickness Estimation) Inversionsalgorithmus entwickelt. Die einbezogenen Parameter stammen sowohl aus Bodenradarmessungen, die die absolute Eisdicke festlegen als auch von einem glaziologischen Massenerhaltungsmodell, mit dem die generelle Verteilung des Eises bestimmt wurde. Bei der Definition weiterer Randbedingungen für die Inversion wurde die Glättung von Unebenheiten im Untergrund und die Begrenzung des Gletschers in seiner realen Ausdehnung berücksichtigt. Mit Hilfe der Inversionsmethode konnte die Eisdickenverteilung vom Morteratsch, Oberaletsch, Plaine Morte und kleineren Gletschern in der Dom-Region berechnet werden und somit unterschiedliche Gletschertypen in den Schweizer Alpen repräsentiert werden. Im Vergleich der Ergebnisse der GlaTE-Inversion mit den Resultaten der traditionellen, glaziologischen Massenerhaltungsmethode wird sichtbar, dass die Inversionsresultate die Eisdickenverteilung genauer abbilden. Die verbesserte Genauigkeit der Analysen ist auf die Einbeziehung der Bodenradardaten als zusätzlicher reeller Parameter zurück zu führen.

Bevor Radarmessungen auf einem Gletscher durchgeführt werden, wird die Lage der Profile häufig beliebig gewählt. Dieses Vorgehen kann mit Hilfe des GlaTE-Inversionsalgorithmus und einer Sequentiell Optimiertes Experimentelles Design (SOED) Methode optimiert werden. Die SOED-

Ergebnisse zeigen, dass weniger als die Hälfte der zuvor erfassten Bodenradarprofile notwendig sind, um eine sehr genaue Eisdickenverteilung des Gletschers zu erzeugen. Aus den vorliegenden Analysen kann geschlussfolgert werden, dass Längsprofile entlang von schmalen Talgletschern effektiver sind als mehrere Querprofile um die Dickenverteilung des Gletschers kosteneffizient abzubilden. Nichtsdestotrotz sind Querprofile sehr wertvoll, wenn die Gletscheroberfläche in der Breite zunimmt.

Die vorgestellten Untersuchungsmethoden und erzielten Ergebnisse in dieser Studie tragen wesentlich zu neuen Erkenntnissen in der Bodenradarforschung auf Alpengletschern bei. Mit dem neuartigen helikoptergestützten Bodenradarsystem, der optimierten Feldplanung, verbesserten Prozessierungsmethoden und der Inversion für die Eisdickenabschätzung wurden im Rahmen dieser Arbeit neue Werkzeuge entwickelt, um die Masse der Gletscher in den Schweizer Alpen und in anderen Hochgebirgsregionen mit höherer Genauigkeit zu bestimmen.

Contents

List of Figures

List of Tables

Chapter 1

General Introduction

1.1 Motivation

In 2010, 2.3% of Switzerland's territory was covered with glacier ice (Fischer et al., 2014; EDA Präsenz Schweiz, 2017). Compared to the total area of the country, the extent of the glaciated terrain seems to be negligible. However, glaciers substantially influence their direct natural environment and humans living in their vicinity or downstream regions.

Environmental effects range from periodically varying meltwater runoff (Farinotti et al., 2012), impacts on the local climate (Van den Broeke, 1997) to catastrophic glacial outburst floods caused by rapid meltwater release and destabilizing the static support of surrounding mountain slopes (Richardson and Reynolds, 2000). Economically, mountain glaciers and glacierized catchments act as fresh water storage at high altitudes and provide an input in the form of meltwater run-off for hydropower reservoirs (Finger et al., 2012; Schaefli et al., 2007). In Switzerland, 56% of the total generated energy is based on hydropower. Pump storage stations and river power plants are essential for the local and regional energy production (Pfammatter and Piot, 2014).

Therefore, reliable predictions of future meltwater runoff and models of fresh water availability are necessary to secure the production of renewable energy by hydropower. Based on glacier models, Braun et al. (2000), Farinotti et al. (2012), Gabbi et al. (2012), Linsbauer et al. (2013), and Oerlemans et al. (1998) have shown that the change towards a warming and drying climate causes glacier mass shrinkage at high altitudes. Gabbi et al. (2012) showed that after a first minor increase in meltwater runoff, the inflow into the drainage networks will decrease substantially during the summer months in the next century.

To predict the glacier behavior and meltwater production for the next decades or centuries with glacier models, the mass balance, geometry and ice rheology as well as glacier flow laws have to be considered in the modeling process. The glacier mass balance is highly dependent on meteorological factors such as the amount and type of precipitation, temperature and wind patterns as well as the energetic components of the surface energy balance. Monitoring of surface parameters with automatic weather stations, snow pits, mass balance stakes and satellite imagery or radar is widely used to assess the current state of glaciers around the world (Bamber and Kwok, 2004; Benn and Evans, 2010; DeWalle and Rango, 2008; Hagen and Reeh, 2004). The glacier geometry, bedrock topography, slope and exposition determine the response time of the ice mass to changing climatic conditions (Cuffey and Paterson, 2010). However, determining the exact volume of the ice mass remains difficult due to the lack of subsurface information.

To overcome these difficulties, geophysical methods, such as ground-penetrating radar (GPR), can be applied to explore the glacier interior and subglacial topography. It offers the possibility to be operated ground-based as well as airborne, because of inductive coupling. GPR is a non-destructive and logistically inexpensive technique to measure the thickness of high-altitude glaciers and their subsurface topography.

In 2014, the Swiss-wide glacier mapping project was initiated to establish a comprehensive data base of glacier bedrock topography and ice mass data base. This lays a foundation for accurate glacier mass prediction models and will help to identify future hydropower sites in the Alps. One goal of the project is the development of a novel helicopter-borne GPR measuring system, which can be applied to a variety of environmental settings. Further details about the project can be found in Section 1.6

1.2 Alpine glaciers in Switzerland

Glaciers are ice masses, which move due to their own weight and their shape is constrained by the surrounding topography (Dobhal, 2014). Depending on the extent of ice masses, they are referred to as ice caps (e.g. Vatnajökull Ice Cap in Iceland) or ice sheets such as the Greenland and Antarctic Ice sheet (Graham, 2011). However, the structural ice composition and occurring periglacial features, such as moraines, are similar for all ice masses.

Generally, glaciers are subdivided into an accumulation zone at higher elevations, where mass gain exceeds mass loss and an ablation zone at lower elevations, where mass loss is the dominating process (Figure 1.1). The transition line between the accumulation and ablation zone of equal mass loss and gain is defined as the equilibrium line. Common types in the Swiss Alps are valley (Figure 1.1), cirque and hanging-type glaciers. Most glaciers in the Alps consist of temperate ice, which in contrast to cold ice, has a temperature close to the melting point of 0°C at atmospheric pressure. As a consequence, water can be present supra- (at the surface), eng- (inside the glacier) and subglacial (below the glacier) throughout the year (Fountain, 2014).

The number of 1420 glaciers were counted to exist in Switzerland in 2010 (Fischer et al., 2014). Around 88% of them are equal to or smaller than 1 km^2, while only 16 glaciers span an area larger than 10 km^2, e.g. the Great Aletsch Glacier (78.4 km^2 in 2010, Fischer et al., 2014) and the Rhone Glacier (15.6 km^2 in 2015, Bauder, 2017). The majority of the Swiss glaciers is situated in the mountain chains along the Rhône river, the northern Alpine Crest (Bernese Alps) and the main Alpine Crest (Valais Alps) shown in Figure 1.2, Fischer et al., 2014; Maisch et al., 2000).

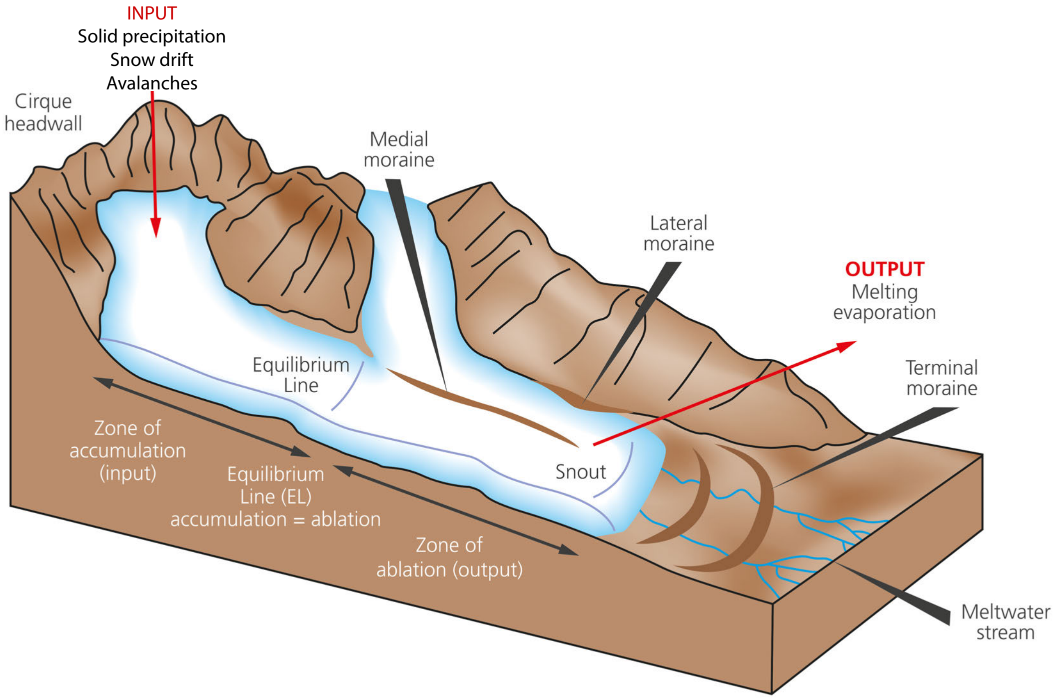

Figure 1.1: Illustration of a typical valley glacier with dominant glacial features. Modified after Sigurðsson (2018).

1.3 Ground-penetrating radar

It is rumored that the interest in applying radar as subsurface mapping tool for ice masses originated after World War II, since it was reported that military airplanes had difficulties measuring the exact height over the Greenland ice sheet with their radar instruments. It could be explained by the low conductivity of ice and the penetration of the electromagnetic (EM) waves into the subsurface (Evans, 1963; Nobes, 2014; Waite and Schmidt, 1962). Since the 1950s, RADAR (RAdio Detection And Ranging) techniques (e.g radio echo soundings) have been used as a geophysical method to investigate the thickness and subsurface conditions of ice masses (Cook, 1960; Harrison, 1970; Steenson, 1951). Nowadays, commercially available GPR systems with short duration pulses are based on the technology developed in the 1970s (Annan, 1973). A more detailed overview of GPR applications on glaciers is given in Section 1.5 as well as in Nobes (2014), Plewes and Hubbard (2001), and Woodward and Burke (2007).

Resistively loaded dipole antennas are used to radiate electromagnetic waves into the underlying material (Plewes and Hubbard, 2001). EM theory describes the propagation of electromagnetic

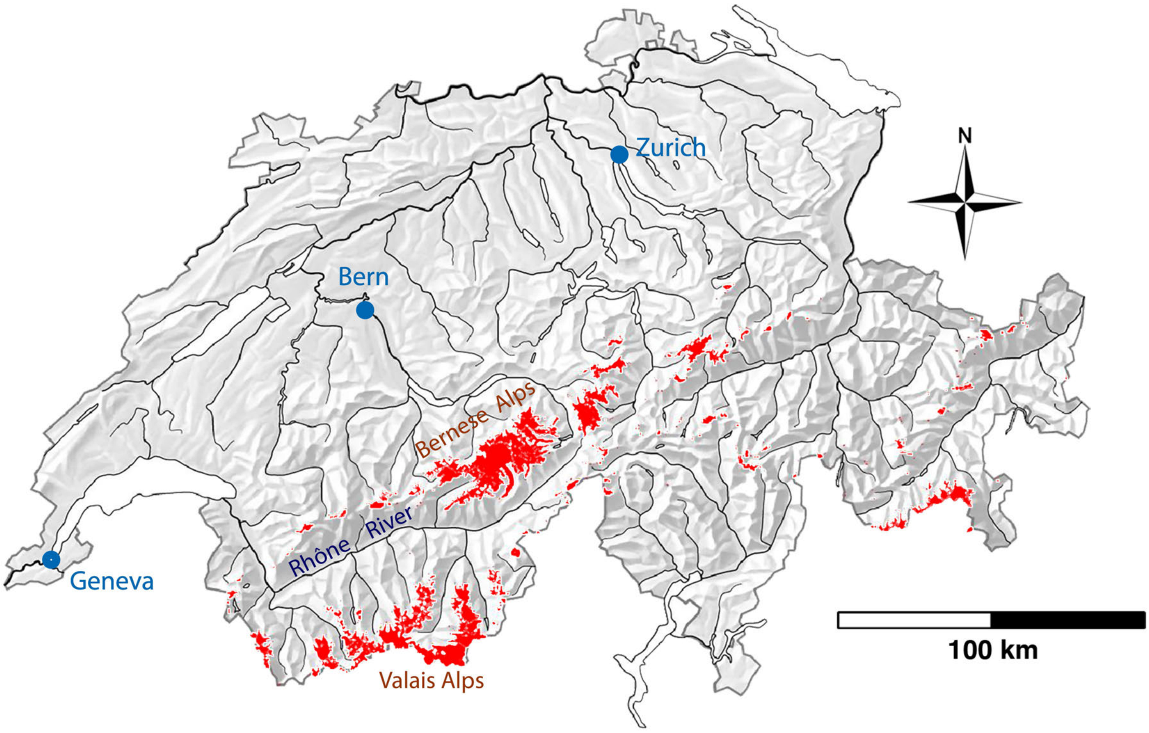

Figure 1.2: Location of glaciated area in Switzerland marked in red. Provided by A. Bauder (Laboratory of Hydraulics, Hydrology and Glaciology, ETH Zürich) and M. Grab (Exploration and Environmental Geophysics, ETH Zürich).

energy in space. Maxwell's equations characterize EM field physics and the properties of the subsurface material are specified by constitutive laws (Annan, 2009). Ice is a low loss material (electrical conductivity $\sigma = 0.01$ mS/m, relative electrical permittivity ε_{r}= 3-4 (Plewes and Hubbard, 2001; Nobes, 2014; Annan, 2005) and therefore a suitable medium to be investigated with GPR. Electromagnetic waves can propagate several hundreds of meters in temperate ice (e.g. Bauder et al., 2003; Kennett et al., 1993) and up to 4000 m in cold ice (e.g. Evans et al., 1972). The change of dielectric properties in materials and scattering of electromagnetic waves in glaciers usually occur due to enclosed boulders, water pockets and channels, the ice-bedrock interface, ice impurities and density variations, anisotropy of the crystal orientation fabric or refrozen crevasse systems (Plewes and Hubbard, 2001). Figure 1.3 displays the geometry of a common offset measurement configuration. Two dipole antennas (transmitter and receiver pair) are carried along the surface of the glacier at a set distance (Δx). The transmitted electromagnetic waves are reflected

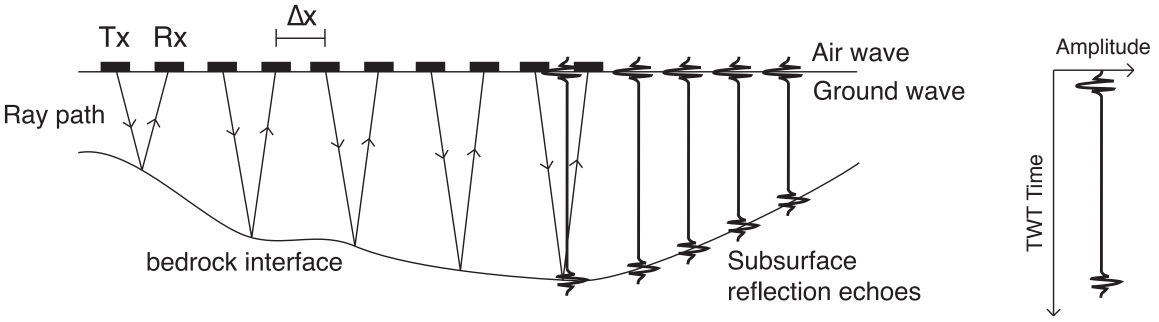

Figure 1.3: Common offset geometry for GPR measurements over glaciers. Transmitter (Tx) and receiver (Rx) pair moved with constant step sizes (Δx - offsets) along the glacier's surface (left). Electromagnetic waves are reflected at ice-bedrock interface. First arrival is the air wave, followed by the ground wave and the subsurface reflection echoes arrive at a later time. Subsequent radar echoes displayed in amplitude and two-way travel time form a radar profile (right). Modified after Nobes (2014) p. 494.

at the ice-bedrock interface and received at the surface by the receiving antenna. A radar profile is produced by displaying subsequent recorded traces in two-way travel time and amplitude values (Nobes, 2014)

1.4 Electromagnetic wave field directionality of dipole-type GPR antennas

While conducting GPR field surveys, the operator has to pay attention to the dipole characteristics of the antennas. Dipole antennas radiate polarized wave fields, which cause high directionality of the amplitudes (Lehmann et al., 2000). Annan (1973), Arcone (1995), and Engheta et al. (1982) were pioneers in the field of describing the vectorial nature of dipole antenna radiation. The analytical far-field solution is based on an infinitesimal dipole approximation (Engheta et al., 1982) and can be used to calculate the 2D radiation pattern for a dipole surrounded by one medium (full space) or placed on an interface (half space) (e.g Lampe et al., 2003; Lehmann et al., 2000). The specific shape of the radiation pattern strongly depends on the electromagnetic properties of the surrounding media. Figure 1.4 depicts the 2D analytical far-field radiation pattern in full space surrounded by air and in a half space at the interface between air (at the top) and ice (at the bottom). The planes perpendicular and parallel to the dipole's axis are defined as H- and

E- planes, respectively. The radiation patterns in Figure 1.4 are shown in H- and E-plane with area-normalized amplitudes and only for the lower hemisphere. In full space, the entire pattern takes the shape of a donut (in Figure 1.4: half donut) with highest amplitudes evenly distributed in the H-plane around the dipole and nulls at its end in the E-plane (also seen in 3D Figure 1.5). Placing the dipole close to an interface changes the energy distribution of the amplitude along the wavefront because of the change in electromagnetic properties of the two media. In the half space model, maximum electrical field amplitudes occur in the H-plane, specifically at the critical angle θ_c. In Figure 1.4, the highest amplitudes in the half space pattern can be recognized between the angles of 140-150° and 210-220° in H-plane and in the E-plane nulls occur at the approximately same angle. Thus, the E-plane pattern is divided into individual lobes.

The far-field criteria only applies when the wavefield has traveled far enough from the source to transition from near- to the far-field. According to Diamanti and Annan (2013), this applies at a distance of 10 wavelengths. Van der Kruk (2001) and Streich (2007) utilized exact radiation pattern in GPR acquisition and processing to enhance 3-D GPR imaging techniques. Other modeling approaches of radiation characteristics and GPR finite-difference time-domain simulation tools were published by Moran et al. (2003) and Lampe et al. (2003). Furthermore, the shape of the radiation pattern varies with the elevation above ground (Van der Kruk, 2004), the horizontal leveling of the dipole (Lampe and Holliger, 2005) and the GPR antenna shielding material (Lampe et al., 2003).

Different field components of the electromagnetic wave can be recorded, if the orientation of the transmitting and/or receiving antenna is changed in space. Several setups, as shown in Figure 1.6, provide additional data about the subsurface in contrast to recording only with the standard broadside, co-polarized setup widely used in geophysical investigations on glaciers. In the broadside configuration, the axes of both, transmitter and receiver antennas, are parallel and with an offset in perpendicular direction. The offset is parallel for the endfire mode. Van der Kruk et al. (2003), Lehmann et al. (2000), Streich et al. (2006), and Streich and Van der Kruk (2007) explain the theoretical background and the usability of multicomponent GPR setups for minimizing the directionality effects on ground-based GPR data in more detail.

1.5 Application of ground-based and helicopter-borne GPR for glacier surveying

Generally, GPR is applied to examine a variety of interior features of glaciers. Higher frequency GPRs (250 MHz - 1.5 GHz) can visualize snow and firn stratigraphy at large spatial scales along transects (e.g. Dunse et al., 2009; Forte et al., 2014; Godio and Rege, 2016) and complement

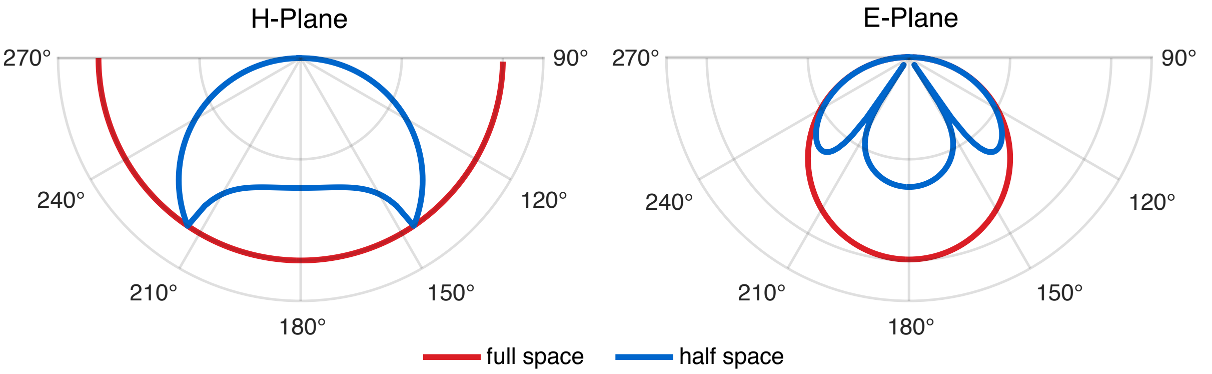

Figure 1.4: Far-field, 2D radiation pattern of a infinitesimal dipole for a full (red) and a half space (blue) in H- and E-plane. Half space is composed of air (top - not shown) and ice (bottom) and the full space entirely of air. The dipole is located directly at the interface and only the radiation pattern of lower hemisphere is shown. Radiation patterns are area-normalized and based on the analytical solution by Arcone (1995) and Engheta et al. (1982).

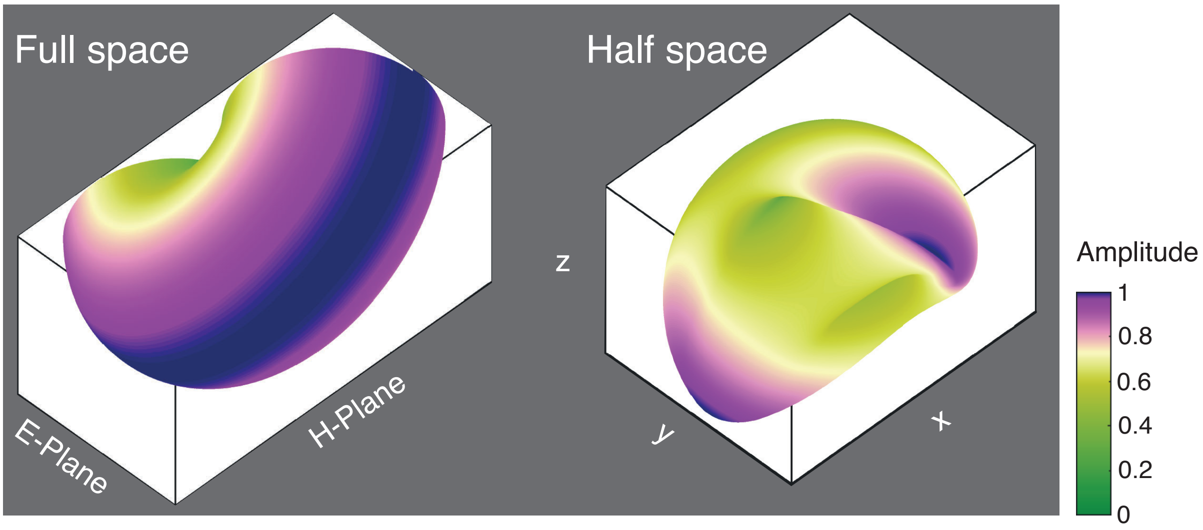

Figure 1.5: 3D far-field representation of the analytical infinitesimal dipole pattern in (left) full space (air) and (right) half space (air-ice). Surface is interpolated with $A = [(S_1 - S_0)\sin^2\phi + S_0]^{\frac{1}{2}}$ from 2D H- and E-planes shown in Figure 1.4. A is the amplitude along the 3D surface, S_0 and S_1 are the powers of the 2D planes and $0<\phi\leqslant 2\pi$. Both radiation patterns are seen from underneath, looking upwards with only the lower hemisphere displayed. Color scale is nonlinear and amplitude values are normalized.

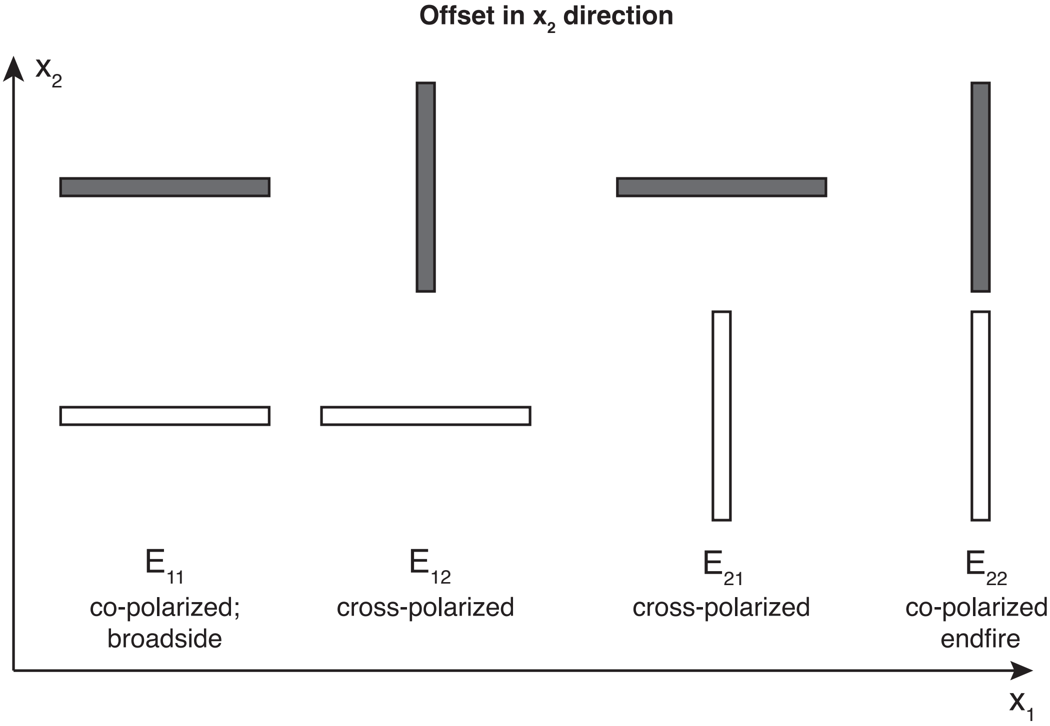

Figure 1.6: Display of common GPR antenna configuration co- and cross polarized. Antennas seen from above in offset mode. The subscript of electric field component $E_{\alpha\beta}$ indicates the recorded field direction x_α and $_\beta$ for the transmitter shown in white and the receiver in gray. Modified after Streich (2007) p. 8.

mass balance estimates based on traditional glaciological methods (e.g. direct mass balance stake measure or snow/firn cores). Additionally, the overall water content is of interest for geophysical-glaciological investigations (e.g. Garambois et al., 2015) as well as ice crystal orientation (e.g. Drews et al., 2009; Matsuoka et al., 2012a), hydrological englacial and subglacial systems (e.g. Gabbud et al., 2015) and the structure and topography of the ice-bedrock interface (e.g. Bauder et al., 2003; Feiger et al., 2018; Langhammer et al., 2017). Figure 1.7 displays a typical ground-based GPR profile, which was recorded with a 25-MHz antenna system on the Gries Glacier, Switzerland by Feiger et al. (2018). The bedrock reflection is clearly visible, specifically below 100 m depth, and englacial scattering occurs in the shallower regions above 60 m depth. Other examples of ground-based radar transects on a Swiss glacier can be found in Chapter 2 and 3 of this thesis.

Traditionally, GPR systems are carried along the glaciers surface either manually or pulled behind vehicles. Mapping the bedrock topography with low frequency (e.g. 15-50 MHz on Alpine glaciers) dipole GPR antennas can become challenging because of their physical size of 2 m and

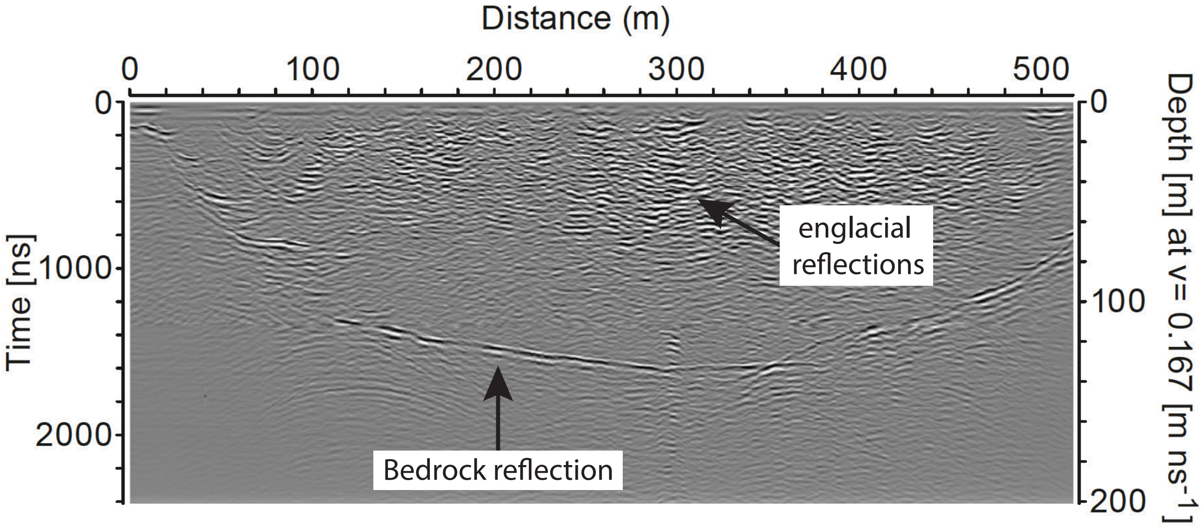

Figure 1.7: Example of a ground-based GPR profile with 25 MHz antennas on the temperate alpine Gries Glacier. Data published in Feiger et al. (2018) and figure is modified.

longer. If the glacier is located at high alpine elevations or the slope of the glacier surface becomes steeper, a thick snow cover is present or extensive crevasse fields occur, airborne GPR techniques are superior. In this case, airborne systems are more cost-effective in operation and require less manpower.

In recent years, helicopter-borne GPR systems have gained attention as a profitable method to conduct large scale surveys in the European Alps. Rutishauser et al. (2016) provide a comprehensive overview about three different helicopter-borne GPR systems, which were used between 2008-2013 to collect approximately 1200 km of radar transects for mapping the subglacial bedrock topography. The frequency of the employed antenna setups include a 30 MHz (BGR-P30) and a 70MHz pulsed GPR system (Blindow et al., 2011; Geophysical Survey Systems Inc., 2017) and a 55 to 150 MHz (HERA-G) stepped-frequency system (Eisenburger et al., 2008; Krellmann and Triltzsch, 2012). The success rate varied between 11.7-69.9 % for the individual systems per total recorded profile length and a differences in the data quality depending on the field site were observed. Another helicopter-borne GPR system in the European Alps was presented by Urbini et al. (2017) with 40 MHz antennas attached to a wooden bird. For a broader overview about the evolution and application of helicopter-borne GPR systems on glaciers around the globe, the reader is referred to Chapter 3 of this work.

1.6 Thesis objectives and outline

Despite efforts in the past to delineate the bedrock topography of individual glaciers (Bauder et al., 2003; Eisen et al., 2009; Maurer and Bauder, 2013; Rutishauser, 2013), a data base of large scale bedrock surveys was missing for the Swiss Alps. The lack of available national data gave rise to an interdisciplinary project initiated by the Exploration and Environmental Geophysics (EEG) group and the Laboratory of Hydraulics, Hydrology and Glaciology (VAW) at ETH Zürich, as well as the Swiss Geophysical Commission (SGPK). The project aims to establish a comprehensive data base of subglacial bedrock topography in the Swiss Alps to advance the fundamental understanding of glacier behavior in a changing climate. It is embedded in the framework of the Swiss Competence Center for Energy Research - Supply of Electricity (SCCER-SoE). The project is unique in financial and logistical efforts, geospatially and computationally extensive and based on new developments in GPR surveying techniques. Scientific staff involved in the project are based at EEG (Prof. Hansruedi Maurer, Prof. Johan Robertsson, Dr. Lasse Rabenstein, Dr. Lino Schmid, Dr. Melchior Grab and Lisbeth Langhammer as a PhD student) and VAW (Dr. Andreas Bauder). Additionally, we are cooperating with the engineering and surveying company GEOSAT SA in Sion, Switzerland as well as BRTechnik for planning and constructing the airborne GPR equipment.

To fulfill the overall goal of determining the amount of glacier mass in the Swiss Alps, helicopter-borne instead of ground-based GPR surveys are compulsory to achieve area-wide data coverage in the limited time of the project. This PhD thesis reflects the efforts to establish a novel GPR methodology, the development and application of a new, exceptional helicopter-borne GPR system with optimized survey strategies and the implementation of a glacier mass estimation technique based on the collected GPR data.

The main specific objectives of the project are

- GPR methodology: In depth characterization of GPR radiation patterns of dipole antennas in glacier ice for optimal airborne GPR acquisition
- Data acquisition: Development and testing of a suitable helicopter-borne GPR acquisition system for standardized, time-effective surveying of the majority of the Swiss glaciers
- Data processing: Establish and implement an extensive processing software to exploit the helicopter-borne GPR data in depth and to homogenize the output of the system consisting of several individual technical components
- Joint interpretation: 3D glacier mass distribution based on acquired GPR profiles and glacier thickness models

- Survey design: Optimize helicopter flight paths over the survey area to reduce costs and maximize aerial coverage for individual surveys

This work focuses on the methodological background for an effective antenna setup design in terms of antenna orientation during acquisition and the enhanced processing for multicomponent (two antenna directions for a co-polarized, broadside mode) GPR data. Furthermore, special attention is given to the interpretation of glacier mass distribution related to the GPR-derived basal topography. Several field surveys were carried out on different Swiss glaciers to conduct pilot studies of GPR antenna orientation effects and to continually test the developed helicopter-borne system.

The following chapters present my work as part of the aforementioned interdisciplinary project, the results published in international journals and give an outlook on future potential research topics emerging from the accomplished goals.

Chapter 2 demonstrates the effect of the dipole antenna orientation on GPR data quality for the purpose of detecting the subglacial bedrock topography. Different ground-based GPR systems and frequencies were tested on the Otemma Glacier, Switzerland to identify the best surveying strategy with dipole antennas on Alpine glaciers. To explain the differences in bedrock reflection visibility, a numerical study is further used to test the influence of the specific dipole radiation pattern on glacial GPR data.

In Chapter 3, our novel helicopter-borne GPR system (AIR-ETH) is presented with its dual-polarization antenna configuration. Additionally, the advantage of applying a pseudo-scalar approach for multicomponent GPR processing is presented with helicopter-borne examples from the Plaine Morte and Oberaletsch Glacier in Switzerland. The changes in radiation pattern with increasing flight height above the glacier surface are numerically derived and summed to approximate a full radiation pattern consisting of two polarizations.

Chapter 4 describes the implementation of the GlaTE (Glacier Thickness Estimation) inversion, which is used to generate a three-dimensional ice thickness distribution of our test glaciers. The inversion is constrained by the thickness measured with the previously recorded GPR data, the thickness gradient calculated with a glaciological mass conservation model and other additional constraints. By combining the GlaTE inversion and sequential optimized experimental design methods, improved survey layouts for GPR measurements on Alpine Glacier are generated and compared for different glacier types.

In Chapter 5 the outcome of this work is reviewed and in Chapter 6 further potential applications and open research questions are discussed.

Chapter 2

Ground-penetrating radar antenna orientation effects on temperate mountain glaciers

Abstract

Ground-penetrating radar (GPR) surveys on glaciers are generally restricted to a single pair of bistatic dipole antennas orientated either parallel or perpendicular to the surveying direction. Extensive helicopter-borne and ground-based GPR investigations on the Glacier d'Otemma, Switzerland, demonstrated that the detectability of the ice-bedrock interface varies substantially with dipole orientation. We recorded several across and along profiles using two different commercial GPR systems and operated with 15-, 25-, 50- and 70-MHz antennas. Dipole alignments parallel to the glacier flow generated considerable stronger and more coherent bedrock reflections compared to a perpendicular dipole setup. We observed the behavior for all employed systems and antenna frequencies. To help explain these findings, we performed 3D numerical modeling using the open source software gprMax. Simulations with 20-MHz transmitting and receiving dipoles indicated that the changes of the bedrock reflection amplitude are primarily governed by the bedrock topography. Scattering and intrinsic attenuation may also influence the amplitudes of the bedrock reflections, but these effects seem to be much less pronounced. Evidently, to increase the GPR bedrock reflection quality, dipole antennas should be orientated parallel to the glacier flow direction on glacier confined to a valley. Since the directional dependence is a first-order effect, it is advisable to perform multi-component surveys, when the general shape of the bedrock topography is unknown. The multi-component setup preferably consists of two sets of dipole antennas, each in broadside configuration and the sets orthogonal to each other.

Published in: Langhammer, L., Rabenstein, L., Bauder, A. and H. Maurer (2017). Ground-penetrating radar antenna orientation effects on temperate mountain glaciers. GEOPHYSICS, Vol. 82, No. 3, P. H15–H24.

2.1 Introduction

Glaciers in the European Alps have experienced severe retreat in recent decades due to increasing annual air temperatures (Haeberli and Beniston, 1998; Rebetez and Reinhard, 2007). Switzerland's energy production is significantly based on hydro-power, which is driven by rain events and meltwater inflow of snow and glacier ice. Thus, the decrease of existing glacier ice in the Swiss Alps is a major concern for communities and industry to sustain renewable energy production and fresh water storage in the future. Temporal changes in glacier ice mass can be monitored using direct glaciological and remote sensing methods (e.g. Bauder et al., 2003; Farinotti et al., 2009a). For example, mass-balance stakes and satellite altimetry data allow tracking of temporal surface variations. In contrast, estimates of the absolute ice volume require detailed knowledge of the underlying bedrock topography. Seismic surveying and ground-penetrating radar (GPR) have proven to be valuable probing tools for the glaciological community to measure the thickness of ice bodies (e.g. Plewes and Hubbard, 2001; Polom et al., 2014). Logistically inexpensive, compared to other near-surface geophysical methods, and a wide range of applications, GPR is considered to be the most suitable option (Nobes, 2014; Woodward and Burke, 2007). It provides an even greater advantage in rough terrain environments, since GPR systems can be operated airborne as well (Blindow et al., 2012; Bradford et al., 2010; Merz et al., 2015; Rutishauser et al., 2016).

In the beginning of the 1980s, Watts and Wright (1981) mounted a 1.2-MHz radar system on a fixed-wing aircraft to measure the ice thickness of the Columbia Glacier, Alaska. Advances in technology and system stability enabled Kennett et al. (1993) to attach a 5-MHz GPR system underneath a helicopter for depth sounding surveys on Engabreen, Norway. In the following years, numerous ground-based and airborne GPR applications in Polar regions and other areas, where cold ice prevails, showed remarkably good results; but on temperate ice bodies it appears to be much more challenging to image the bedrock topography at greater depths. Recent developments by Blindow et al. (2012) demonstrated the capability of airborne GPR systems to penetrate down to 800 m within temperate ice of the North Patagonian Ice Field with a 30-MHz radar system. However, Rutishauser et al. (2016) found that attempts with similar systems were far less successful over Alpine glaciers in Switzerland. At some locations, bedrock down to 600 m depth was imaged, but along the majority of the collected profiles the penetration depth was much shallower. Overall, the ice-bedrock interface was only visible in less than 50 % of the entire length of the profiles.

The large variability of data quality can either be attributed to glacier ice properties or features of the GPR system setup. Ice properties govern the attenuation of the electromagnetic waves, and can vary throughout the glacier mass due to the existence of i) micro- and mesoscale water intrusions (Bradford et al., 2009; Murray et al., 2000), ii) macroscale supra- and englacial features, such as crevasses and meltwater channels (Bradford et al., 2013; Nobes, 1999), iii) internal electrical anisotropy induced by ice crystal orientations and/or air bubbles (Drews et al., 2012; Matsuoka et al., 2012b).

For detecting and delineating a desired target in the subsurface, the appropriate antenna frequency and sufficient transmitter power are essential, but the relative positioning and orientation of the transmit and receive antenna dipoles are critical parameters as well. Commonly antenna orientations are constrained by the operational handling in the field and often there is little flexibility during experimental design. Yet, it was observed that the orientation of the dipoles relative to the strike of dipping reflectors can affect the image quality (Nobes and Annan, 2000). Nobes (1999) performed GPR measurements on a temperate glacier in New Zealand. He observed that the bedrock reflection becomes obscure, when the antennas are orientated perpendicular to the glacier flow. Nobes (1999) speculated that the decrease in amplitude strength is caused by the presence of crevasses and micro-scale features in the ice body. An alternative explanation for these observations is the shape of the bedrock topography. Moran et al. (2003) used a Helmholtz-Kirchhoff diffraction integration method to numerically reconstruct the GPR responses over a complex glacier bed. They showed that the bedrock visibility is dependent on the antenna orientation, but their numerical results were only partly supported by their own field data (measured with a single antenna orientation) and the data of Nobes (1999).

Considering the potentially strong influence of the antenna orientation on the imaging quality of the bedrock topography underneath temperate glaciers, and the partly inconclusive results from previous studies, we deemed it worthwhile to investigate this problem in more detail. For that purpose, we have collected a comprehensive GPR data set using several antenna frequencies and orientations on a temperate glacier located in the Western Swiss Alps. In the first part of the paper, we introduce the test site and describe our data acquisition and processing approach. Then, we present numerical modeling results to explain our field observations. In particular, we investigate to what extent the observed dependency of the bedrock reflection amplitude on the antenna orientation can be solely attributed to the shape of the bedrock topography.

2.2 Field site

The Glacier d'Otemma (2465-3815 m a.s.l) is located in the south-western part of the Valais region, Switzerland (see Figure 2.1). It originates at the Col de Charmotane at the southern flank of the Pigne d'Arolla mountain and flows towards the south-west. The equilibrium line altitude is located around 2900 m a.s.l. (Gabbi et al., 2012). Several smaller tributary glaciers in the north and east feed the glacier tongue. In 1973, the ice covered area was estimated 17.51 km^2 with a length of 8.7 km (Müller et al., 1976). Since then, the glacier tongue has retreated ∼1.3 km, with length changes up to 107.0 m (2002-2003) per year (Bauder, 2016). Today, the average glacier thickness is ∼250 m, and the ice is assumed to be temperate.

During the last five years, the Glacier d'Otemma has served as a test site for multiple helicopter-borne and ground-based GPR campaigns (e.g. Rutishauser et al., 2016), because of its representative mountain glacier shape, typical shallow bedrock structure, and slope. In this study, we consider various data sets of along and across profiles as indicated in Figure 2.1. All data were recorded with parallel dipoles.

To clarify terminology, we are referring to x- and y-directed dipole GPR antenna configurations for the survey setup. The x-orientation refers to an alignment of the antennas approximately in the direction of glacier flow, parallel to the surrounding valley walls in the lower area of the glacier's tongue. The y-directed dipoles are orientated perpendicular to the glacier flow (Figure 2.1). Hence, the terminology is independent of the flight path or surveying direction.

2.3 Data acquisition

2.3.1 Helicopter-borne data

In March 2014, we acquired helicopter-borne data with a 70-MHz SUBECHO-40 antenna pair connected to a GSSI SIR-3000 (Geophysical Survey Systems Inc., 2016). The antennas were mounted parallel to the skids of a helicopter. One along (∼3250 m) and across profile (∼1200 m) were measured over the Glacier d'Otemma (Figure 2.1). The proximity of the antennas to the helicopter simplified the operational handling and reduced the risks of crashing during the flight, but the close vicinity to the fuselage can cause dominant ringing effects in the recorded data (Rutishauser et al., 2016). To ensure an adequate spatial sampling, the helicopter flew with a speed of < 20 km/h and 10-20 m above the glacier's surface. Because of the fixed position of the antennas, the along profile was measured with x-directed dipoles and the across profile was recorded with y-directed dipoles (Figure 2.1). For accurate positioning in the order of centimeters, a differential GPS system was attached to the helicopter's roof.

2.3.2 Ground-based data

For the ground-based surveys, three different GPR setups were considered. All profiles were recorded during one campaign in October 2014. We operated the pulseEKKO PRO system with 25- and 50-MHz antennas (Sensors & Software, 2016), and the GSSI SIR-3000 with 15-MHz 3200 MLF antennas. Each profile was measured twice with the same system, using x- or y-directed parallel dipoles in broadside configuration, respectively. We carried the system manually over the glacier's surface, either by hand or mounted on a rigid wooden frame. The along profiles extended over a length of ∼1200 m and the across profiles stretched over ∼680 m before crevasses

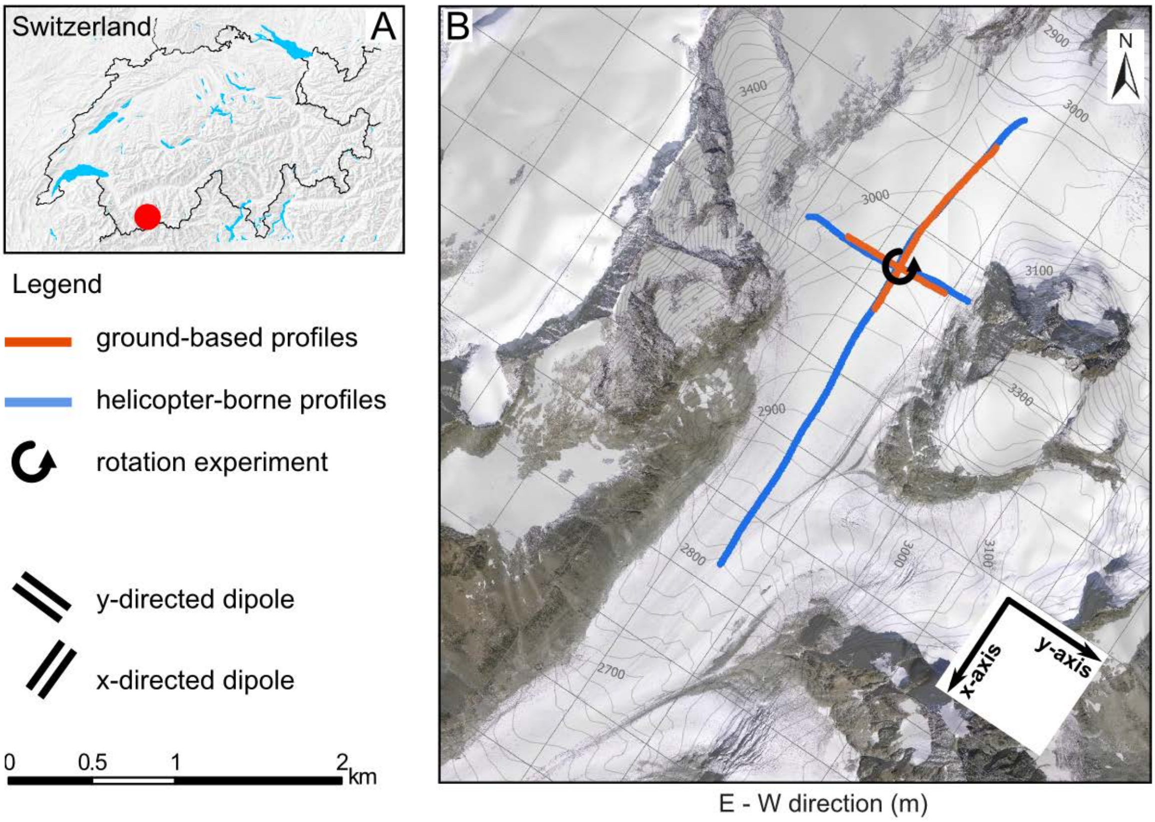

Figure 2.1: A) Location of the Glacier d'Otemma, Switzerland (red dot). B) Orthophoto © 2017 swisstopo (JD100042) with a superimposed mesh grid of 500x500 m. X-axis is parallel to glacier flow direction and Y-axis is perpendicular to the glacier flow. Red and blue lines indicate the GPS locations of the ground-based and helicopter-borne profiles.

prohibited further passage. A differential GPS (Leica Geosystems, 2016) was attached to the GPR console and carried in the same backpack by the operator. In addition to acquiring the profiles, we conducted rotation experiments at the deepest point of the glacier with each of the GPR antennas (Figure 2.1) to investigate the bedrock visibility depending on the dipole orientation. Both dipoles were initially placed in y-directed position and were then rotated around a midpoint. A trace was recorded at every 5° until the 180° position was reached. Accordingly, a 90° rotation corresponds to an x-directed alignment of the antennas. Acquisition parameters of all data sets are summarized in Table 2.1.

Table 2.1: Data acquisition and GPR systems (Geophysical Survey Systems Inc., 2016; Sensors & Software, 2016), PE = pulseEKKO.

System and antennas	Ground PE PRO	Ground PE PRO	Ground GSSI 3200 MLF	Helicopter GSSI SUBECHO-40
Nominal antenna frequency (MHz)	25	50	15	70
Dipole separation (m)	4	2	5.5	2
Sampling rate (ns)	3.2	1.6	4.39	1.85
Trace length (ns)	4560	4520	4500	3800
Antenna transportation	Rigid frame	Manually	Manually	Helicopter
Positioning	Diff. GPS	Diff. GPS	Diff. GPS	Diff. GPS

2.4 Data processing

The profile data were processed following a standard scheme for GPR data analysis with minor modifications for ground-based and helicopter-borne data (Table 2.2). Each step was performed using in-house processing routines written in MATLAB and the CREWES MATLAB software (Margrave, 2003). First, differential GPS coordinates were assigned to the individual traces and the data format of the commercial GPR systems were converted to a suitable industry standard format (SEG-Y). We applied median filter background removal to the GSSI data (Geophysical Survey Systems Inc., 2016) and a custom software running average filter was used for the pulseEKKO PRO data (Sensors & Software, 2016). Both, the helicopter-borne and ground-based data were statically corrected for time-zero. For the helicopter-borne profiles we additionally picked the ground surface reflection (Table 2.2). Since no altimeter was available, we used the surface reflection time to determine the height of the antennas above the ground. Next, we applied a singular value decomposition filter with the largest 2 % of the eigenvalues set to zero to remove the ringing noise (Kim et al., 2007). The spatial filter window size had the length of the entire profile, because the coherent ringing noise of the helicopter appeared to be persistent throughout the individual survey lines. Furthermore, a bandpass filter was applied, with corner frequencies depending on the central frequency of the operated GPR system (Table 2.2).

The varying speed of the helicopter during the flight and changes in walking speed for the ground measurements, whilst carrying the GPR antennas over the rough surface terrain, caused irregular spatial sampling of traces. To equalize the trace spacing, we projected the binning centers, separated by 0.5 and 1 m, on a straight line for the ground-based profiles and the helicopter-borne data, respectively. The average original trace spacing was a few centimeters for the ground-based data and between 0.5 and 1.0 m for the helicopter-borne data. Based on the GPS position, the individual GPR traces were assigned to the binning centers with the weighted nearest neighbor interpolation. Further processing included Kirchhoff-time migration (Table 2.2). Prior to the migration we generated a half-space velocity model with a uniform ice layer and overlying air layer, which served as an input for the migration algorithm. The interface between the air and ice layer corresponds to the true surface topography. A radar velocity of 0.167 m/ns for ice was employed, which is typical for temperate glaciers (Reynolds, 2011). The migration was carried out with the corresponding module of the CREWES MATLAB processing package (Margrave, 2003) using the default control parameters.

The same velocity was considered for the time-to-depth conversion of the plotted profiles. All profiles were arranged such that the vertical axis represents depth below the surface and not elevation. Spherical divergence, scattering and intrinsic attenuation of the radiated electromagnetic waves cause the signal strength to decrease with depth. Similar losses are encountered on the return path for reflected signals. We accounted for these losses by applying a time-variant gain function of the form e^{at} (t = time, a = scaling factor) to boost the data and appropriately adjusting the color scale to enhance features from deeper structures. Identical parameters for the gain functions and color scales were used for comparing profiles acquired with x- and y-directed dipole configurations.

2.5 Experimental Test Data Results

The processed sections acquired with the helicopter-borne system are shown in Figure 2.2. The fixed setup of the antennas alongside the helicopter skids resulted in an x-directed dipole configuration for the along profile and y-directed dipoles for the across profile. We observed a moderate to good bedrock visibility (i.e. prominent reflection and SNR $\sim$ 2-5), when the antennas were orientated parallel to the glacier flow (x-directed dipoles, Figure 2.2a). The along profile shows reflections of bedrock undulations beneath the glacier and an increasing slope towards the saddle area in the north-east. It should be noted that such along profiles suffer from out-of-plane effects. The bedrock reflections don't necessarily originate from the bedrock directly underneath the profile line. They can arise from reflection points on interfaces out of the plane of the profile. This is commonly referred to as sideswipe and indicates the true 3D nature of the target and explains the appearance of multiple reflection segments as indicated with red arrows in Figure 2.2a. GPR profiles are generally acquired perpendicular to geological subsurface structures. In this study, we are primarily interested in antenna orientation effects. Therefore, we refrain from localizing the sideswipe reflections accurately. For our purpose, it is only important to assume that all reflections

Table 2.2: Data processing parameters, Abbreviation for data set: helicopter-borne (H), ground-based (G) and modeled (M)

Processing step	Data set	Details
Assigning coordinates to traces	(H) (G) (M)	Coordinates from differential GPS
Dewow	(H) (G-GSSI) (M)	Median background removal
	(G-PE)	PulseEKKO Software; running average filter
Time-zero correction	(G) (M)	Manual picking of air wave
Surface elevation picking	(H)	Manual picking of surface reflection
Singular value decomposition filter	(H) (G)	largest 2% eigenvalues set to 0
Bandpass filter	(H)	34-100 (70 MHz)
	(G)	15-40 MHz (15-MHz), 10-40 MHz (25-MHz), 25-75 MHz (50-MHz)
Binning	(H)	1 m
	(G) (M)	0.5 m
Time-variant gain function	(H) (G) (M)	e^{at} (t = time, a = scaling factor)
Two-layer Kirchhoff time migration	(H) (G) (M)	Constant velocity air: 0.299 m/ns temperate ice: 0.167 m/ns
Time-depth conversion	(H) (G) (M)	Same velocity as migration

visible in the profiles, originate from the deeper part of the glacier and are thus subject to similar antenna orientation effects.

The bedrock reflections in the across profile Figure 2.2b vanish abruptly at a depth of ∼40 m and no indications of bedrock reflections at greater depths are visible. Furthermore, a pronounced near-surface scattering zone appears in the central part of the profile. The system settings were identical for both profiles shown in Figure 2.2 (Table 2.1). Therefore, the fact that no deeper bedrock reflection in the across profile is visible, must be attributed to the orientation of the antenna dipoles. Very similar results were obtained with the pulseEKKO PRO system and 50-MHz antennas mounted underneath the helicopter (not shown), thereby indicating that the observations are not unique to the GSSI system. These findings motivated us to perform a more detailed study on antenna orientation effects on the ground, including the comparison of different GPR systems.

Ground-based results using the 50-MHz pulseEKKO antennas are shown in Figure 2.3. As expected, the overall quality is superior compared to the helicopter-borne data in Figure 2.2 (see

Rutishauser et al. (2016) for a more detailed discussion of ground-based vs. helicopter-borne data). A comparison of the x- and y-directed dipole data of the across and along profiles (Figure 2.3a and 2.3b) confirms the influence of the antenna orientation on the image quality of the ice-bedrock interface.

Similar to the helicopter-borne data in Figure 2.2b the ground-based y-directed across profile (Figure 2.3b) shows areas of high scattering underneath the surface and no coherent bedrock reflections. In contrast, the x-directed across profile in Figure 2.3a shows a pronounced bedrock reflection. As already observed in Figure 2.3a, the x-directed dipole data in Figure 2.3c also show clear bedrock reflections, although they are distorted by out-of-plane effects, and the y-directed dipole data in Figure 2.3d exhibit only a faint signature of the bedrock interface. Generally, our initial observations from the helicopter-borne data are confirmed by the 50-MHz ground-based measurements.

In glaciological surveys, GPR antennas with dominant frequencies below 50-MHz are often employed for measuring the glacier thickness. Therefore, we tested if our findings shown in Figures 2.2 and 2.3 can be reproduced with lower frequency antennas. The results using the pulseEKKO PRO 25-MHz and GSSI 15-MHz antennas (see Table 2.1) are shown in Figures 2.4 and 2.5, respectively. As expected, the lower frequencies allow a better depth penetration, and the ice-bedrock interface appears more coherent compared to the 50-MHz data. It is noteworthy that the low frequency profiles also exhibit bedrock reflections in the unfavorably oriented y-directed dipole data (Figures 2.4b, 2.4d, 2.5b and 2.5d), but the corresponding x-directed dipole data offer a much better data quality. Similar to the 50-MHz data (Figure 2.3b), the low frequency y-directed dipole data show an increased amount of scattering in the uppermost 100 m (e.g. Figure 2.5b and d). Overall, the antenna orientation effect appears to be independent of the antenna central frequency.

The across profiles indicate a maximum ice thickness of ∼250 m at the profile intersection, and the along profiles also show their deepest reflector at a similar depth. We have further examined the reflection signature at the the profile intersection by conducting a rotation experiment. The experimental setup is shown in Figure 2.6a, and the unmigrated results using 50-MHz antennas are displayed in Figure 2.6b. In addition, Figure 2.6c shows the enlarged bedrock reflection at 250 m depth in the form of normalized absolute amplitude values. It is noteworthy that the amplitude pattern in Figure 2.6c is not symmetric around 90°, and the reflections are slightly shifted upwards between 90° and 180° by ∼0.5 m. The reflected signal in Figure 2.6 presumably originates from a slightly different bedrock locations due to irregular bedrock topography with the shift being much smaller than 1% of glaciers depth.

The amplitude of the bedrock reflection is not constant throughout the rotation cycle. The highest amplitudes were recorded, when the antenna setup was similar or equivalent to an x-directed dipole configuration (90°). Rotating the antennas towards a y-directed dipole alignment

(0° or 180°) causes the amplitude to decrease considerably (>80%). Similar results were observed in the rotation profiles of the pulseEKKO PRO 25-MHz and GSSI 15-MHz systems (not shown).

Our data provide clear evidence that the antenna orientation during data acquisition on a temperate glacier has a substantial impact on the bedrock visibility. In contrast to earlier investigations by Moran et al. (2003) and Nobes (1999), our measurements were solely designed to investigate the influence of the antenna orientation. The findings are supported by a comprehensive data base including x- and y-directed dipole profiles, ground-based and helicopter-borne antenna setups and a large range of center frequencies. Additionally, we present an extensive amount of data collected in the accumulation zone of the glacier.

2.6 Numerical modeling

Our field data sets provide compelling evidence that the antenna orientation has a substantial effect on the data quality. This has been observed previously (Moran et al., 2003; Nobes, 1999), but the controlling factors of these observations are still unclear. A likely hypothesis is that the combined effect of antenna radiation patterns and bedrock topography predominantly governs the amplitude strength. We have tested this conjecture by making use of numerical modeling.

For that purpose, we employed the open source software gprMax 3D Version 2.0 (Giannopoulos, 2005), a Finite-Difference Time-Domain (FDTD) solver for electromagnetic wave propagation. Based on the GPS derived surface elevation and GPR derived bedrock topography along the x-directed across profile (Figures 2.4a), we constructed a 2D model and extended it uniformly into the third dimension. A sketch of the model is shown in Figure 2.7, and the associated model parameterization is summarized in Tables 2.3 and 2.4. To reproduce the ground-based profiles measured in the field, 1313 antenna positions were modeled, each with x- and y-directed dipoles (Figure 2.8b and c). The transmitting (Tx) and receiving (Rx) dipole were placed 20 cells away from the model boundaries and 1 m above the air-ice interface following the surface topography. Modeling of a single source position required 6 hours on a 48 core cluster, resulting in 378144 CPU hours per profile. The model consists of an air layer, homogeneous temperate glacier ice and granite bedrock (Table 2.4). Due to the enormous computation time of the numerical simulations, the cell size was chosen to be far greater than what would have been necessary for resolving ice anisotropy or water inclusion effects. Therefore, internal electrical anomalies aren't included in the homogeneous ice body. The modeled GPR data were processed in a similar matter to the ground-based field data, including background removal, zero-time correction, Kirchhoff-time migration and application of a time-variant gain to boost later arrivals (Table 2.2).

Figure 2.8b and c show the modeled 20-MHz across profiles. The high reflection amplitudes in the x-directed dipole profile and lower reflection amplitudes in the y-directed dipole transect are

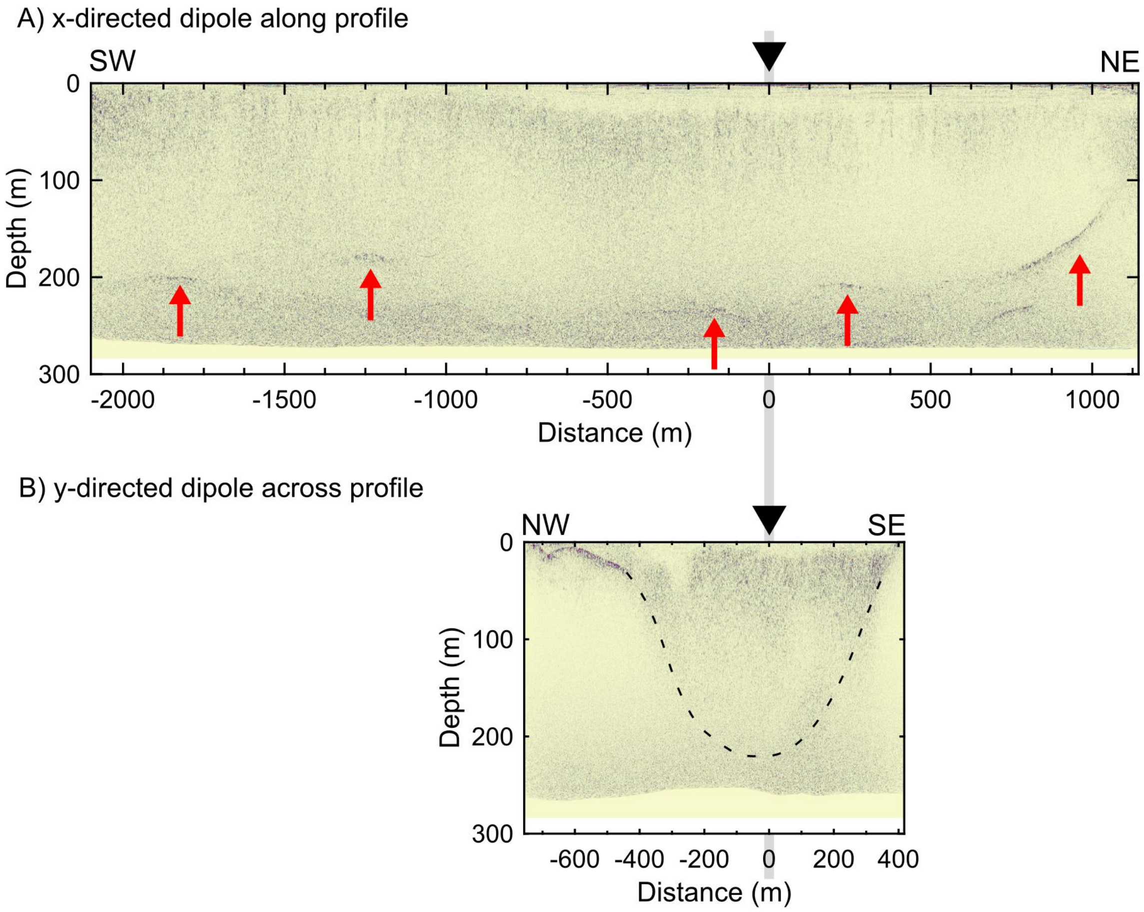

Figure 2.2: Helicopter-borne GSSI 70-MHz along (x-directed dipoles) (A) and across (y-directed dipoles) (B) profiles over the Glacier d'Otemma. Exaggeration of depth axis is 3:1. Red arrows show bedrock reflection at greater depths (A) and the approximate position of the ice-bedrock interface is indicated with a dashed black line in the across profile (A). Black triangles correspond to the cross over location of both profiles.

broadly consistent with the observed data (Figures 2.4 and 2.5). By comparing the north-western and south-eastern flanks of the bedrock reflection, the difference in received energy becomes apparent. Higher amplitudes can be seen in both (x- and y-directed dipole) profiles at the deepest part of the glacier, presumably caused by signal focusing at small bedrock undulations.

Reproducing the entire rotation experiment (Figure 2.6) was impractical, because gprMax does not allow for incremental rotation of the antennas. Consequently, the geometry model underneath has to be rotated. This requires a full-size glacier model (length and width: 701.5 m), which was beyond our computational capabilities. Yet, we were able to simulate the bedrock reflection

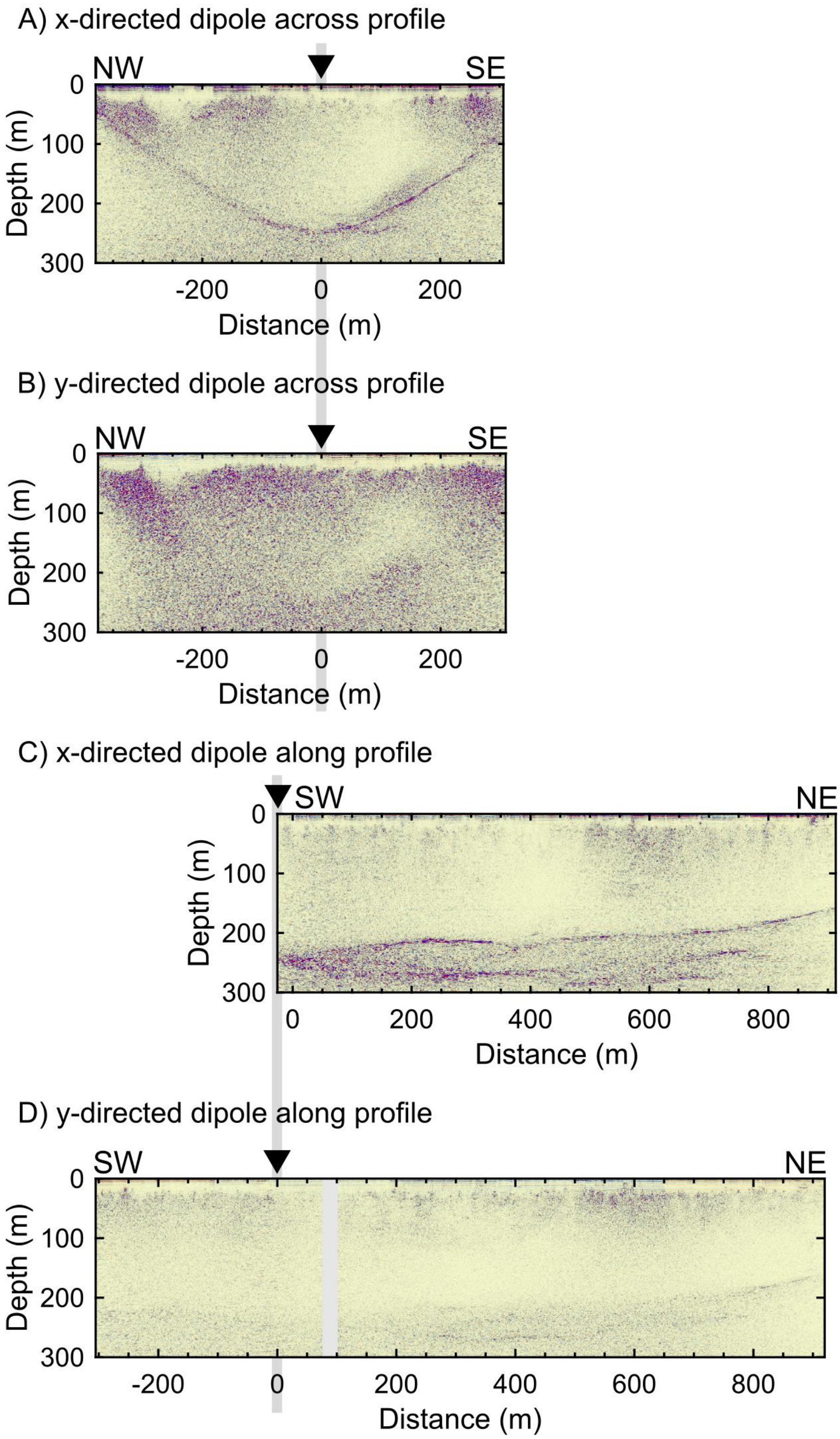

Figure 2.3: Ground-based pulseEKKO PRO 50-MHz across (A, B) and along (C, D) profiles with x- and y-directed dipoles.

A) x-directed dipole across profile

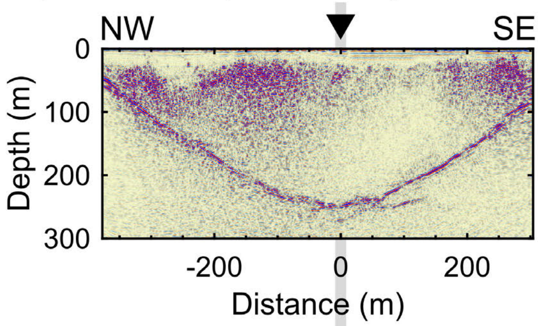

B) y-directed dipole across profile

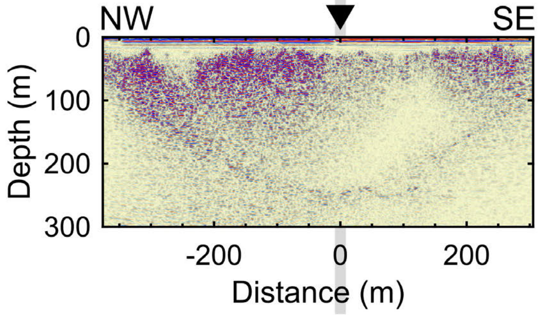

C) x-directed dipole along profile

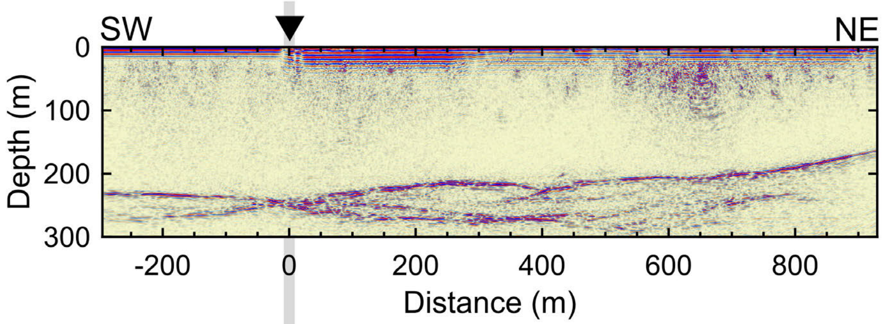

D) y-directed dipole along profile

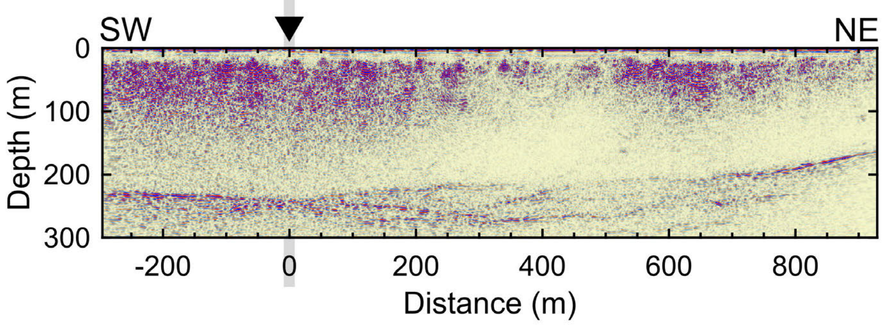

Figure 2.4: Ground-based pulseEKKO PRO 25-MHz across (A, B) and along (C, D) profiles with x- and y-directed dipoles.

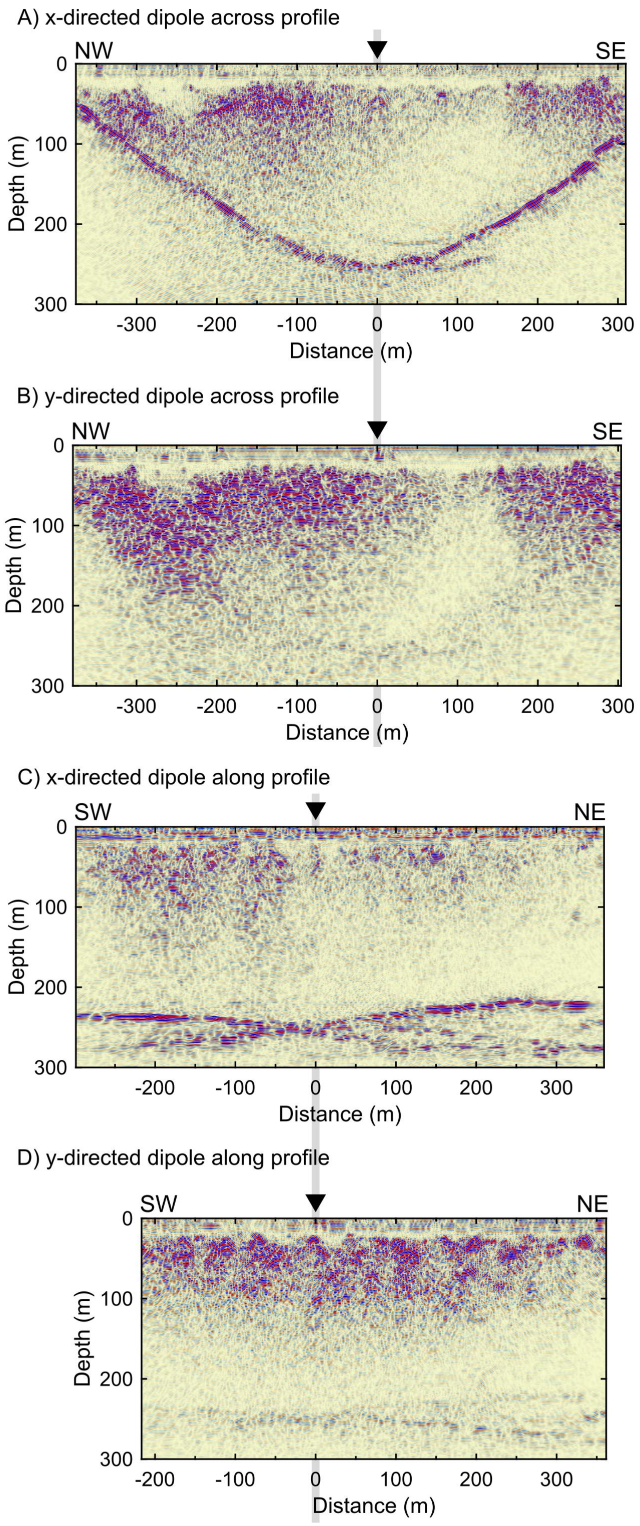

Figure 2.5: Ground-based GSSI 3200 MLF 15-MHz across (A, B) and along (C, D) profiles with x- and y-directed dipoles.

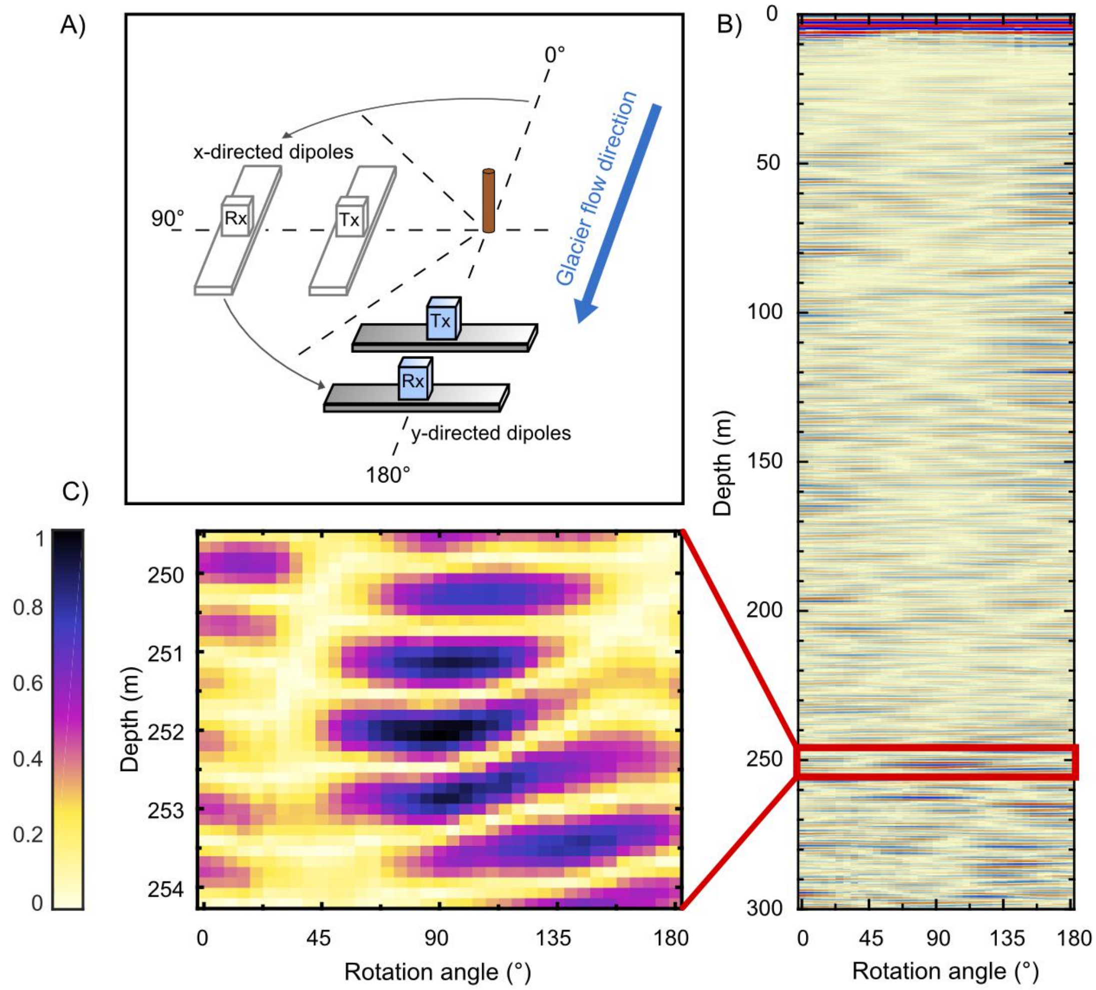

Figure 2.6: Ground-based PulseEKKO Pro 50-MHz rotation experiment. A) Schematic of rotation experiment at the cross-over point. Antennas were rotated for 180° in 5° steps, starting with y-directed dipoles at 0° position. B) Rotation profile with bedrock reflection at ∼250 m depth with enlarged section (C) showing the absolute, normalized amplitude of traces.

response for 90° (x-directed) and 180° (y-directed) antenna setups. Figure 2.9 presents the amplitude of the bedrock reflection for both antenna orientations. As seen in the previous results, the amplitude of the x-directed dipole trace (red) is significantly higher for the bedrock reflection at ∼2700-2900 ns. These results have been numerically verified for frequencies of 15-, 20- and 25-MHz.

The results, shown in Figures 2.8 and 2.9, demonstrate that the observed differences between x- and y-directed dipoles can be, at least qualitatively, explained by bedrock topography. A more quantitative analysis can be performed by comparing reflection amplitudes of the two dipole directions. To determine the amplitude strength of the bedrock reflection the following steps were applied. For each individual trace, the first peak of the interface reflection was picked manually. Then, a window with the length of 50 ns was applied below the prior picked onset of the reflection to capture the envelope automatically. The amplitude values inside the window are transformed to absolute values and finally, the 95^{th} percentile of the entire window is calculated for each trace separately. This procedure allows us to extract an amplitude strength close to the maximum, which is less affected by outliers. Additionally, we smoothed the 95^{th} percentile values along the profile with a moving average filter and the span of 15. In the following, a section of 50 samples per trace were transformed to absolute values, the 95^{th} percentile calculated and smoothed. The ratio is assessed by dividing the 95^{th} percentile of the x-directed dipole profile by the y-directed dipole values. This approach enables us to evaluate relative amplitude values.

Figure 2.10 shows the amplitude ratios for the 15- and 25-MHz field data and the 20-MHz modeled data. There are considerable differences between the three amplitude curves. In the north-western end of the profile, the ratios of the field data sets (15- and 25-MHz) are similar in magnitude, but exhibit strong localized fluctuations in the south-eastern part. Since we are comparing ratios of the individual x- and y-directed profiles recorded with the same frequency, attenuation effects related to the operation frequency are largely eliminated. Instead, the observed variations must be attributed to differences in equipment handling during acquisition, and, more importantly, to different sizes of the Fresnel zones associated with the 15- and 25-MHz antenna pairs. The size of the Fresnel zones affect the reflection amplitudes, due to small-scale undulations of the bedrock topography and out-of-plane effects. Interestingly, the amplitude ratios of the synthetic data exhibit also considerable fluctuations. Since equipment and out-of-plane effects can be excluded for the synthetic data, these variations must be attributed to focusing and defocussing effects at the small-scale undulations of the bedrock topography shown in Figure 2.7. Nevertheless, the individual curves support the visual differences seen in the Figures 2.3 to 2.5 and 2.8. With minimal deviation, the ratios of the observed data are larger than 1.0 and the median ratios are 3.3 and 3.13 for the 15- and 25-MHz data, respectively. The ratio of the modeled 20-MHz is constantly greater than 1 (median = 3.59), and therefore, shows a stronger bedrock reflection with x-directed dipoles. The modeled glacier ice is homogeneous. Therefore the variations of the 20-MHz ratio can be explained by the underlying bedrock topography and antenna orientation.

Table 2.3: Model parameters for gprMax simulations

Input parameters	
Model extension (length x width x height)	701.5 m x 80 m x 355 m
Cell discretization	0.5 m
Perfectly Matched layer width	20 cells
Nominal antenna frequency	20 MHz
Dipole separation	5 m
Trace length	3500 ns
Spatial sampling	0.5 m

Table 2.4: Media parameter for numerical model of the Glacier d'Otemma based on Giannopoulos (2005), Grimm et al. (2015), Reynolds (2011), and Takei (2007)

Constitutive parameter	Air	Temperate Ice	Granite
Static relative permittivity ε_{rs}	1.0	3.2	6.0
Static conductivity σ (Siemens/meter)	0.0	$5.0e^{-8}$	0.001
Relative permeability μ_r	1.0	1.0	1.0

2.7 Discussion

Geophysical surveys on large ice bodies can be logistically challenging and time consuming. Therefore, GPR data are usually acquired with only one dipole antenna orientation either parallel or perpendicular to the survey direction. As demonstrated in Figures 2.3 to 2.5, the GPR images may be inconclusive, when a campaign is performed primarily with y-directed dipoles, but very good results can be achieved with an x-directed dipole orientation.

Dominant bedrock reflection amplitudes were measured for all profiles with a x-directed dipole setup (Figures 2.3 to 2.5). For y-directed dipole configurations, the ice-bedrock reflection diffuses into a broad scatter cloud with a variable degree of coherence. Nobes (1999) proposed internal structures such as closed crevasses to be the cause for the directional dependence of the reflection amplitude. However, due to the smooth topography of the Glacier d'Otemma no crevasse fields are present in our survey area. Additionally, no compelling evidence for macroscale closed or open fractures can be recognized in the GPR profiles.

A widely accepted cause for scattering in ice bodies is anisotropy originating from directional changes in electrical permittivity. Differences in received signal strength can occur due to anisotropic

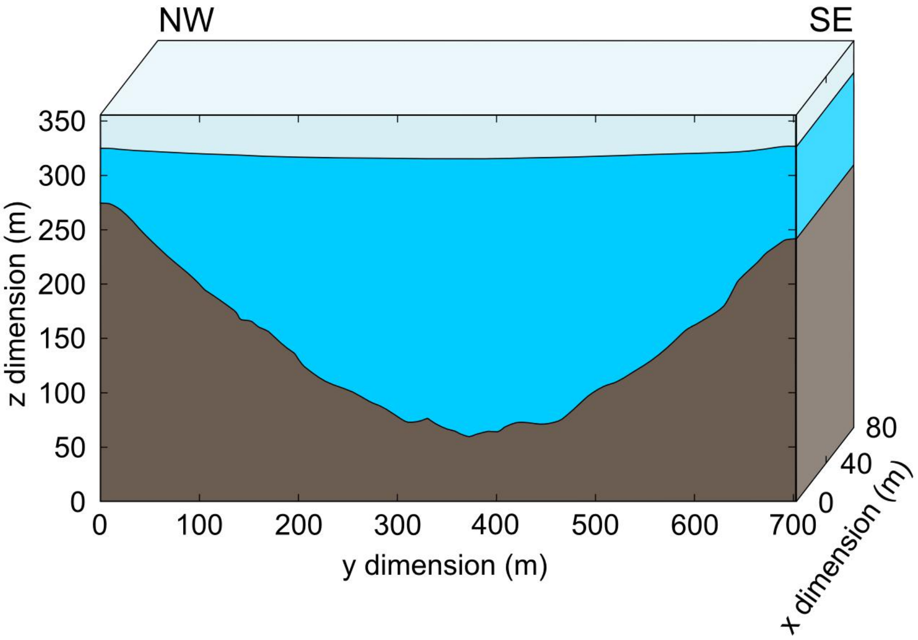

Figure 2.7: Geometry model for gprMax. Y-Z plane based on 25-MHz x-directed dipole across profile data (Figure 2.4A) and extended horizontally into the x dimension.

ice crystal alignments or preferentially orientated air and water bubbles. Drews et al. (2012) and Matsuoka et al. (2012b) showed that such a type of anisotropy results in an azimuthally dependent amount of scattering. One may therefore argue that the decreased bedrock reflection amplitudes in the y-directed data are the result of scattering losses within the temperate ice body. In fact, all across profiles in Figures 2.3 to 2.5 exhibit considerable scattering within the uppermost 100 to 150 m and in the distance range -200 to 0 m, whereby the amount of scattering is more pronounced in the y-directed data. The origin of the increased scattering is unknown, but we speculate that this is caused by an increased amount of water in this portion of the temperate ice body.

The overall amount of scattering is significantly smaller in the same depth range at distances between 0 and approx. 150 m, which could be indicative of a reduced amount of water. If the bedrock reflection amplitude was governed predominately by scattering losses, one would expect high amplitude ratios for x- and y-directed data at distances between -200 and 0 m, and lower ratios between 0 and 150 m distance. As shown in Figure 2.8, this is not the case. Although, the amplitude ratios for the different frequencies exhibit substantial discrepancies, it seems evident that the ratios are even higher between 0 and 150 m. Therefore, scattering losses cannot be the controlling factor for the variations of the bedrock reflection amplitudes in Figures 2.3 to 2.5.

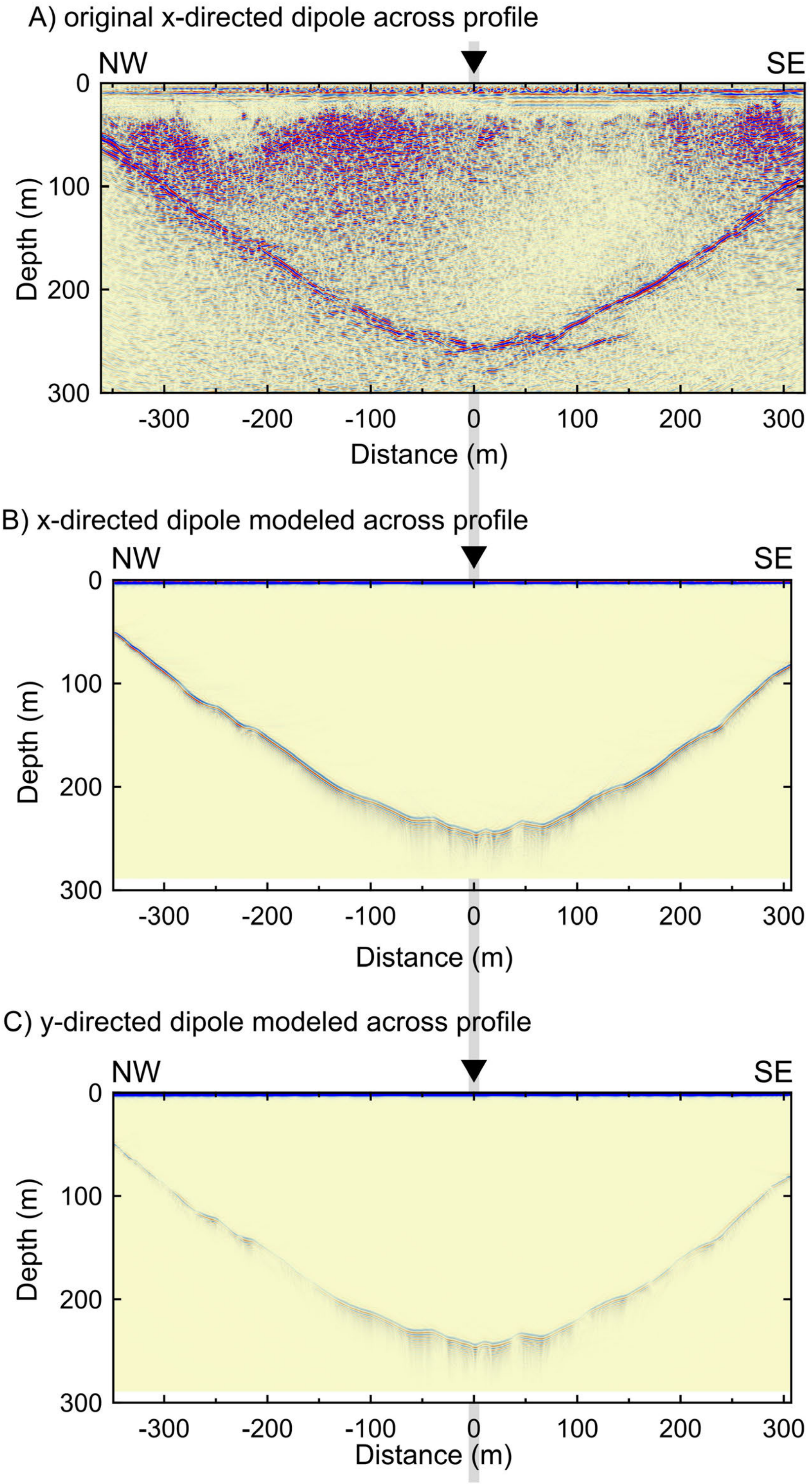

Figure 2.8: Modeled 20-MHz x- (B) and y-directed (C) across profiles. A) displays the 25-MHz x-directed across profile, which was used for the bedrock geometry model generation in gprMax.

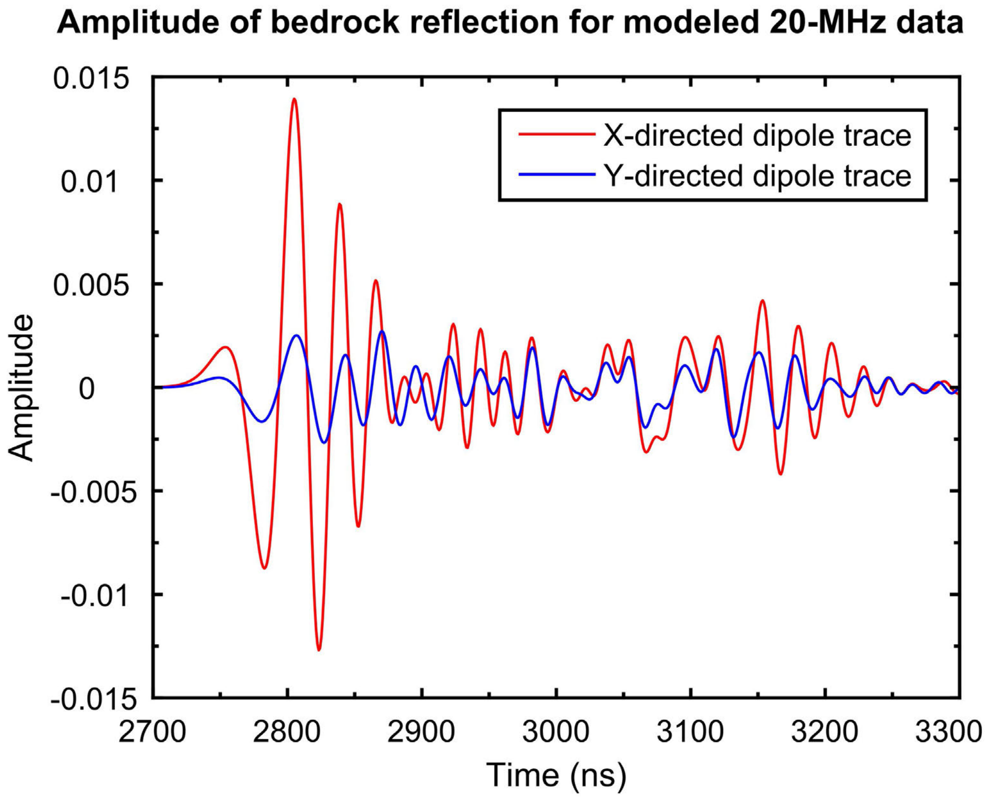

Figure 2.9: Modeled 20-MHz traces with x- (red) and y-directed (blue) dipole antennas showing the bedrock reflection. Antenna position at 0 m of the across profile in Figure 2.8.

Our numerical modeling results demonstrate at least qualitatively that the orientation of the antenna dipoles with respect to the bedrock topography is crucial factor for the quality of the bedrock reflections. This should therefore be a key criteria for an effective survey design.

Obviously, for glacier areas that are confined by steep valley walls, the preferred profile orientation should be aligned with the line of strike of the valley flanks. The choice of an appropriate recording configuration is less clear in plateau or saddle areas, where the subsurface topography is unknown. In such situations, it would be advisable to acquire two data sets with orthogonal antenna pairs. This can be achieved most efficiently with a multi-component recording system. We are currently testing such a system, and its performance will be the subject matter of a follow-up paper. If one set of the dipole antennas is aligned with the preferred orientation, the GPR profiles will show the best possible image of the bedrock topography. If this is not the case, one may consider the pseudoscalar approach advocated by Lehmann et al. (2000) of combining the two recordings into one favorable signal.

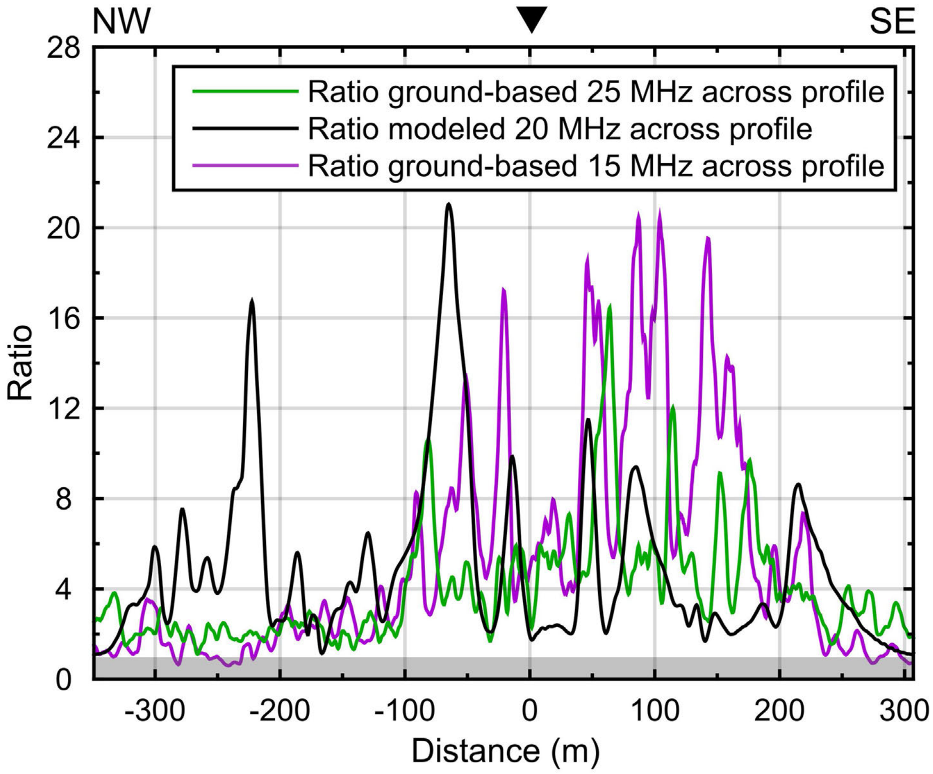

Figure 2.10: Amplitude ratios of the x- and y-directed dipole bedrock reflection. Ratios of observed data are shown in purple (15-MHz) and green (25-MHz). Ratio of modeled 20-MHz data is presented in black.

2.8 Conclusions

We acquired a comprehensive data set of GPR profiles on a temperate mountain glacier for the purpose of investigating the directional dependence of GPR dipole antennas on the quality of bedrock reflections. Helicopter-borne and ground-based profiles, both across and along the glacier flow, revealed a substantial difference in bedrock reflection amplitude, depending on the GPR dipole antenna orientation. This observation is independent of the frequencies used and the GPR systems employed. Our results show a considerably better data quality with median ratios above 3, when using x-directed dipoles (parallel to the glacier flow) compared with a y-directed dipole antenna setup (perpendicular to the glacier flow).

The numerical simulations based on the GPR-derived bedrock topography of the Glacier d'Otemma confirmed that the directional dependence of the ice-bedrock interface reflection amplitude is governed primarily by the shape of the glacier bed. Other features, such as water inclusions, air bubble or ice crystal anisotropy may also influence the amplitudes of the received GPR signals. We observed that scatter clouds in the shallow sections of the ice body, likely caused by some of these features, are more pronounced on profiles with y-directed antenna orientations. These effects are much smaller than those generated by the bedrock topography.

We conclude that the directional amplitude dependence of the GPR antenna orientation is the primary effect that must be considered during experimental design. On glaciers confined by valley walls, the preferred orientation of the dipole antennas should align parallel to the striking direction of the side walls. If the general topography underneath a temperate glacier is unknown, such as in saddle areas or divergence zones, a multi-component setup with two dipole sets perpendicular to each other is advisable. Our findings are particularly important for helicopter-borne campaigns, where the antenna dipole orientation is usually constrained by the system setup and cannot be changed easily.

2.9 Acknowledgments

Financial support was provided by ETH Zurich, Swiss Geophysical Commission and the Swiss Competence Center for Energy Research - Supply of Electricity (SCCER-SoE). Data acquisition has been enabled by the Laboratory of Hydraulics, Hydrology and Glaciology (VAW) of ETH Zurich and GEOSAT SA, Sion. We acknowledge P. Becker and C. Jordi for their support during the field campaigns. Processing of our data was facilitated by CREWES MATLAB software (Margrave, 2003) and we thank A. Cheng and three anonymous reviewers for constructive comments that improved the manuscript.

Chapter 3

Glacier bed surveying with helicopter-borne dual-polarization ground-penetrating radar

Abstract

Traditionally, helicopter-borne ground-penetrating radar (GPR) systems are operated with a single pair of bistatic dipole antennas to measure the thickness of glaciers. We demonstrate numerically that the directivity of the radiation pattern of single airborne dipoles does not correspond to an ideal full-space solution, if the antennas are employed at typical flight heights. These directionality effects can degrade the quality of the subsurface images significantly, when the GPR antennas are orientated unfavorably. Since an adjustment of the antenna orientation is impractical during flight, we have developed a novel dual-polarization helicopter-borne GPR system consisting of two orthogonal pairs of commercial antennas in broadside configuration. To overcome the image quality deficits of the individual channels, we apply a pseudo-scalar approach in which we combine the data of both polarizations. Results of helicopter-borne GPR surveys on two alpine glaciers in Switzerland reveal more coherent bedrock reflections in the summed data compared to single dipole pair profiles. Generally, the dual-polarization setup is more suitable than single antenna systems, because it is more versatile and less prone to directional effects caused by the placement of the dipole antennas in relation to undulating subsurface reflectors.

Accepted for publication in Journal of Glaciology: Langhammer, L., Rabenstein, L., Schmid, L., Bauder, A., Grab, M., Schaer, P. and H. Maurer. Glacier bed surveying with helicopter-borne dual-polarization ground-penetrating radar.

3.1 Introduction

Estimating the present mass of glaciers, ice caps and ice sheets is a key element for global sea level rise predictions, regional strategies for managing water resources and local hazard assessment in high mountain environments. Ground-penetrating radar (GPR) measurements (Plewes and Hubbard, 2001; Woodward and Burke, 2007), ice thickness modeling techniques (Huss and Farinotti, 2012; Farinotti et al., 2009b, 2017) and satellite observation (Hirt, 2014) have traditionally been the tools of choice for assessing the bedrock topography and determining ice volume. GPR systems in particular provide in-situ data and are also referred to as RES (Radio-echo sounding) techniques. They can be operated ground-based or air-borne. Airborne GPR systems mounted on fixed-wing aircrafts are common for large-scale surveys in the polar regions and over wide glaciers (Conway et al., 2009; Li et al., 2013; Shi et al., 2010; Watts and Wright, 1981; Zamora et al., 2009), but in high-mountain environments with complex topography, helicopter-borne systems are more suitable because of better maneuverability (Kennett et al., 1993; Blindow et al., 2012).

One of the earliest attempts to measure bedrock topography underneath temperate glaciers with helicopter-borne GPR was carried out by Kennett et al. (1993). They used an 8 MHz GPR system that was mounted on a H-shaped construction consisting of fiberglass poles and an aluminum mast. On Svartisen Glacier, Norway, bedrock reflections down to 350 m depth were recorded. In recent years, low-frequency helicopter-borne GPR systems have been used more frequently, particularly in mountainous environments. For example, Blindow (2009) developed the UMAIR (University of Münster Airborne Ice Radar, later referred to as BGR-P30 system; Rückamp and Blindow, 2012), a broadband antenna system with a 30 MHz center frequency. During surveys on the Southern Patagonian Ice Field, Chile, bedrock reflections down to 800 m in temperate ice were recorded. Later, the UMAIR/BGR-P30 system was used in campaigns on the King George Island Ice Cap, Antarctica, (Rückamp and Blindow, 2012), the Colonia and Nef Glacier in Chile, (Blindow et al., 2012) and the Gorner Glacier, Switzerland, (Ryser et al., 2013). Based on the UMAIR/BGR-P30 concept, a more lightwight and higher frequency (50 MHz) airborne GPR (named 'Carlina') was developed by Casassa et al. (2014). They mapped the bedrock topography of the Juncal Norte Glacier situated at altitudes above 5750 m. Gacitúa et al. (2015) operated a helicopter-borne GPR on the Olivares Alfa Glacier, Chile. The system consisted of a hanging dual bow-tie dipole antenna with a center frequency of 50 MHz. They achieved a maximum penetration depth of up to approximately 130 m and found distinct temperate and cold ice layers in the Olivares Alfa Glacier. Most modern helicopter-borne GPR systems are pulsed, i.e. a short duration pulse is fed into the transmitting antenna. As an alternative Krellmann and Triltzsch (2012) developed a helicopter-borne stepped-frequency GPR (HERA-G). A series of mono-frequency signals are used to step through the required frequency range.

Most recently, Urbini et al. (2017) developed a helicopter-borne system with a pair of 40 MHz antennas attached to a wooden bird perpendicular to the flight direction. They noted that their data quality strongly depends on the surface roughness and water content of the glacier ice. Similar observations were made by Rutishauser et al. (2016). They published results from a comprehensive survey of approximately 1500 km helicopter-borne GPR profiles acquired in the Swiss Alps. Both systems, the BGR-P30 and the HERA-G system were employed as well as a commercial 70 MHz GPR system with unshielded SUBECHO-40 antennas (Radarteam Sweden AB, 2017) and a GSSI SIR-3000 control unit produced by Geophysical Survey Systems Incorporated (Geophysical Survey Systems Inc., 2017). The GPR systems showed varying degrees of success of detecting the ice-bedrock interface underneath the glaciers in the Swiss Alps. However, the systems were mostly operated on different glaciers, such that a direct comparison of the data quality was difficult. The deepest visible bedrock reflection (DVR) of 613.6 m was measured on the Great Aletsch Glacier with the BGR-P30 system, which was the helicopter-borne GPR system operated with the lowest center frequency. It also provided the highest coverage of traceable bedrock reflections in the GPR profiles with 46.8 % to 68.9 %. Overall, only in 46.2 % of the acquired GPR profiles the bedrock reflection was visible, which highlights the difficulties of helicopter-borne systems operated over temperate glacier ice compared to surveys on cold ice glaciers.

A direct comparison of a ground-based profile with a helicopter-borne profile on the Allalin Glacier revealed a generally lower data quality of the helicopter-borne data (Rutishauser et al., 2016). This is likely caused by geometrical spreading of the electromagnetic waves (Reynolds, 2011) and a change in radiation pattern, when the GPR antenna is elevated and therefore further away from the target. Finally, it has been observed that the orientation of GPR antennas has a substantial effect on the data quality. Moran et al. (2003) and Langhammer et al. (2017) showed the importance of the antenna axis alignment in relation to the underlying subsurface topography. This is shown in Figure 3.1 adapted from Langhammer et al. (2017). It displays two coincident ground-based profiles measured across the Otemma Glacier, Switzerland, with 25 MHz GPR antennas. The profiles were acquired with both antennas either oriented parallel (Figure 3.1a) to the glacier flow or perpendicular (Figure 3.1b). The quality of the bedrock reflection differs strongly between the profiles. Similar observations were made for other helicopter-borne data (Langhammer et al., 2017). For valley-type glaciers, the antenna axis should be aligned parallel to the strike direction of valley walls (usually parallel to the glacier flow) to obtain optimal results (Figure 3.1a), but for plateau-type glaciers and saddle areas with undulating bedrock topography it becomes difficult to determine a suitable antenna orientation.

Based on our review of helicopter-borne GPR systems employed on temperate glaciers, we can draw three important conclusions.

1. It is advisable to employ low-frequency antennas of 25 MHz or less for mapping the bedrock

topography underneath temperate Alpine glaciers.

2. The high velocity contrast between air and ice strongly influences the propagation of the electromagnetic waves and should be considered appropriately during data processing.

3. The antenna orientation has a major influence on the data quality.

To address these problems, we have developed a novel GPR system and modified the processing flow appropriately. After a brief discussion of 2D and 3D antenna radiation patterns of helicopter-borne systems at typical flight heights, we introduce our AIR-ETH system (Airborne Ice Radar ETH Zurich). One of its unique features is its capability of recording GPR dual-polarization data. We outline, how such a system can be realized using standard commercial components. Besides providing details of the technical setup, we propose a strategy, how helicopter-borne dual-component data can be processed. The performance of our acquisition and processing strategy is finally demonstrated with field examples from typical plateau and valley glaciers in the high-mountain environment of the Swiss Alps.

3.2 Dipole radiation pattern

3.2.1 2D representation

In conventional glaciological GPR surveys of the bedrock topography, only one transmitting and one receiving GPR antenna are used. They are usually placed in broadside or end-to-end configuration and transported with a fixed orientation along the survey line. As shown in Langhammer et al. (2017), the orientation of the GPR antennas is a crucial parameter to consider for detecting the bedrock topography and can influence data quality significantly. This is caused by the specific shape of GPR antenna radiation patterns. For helicopter-borne applications, the antennas can be approximated with infinitesimal dipoles. Engheta et al. (1982) calculated the analytical far-field solution for an infinitesimal dipole, which was later advanced by Arcone, 1995. The analytical solution can be used to calculate the 2D radiation pattern for a dipole either placed in a full space (i.e. when the helicopter flies at a high altitude) or at an interface between two dielectric media (i.e. for ground-based surveys). Generally, the H-Plane corresponds to the plane perpendicular to the dipole axis, while the parallel plane is referred to as E-Plane. Figure 3.2 shows the downward far-field radiation pattern calculated analytically of an electromagnetic infinitesimal dipole in a full space and the numerical results for antenna heights of 1 m, 20 m and 40 m above a half space consisting of air and ice. For solving the analytical equations, we used an index of refraction $n = 1$ for air and $n = 1.31$ for ice and a frequency (f) of 20 MHz. The numerical radiation pattern were generated with the finite-difference time-domain electromagnetic simulation software gprMax (Giannopoulos, 2005). Further details about the simulation and the parameters used can be found

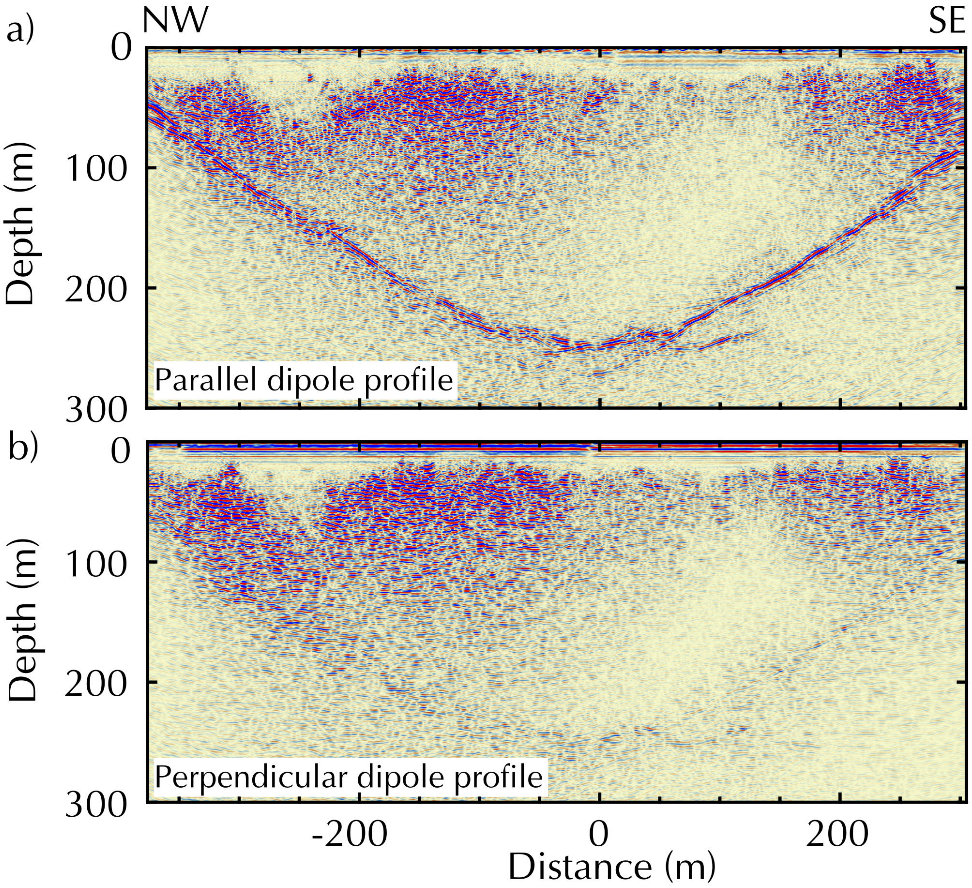

Figure 3.1: Ground-based 25 MHz profile cross the Otemma Glacier with antenna axis aligned parallel to the strike direction of the valley walls (a) and perpendicular to it (b). Adapted from Langhammer et al. (2017)

in Langhammer et al. (2017).

The radiation patterns in Figure 3.2 are area normalized in the H-Plane, such that the comparison of the distinct distribution of the amplitude is possible. In full space the radiation pattern takes the shape of a doughnut with highest amplitudes perpendicular to the dipole axis and very low amounts at the ends of the antenna. Placing the dipole close to an interface e.g. air and ice, changes the energy distribution of the amplitude along the wavefront as seen in Figure 3.2, because of the differing geophysical parameters of the two media. At 1 m distance from the surface and at approximately 140° and 220° in the H-Plane, high amplitude regions are formed in contrast to the uniform pattern of the full space solution. In the E-Plane side lobes occur and nulls are observed at approximately 140° and 220°. By lifting the dipole away from the half space interface the radiation pattern shifts from an ideal half space curve towards the full space solution. It is important to notice that even with the dipole 40 m above the ground the radiation pattern does not correspond to the full space representation. This is caused by the generally low antenna frequencies (e.g. 25 MHz) and therefore the long wavelength of 12 m in air and approximately 6.68 m in temperate ice. Typical flight heights of 10 to 40 m above ground correspond thus only to a few wavelengths. Recent work by Diamanti and Annan (2013) showed that the transition to far-field behavior typically appears at 10 wavelengths. Higher amplitude regions can still be observed at approximately 150° and 210° in H-Plane for 40 m antenna elevation (Figure 3.2). We conclude, that for helicopter-borne GPR measurements neither the full space nor the half space solution are applicable as long as the antennas are transported close to the ice surface.

3.2.2 3D interpolation and pseudoscalar wavefields

We demonstrated that the radiation pattern for 20 MHz dipoles placed reasonably close ($\leqslant$ 40 m) to the ice surface still exhibit high amplitude side lobes. For our helicopter-borne surveys this observation causes significant problems, since regions perpendicular to the antenna axis at an angle of approximately 140°-160° and 200°-220° will be illuminated with higher amplitudes than the area directly underneath (180°) the antennas. Additionally, due to the nature of dipole antennas, less energy is radiated parallel to the axis. To illustrate this, we interpolated the 2D H- and E-plane into 3D by rearranging the analytical expressions by Engheta et al. (1982) to

$$A \quad = \quad [(S_1 - S_0)\sin^2\phi + S_0]^{\frac{1}{2}} \tag{3.1}$$

with A being the amplitude along the 3D surface, S_0 and S_1 the power of the 2D planes and $0<\phi\leqslant 2\pi$. The results are shown in Figure 3.3 (left panel) as single dipole patterns for the full space and 1, 20, 40 m above the ice surface.

Based on Lehmann et al. (2000), electromagnetic field components can be summed to simulate a more symmetric radiation pattern; called "pseudoscalar" wavefields. This can be achieved by utilizing two broadside transmitter and receiver antenna sets, which are perpendicular to each other. Their signals can be summed to enhance the signal-to-noise ratio, and more importantly, to tune the radiation characteristics. The amplitude of the 3D summed pseudoscalar wavefields are visualized in Figure 3.3. We summed two interpolated 3D single dipole radiation pattern; one with the H-plane parallel to the x-axis and the other one 90° rotated (H-plane parallel to y-axis). With increasing height, the highest amplitudes are observed underneath the dipoles and the effect of the side lobes decreases. Based on the results shown in Figure 3.3, we conclude that an acquisition system with two sets of orthogonal antenna pairs is expected to improve the data quality significantly. This motivated us to build the AIR-ETH system, described in the next

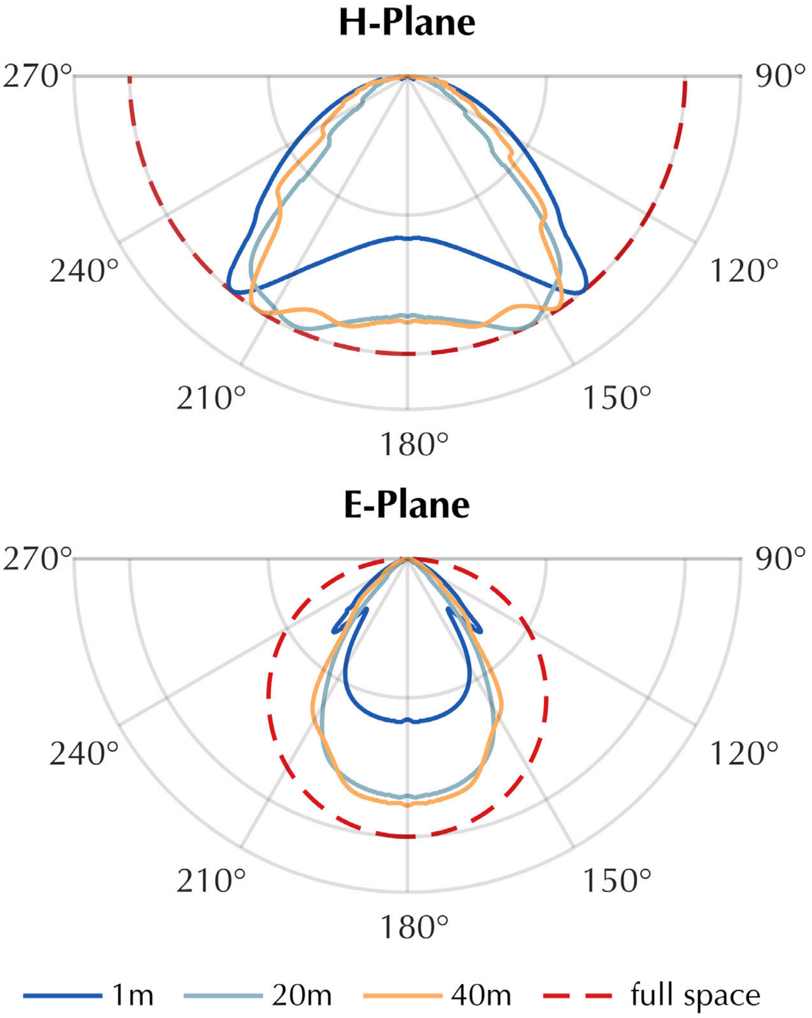

Figure 3.2: Polar plots (H- and E-Plane) of radiation pattern of an infinitesimal dipole in full space (air) and placed on a half space interface (air - ice). Only lower half of polar plot is displayed. Analytical full space solution (dotted) and numerical curves for 1 m, 20 m and 40 m antenna height (solid lines). Curves are area-normalized.

section.

3.3 AIR-ETH system setup

The system consists of commercial GPR components (Table 3.1), which are mounted on a wooden frame and carried underneath a helicopter (Figure 3.4 c). It is hanging from an approximately 14

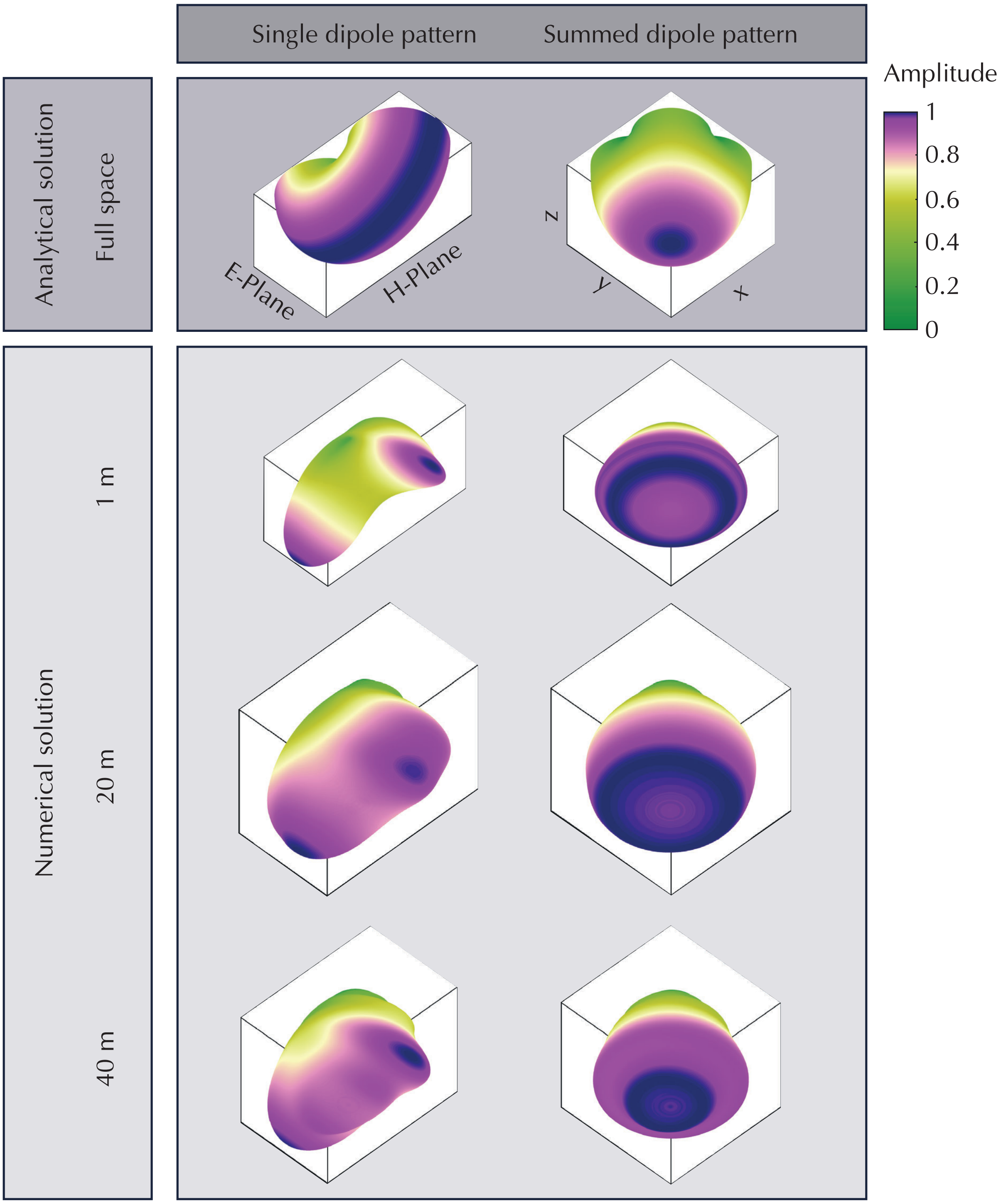

Figure 3.3: Single (left) and summed (right) interpolated 3D amplitude radiation pattern of an infinitesimal dipole in full space (air) and placed on a half space interface (air - ice). View angle from underneath, looking upwards. Color scale nonlinear.

Table 3.1: Helicopter-borne GPR system components

Components	Details
Frame material	Glued oak and spruce bars
Length x Width x Height	5.0 x 4.8 x 0.7 m
Weight	approximately 250 kg
GPR	NIC-500X and 4x pulseEKKO 25 MHz antenna
GPR antenna separation	4 m
Positioning	3 x Differential GNSS (Javad alpha, Omnistar G5Ant)
Laser altimeter	Jenoptik LDM-301
Power consumption	approximately 85 W
Distance to helicopter	approximately 14 m

m rope, which can be released in case of emergency, and wings are attached to the back to ensure a stable trajectory during the flight. The wooden frame is constructed as a connector system (Figure 3.4b and c). Individual parts of the GPR setup are the NIC-500X control unit and four 25 MHz unshielded dipole antennas build by Sensors & Software (2017). Other frequencies can be employed as well, since the system consists of interchangeable antenna elements. The transmitter and receiver antenna of the individual pairs are attached in broadside configuration, but both pairs are placed perpendicular to each other to collect dual-polarization data during the survey. The GPR hard- and software, located in the box on the platform in the middle of the frame (Figure 3.4a and b), can be controlled via any device with a browser and a wireless connection (e.g. labtop, tablet) while sitting in the helicopter. Additionally, three differential GNSS receivers are attached to the corners of the frame for determining the position as well as pitch, roll and yaw of the system during flight with a temporal sampling rate of 1 Hz. To measure the height of the system above the surface, we installed a LDM-301 laser altimeter. For navigation purposes, the GNSS position and elevation above ground is simultaneously displayed on a screen in the helicopter cockpit. Finally, a downward looking GoPro camera is attached to the platform to collect images of the space underneath the system. The system and the transmitter and receiver antenna modules are powered by two 12 V 38 Ah batteries with enough energy to operate the system for ten hours.

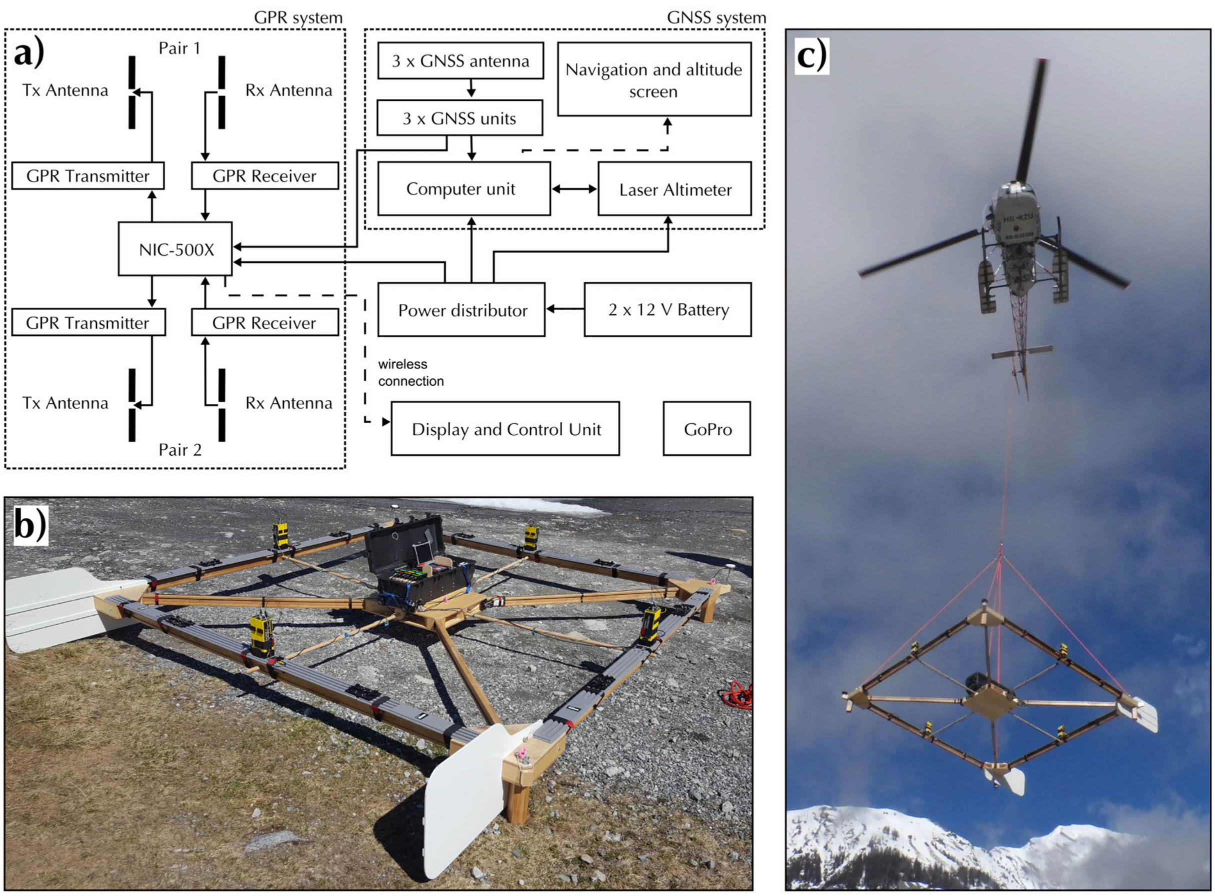

Figure 3.4: Technical sketch of the helicopter-borne dual-polarization GPR system (a). For each dipole pair, the transmitter and receiver antenna are mounted facing each other and in parallel position. The AIR-ETH system on the ground (b) and during take off (c).

3.4 Data processing and results

To demonstrate the capabilities of our helicopter-borne dual-polarization GPR system, we will show results from two glaciers in Switzerland with different morphologies. First, we present the case study of the Glacier de la Plaine Morte (hereby referred to as Plaine Morte Glacier). Here, we describe the GPR data processing steps and highlight the bedrock reflection differences in the individual channels along the profiles. Second, we present a GPR data set from the debris-covered Oberaletschgletscher (hereby referred to as Oberaletsch Glacier) to demonstrate the performance of the AIR-ETH system in a more complex environment.

3.4.1 Case Study 1: Plaine Morte Glacier

The Plaine Morte Glacier is situated between 2400-3000 m a.s.l. in the western Swiss Alps (Figure 3.5a). With an area of 7.5 km^2 in 2016, it is the largest plateau glacier in the European Alps (Bauder, 2017). Over 90 % of the glacier is located at an altitude of 2650-3000 m a.s.l. and thus has a shallow surface slope of less than 4°. It drains into a short glacier tongue towards the North. In recent years, the glacier has been entirely snow free in summer, because of its particular plateau shape and an increasing equilibrium line altitude (Bauder, 2017). The flat and undulating surface of the Plaine Morte Glacier gives ambiguous indications about the underlying bedrock topography. As a result, it becomes challenging to determine the preferred orientation of the GPR antennas by looking at the strike direction of the surrounding valley walls. Therefore, we decided to measure the profiles with the AIR-ETH system with its dual-polarization GPR antenna configuration. In spring 2017, we collected several profiles of helicopter-borne GPR data on the Plaine Morte Glacier (Figure 3.5a). Here, we will focus on one cross (W-E) and one longitudinal profile (N-S) for further analysis.

Data processing

In the context of this paper, we will follow the terminology of x- and y-directed dipoles when referring to the GPR antenna orientation (see also Figure 3.5) so that the terminology is irrespective of the survey direction or flight path of the helicopter. Dipoles orientated in x-direction have an approximate axis orientation parallel to the flow direction of the glacier and thus, are parallel to the strike direction of the surrounding valley walls in the tongue area. Consequently, y-directed dipoles are aligned perpendicular to the glacier flow.

During our surveys in the Swiss Alps and the development of the system, we noticed the strong influence of the helicopter type on the strength of ringing noise in the GPR data recorded with the AIR-ETH system. The bigger the helicopter and the closer the GPR system is attached, the stronger is the overlying ringing. We also tested detaching individual parts of the system (GNSS equipment, Laser altimeter, one antenna pair), but concluded that the helicopter is the key noise source in our data sets. Our raw data, displayed as a section of the cross profile on the Plaine Morte Glacier in Figure 3.6a-1 to c-1, is dominated by ringing down to approximately 1500 ns. Strong ringing causes a saturation of the GPR Receiver A/D converter and the incoming signal is clipped. However, the degree and occurrence of ringing can vary, when other GPR systems are employed.

To improve the image quality and to process our dual-polarization GPR data, we have developed in-house routines written in MATLAB and using the CREWES MATLAB software (Margrave, 2003). They include standard GPR processing steps (Table 3.2) and specific modification for our helicopter-borne acquisition (Table 3.3). To localize the recorded profiles, we assign differential GNSS coordinates to the individual traces. A custom software running-average filter (Sensors & Software, 2017) is applied to dewow the data. Then, we transform the GPR data into the industry standard format SEG-Y. Following the pseudoscalar approach (Lehmann et al., 2000), the x- and y-directed dipole data sets are summed to create a third set, which is processed in the same manner as the other ones. We statically correct for time zero and apply an amplitude interpolation algorithm based on a third order polynomial function to recover the clipped signal content (Ammann, 2017). Afterwards, the position of the surface reflection is automatically determined by using the system-surface distance measured with the laser altimeter. Depending on the quality and consistency of the laser data, the surface reflection has to be picked manually. To reduce the ringing noise caused by the helicopter, we use a singular value decomposition filter (SVD) with the first two eigenvalues set to zero and a window length equal to the absolute number of traces of the profiles. Furthermore, we apply a bandpass filter with corner frequencies of 10 and 40 MHz. The trace spacing is equalized to 1 m by assigning the nearest-neighbor trace to the binning center. Further processing includes a reversed-time migration to collapse diffractions and to locate dipping layers accurately in the subsurface. For this step, we generate a half space model with an air velocity of 0.3 m ns^{-1} and a uniform ice velocity of 0.167 m ns^{-1} (Reynolds, 2011). As a final step, the GPR profiles results are displayed as depth versus distance and the energy signal content of the later arrivals is enhanced by applying a time-variant gain function (e^{at}, a is a scaling factor and t denotes time). The gain parameters and color scale of the x- and y-directed dipole profiles are identical to compare the performance of the individual channels. For the summed x- and y-directed profile, the gain parameters are set for best visibility of the bedrock reflection.

Results

Figure 3.6 illustrates the bedrock reflection quality in the raw data of the individual channels. Here, we only applied a SVD filter to remove the ringing signal to further analyze the amplitudes of the bedrock reflection along the profile. After deleting the ringing, the clipped signal content becomes visible as light horizontal strips in the upper 700-800 ns of Figure 3.6a, b and c. The surface reflection at trace number 500 is distorted, but better visible in the y-directed dipole data. In contrast, the bedrock reflection is stronger in the x-directed dipole profile at trace number 3200. These differences can be analyzed by comparing the power content along the bedrock reflection interface as a ratio of the x- and y-directed dipole data (Figure 3.7). Gray sections in Figure 3.7 should not be considered, because in these areas the ringing effects dominate the received signal and distort the surface and subsurface reflection amplitudes. In each profile, we picked the interface manually in a window of 50 samples, created a spectrogram for each trace separately and determined the power content (dB Hz^{-1}) for the interface in a range between 10-40 MHz. To smooth the results, we merged ten traces to create a segment and used the ratio of the x- and y-directed data for further analysis. We observed that in case of the Plaine Morte Glacier, there is no dominantly stronger channel. The image of the bedrock topography varies in quality within the individual channels and in comparison to each other. While the bedrock reflection is visible in the deeper parts of the glacier in the x-directed dipole data between 2000-3000 ns (Figure 3.6 a), the y-directed dipole profile shows stronger reflections at the bedrock rise at trace numbers 2100-2500 (Figure 3.6 b). The ratio varies in selected areas from 0.4, which indicates an up to 2.5 times stronger power in the y-directed dipole profile, to 1.5 and therefore a stronger bedrock reflection amplitude in the x-directed dipole data. However, the horizontal reflector at traces 1600-1900 is imaged equally well with both polarizations (ratio$\approx$1). The variation of the ratio can be explained by undulations of the subsurface bedrock topography. The Plaine Morte Glacier is atypical for Swiss glaciers and fills rather a plateau than a characteristic u-shaped mountain valley. As mentioned in Langhammer et al. (2017), the polarization of the dipoles determines the sensitivity of the antennas to detect the bedrock dip and strike direction. Operating only one polarization would have been insufficient to obtain optimal results.

The summed x- and y-directed dipole profile is displayed in Figure 3.6c. It can be observed, that the surface reflection is more coherent and the ice-bedrock interface is traceable more consistently below 2000 ns. The uprise in the subsurface at trace 2100-2500 is well defined in space (Figure 3.6c-2) and the overall bedrock reflection is more dominant in comparison to the background noise.

Figure 3.8 and 3.9 show the two selected fully processed profiles of the Plaine Morte Glacier. The vertical axis in all processed profiles shows depth below surface. The crossover point of the cross and longitudinal profile is marked with a black triangle and a distance of 0 m. Similar to the results in Figure 3.6, the difference in bedrock reflection quality in Figure 3.8 is apparent, when the x- and y-directed dipole data sets are compared. While the bedrock reflection below 100 m depth is more visible in the x-directed dipole profile, the uprise at approximately -1800 m distance is better defined in the y-directed dipole data. By summing both orientations (Figure 3.8d) a second uprise and hummock at -800 to -1500 m become visible. Additionally, at greater depth and between -1000 m to 500 m distance the coherency and visibility of the bedrock reflection are increased. In all profiles, a diffuse, vertical noise pattern can be seen in the middle section of the cross profile and its intensity does not change with depth. Its origin is unclear.

The processed data of the longitudinal profile are presented in Figure 3.9. The bedrock reflection is generally more coherent and stronger in the x-directed dipole data set, specifically, in the shallower tongue area in which the y-directed dipole data exhibits incoherent scattering. In all three data sets, patches of increased noise or scattering can be observed in 50-100 m depth in the vicinity of the cross over point. At 600 m distance, a migration artifact occurs below 100 m depth and can be recognized by its characteristic hyperbolic pattern. The summed GPR profile (Figure 3.9d) displays an enhanced bedrock reflection especially in the sections of steeply dipping subsurface topography; e.g. at a distance of -350 to -400 m in the North and at 200 - 500 m in the South. We were able to determine the bedrock reflection down to the deepest part of the glacier at approximately 160 m depth.

3.4.2 Case Study 2: Oberaletsch Glacier

As a second example, we chose the Oberaletsch Glacier (19.58 km^2 in 2009) located in the Western Swiss Alps, Switzerland (Figure 3.5b). The Oberaletsch Glacier (2150-3900 m a.s.l.) is a valley-type glacier and flows from North towards the South-East. In 2011, it covered an area of $\sim$17.5 km^2 and had a length of $\sim$9 km (Bauder, 2015). Its tongue is heavily debris-covered (Jouvet et al., 2011) and supplied with supraglacial material from the northern headwalls and its tributary glacier from the West, the Beich Glacier (Paul et al., 2004). In late spring 2017, we measured a dense survey grid of helicopter-borne GPR data on the tongue of the Oberaletsch Glacier to characterize the underlying bedrock topography (Figure 3.5b). Here, we will present a cross and a longitudinal profile to discuss the performance of the AIR-ETH system on a debris-covered glacier.

Results

The bedrock reflection in the cross profile (Figure 3.10) is less coherent compared to the Plaine Morte Glacier, but it is visible between 60 and 180 m depth. High noise clusters can be observed above 100 m depth and between -20 to -80 m and at 100 m distance. Several potential off-plane reflections in the south-western end (e.g. at -200 and -350 m distance) of the profile occur below 100 m depth. The x-directed dipole profile shows a more prominent bedrock reflection at -200 m distance and at shallower depth (Figure 3.10b), whereas the y-directed dipole data image the subsurface syncline at approximately -80 to -160 m to a greater extent (Figure 3.10c). Summing both data sets enhances the coherency and amplitude of the reflection from the ice-bedrock interface (Figure 3.10d).

The longitudinal profile of the Oberaletsch Glacier shows greater differences in data quality, when both orientations are compared (Figure 3.11). Generally, the x-directed dipole data displays a stronger bedrock reflection along the profile. In both, x- and y- directed dipole profiles, several off-plane reflections can be observed at the same location but different depths. They occur preferentially at a distance of $\geq$ 1500 m at the lower end of the glacier, which is situated in a more narrow glacier valley (Figure 3.5b). In the x-directed dipole profile at additional off-plane reflections are visible at approximately -400 m, 100 m and 700 m. In those regions, differentiating

Table 3.2: Data processing parameters

Processing steps in order of execution	Details
Assigning coordinates to traces	Coordinates from differential GNSS
Dewow	pulseEKKO software running average filter
Time-zero correction	correct for arrival time of direct wave
Pseudoscalar method	Summing x- and y-directed dipole data set
Amplitude Interpolation	Interpolation of clipped signal with third order polynomial function
Picking of surface reflection	Laser altimeter distance to surface or manual picking of the surface reflection
Singular-value decomposition filter	Largest two eigenvalues set to zero
Band-pass filter	10-40 MHz
Binning	1 m
Reverse-time migration	Half space of air (v = 0.3 m ns^{-1}) and temperate ice (v = 0.167 m ns^{-1})

between off-plane and in-plane bedrock reflections becomes challenging. Less off-plane reflections are present in the y-directed dipole profile (Figure 3.11c). The bedrock reflection is amplified in the summed x- and y-directed dipole data and off-plane reflections are reduced in amplitude, specifically in the area from approximately -900 to 1300 m distance (Figure 3.11d). However, the high amount of scattering in the shallower section of the tongue (South-East) prohibit the localization of the bedrock reflector. Overall, the helicopter-borne GPR profiles of the Oberaletsch glacier are less coherent and present a higher noise level than the Plaine Morte Glacier data, but we were able to delineate the bedrock topography below 200 m of temperate glacier ice overlain by a heavily debris-covered surface.

3.5 Discussion

Results of the Plaine Morte (Figure 3.8 and 3.9) and Oberaletsch Glaciers (Figure 3.10 and 3.11) demonstrate the amplitude of the bedrock reflection varies significantly in space along the profile and depending on the antenna orientation used. We can account for these deviations by utilizing a dual-polarization GPR system, because predicting the optimal orientation for a single antenna pair a priori is cumbersome.

In the regions of undulating topography or a bowl-shaped subsurface, two antenna sets with

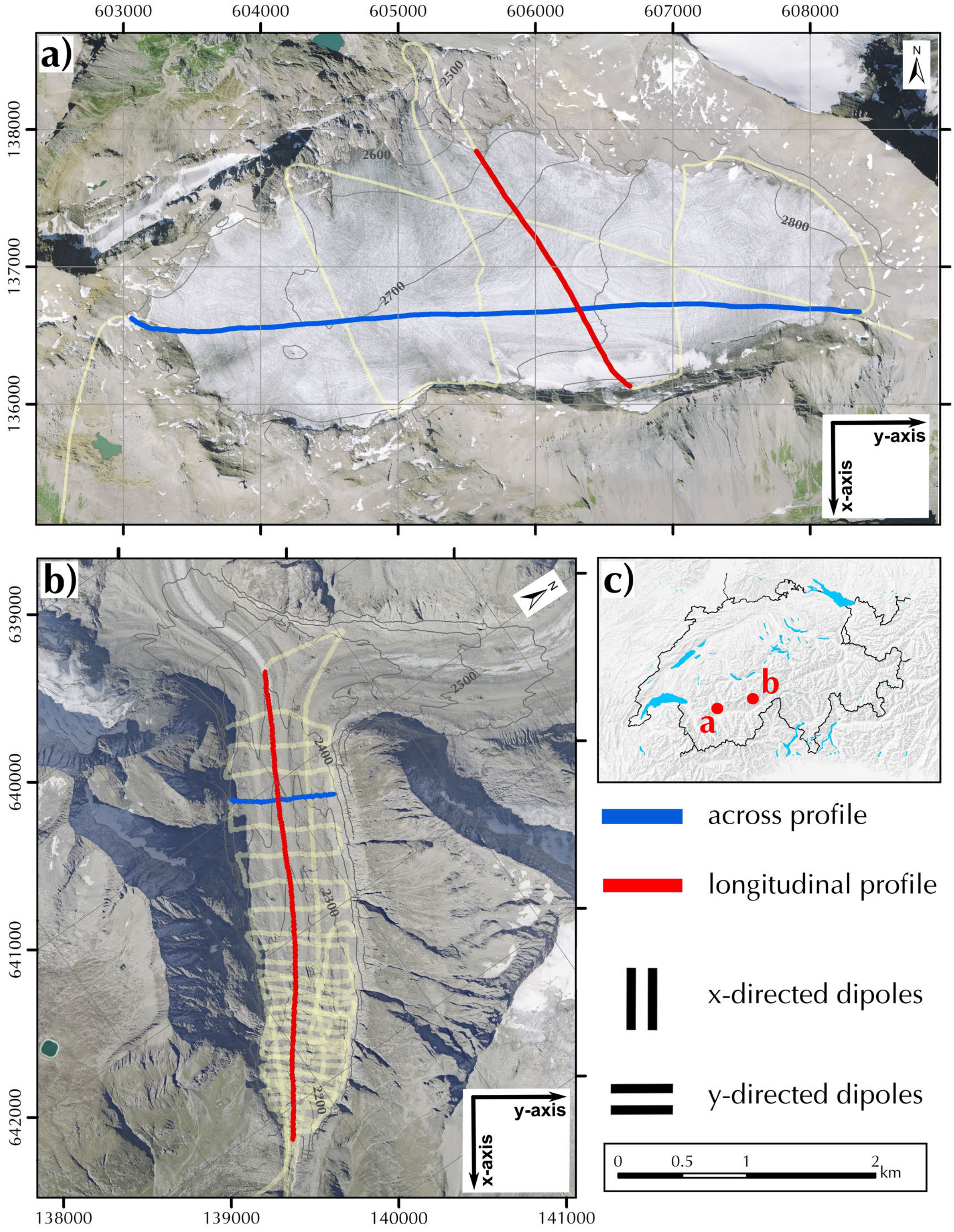

Figure 3.5: Map of the survey area Plaine Morte Glacier (a) and Oberaletsch Glacier (b). Orthophotos © 2017 swisstopo (JD100042). Coordinate system: CH1903-LV03. Location of both glaciers in Switzerland (c). Yellow lines correspond to the entire survey grid measured during the campaign, while the cross (blue) and longitudinal (red) profiles are described in further detail. The x-axis is approximately parallel and the y-axis is perpendicular to the glacier flow direction.

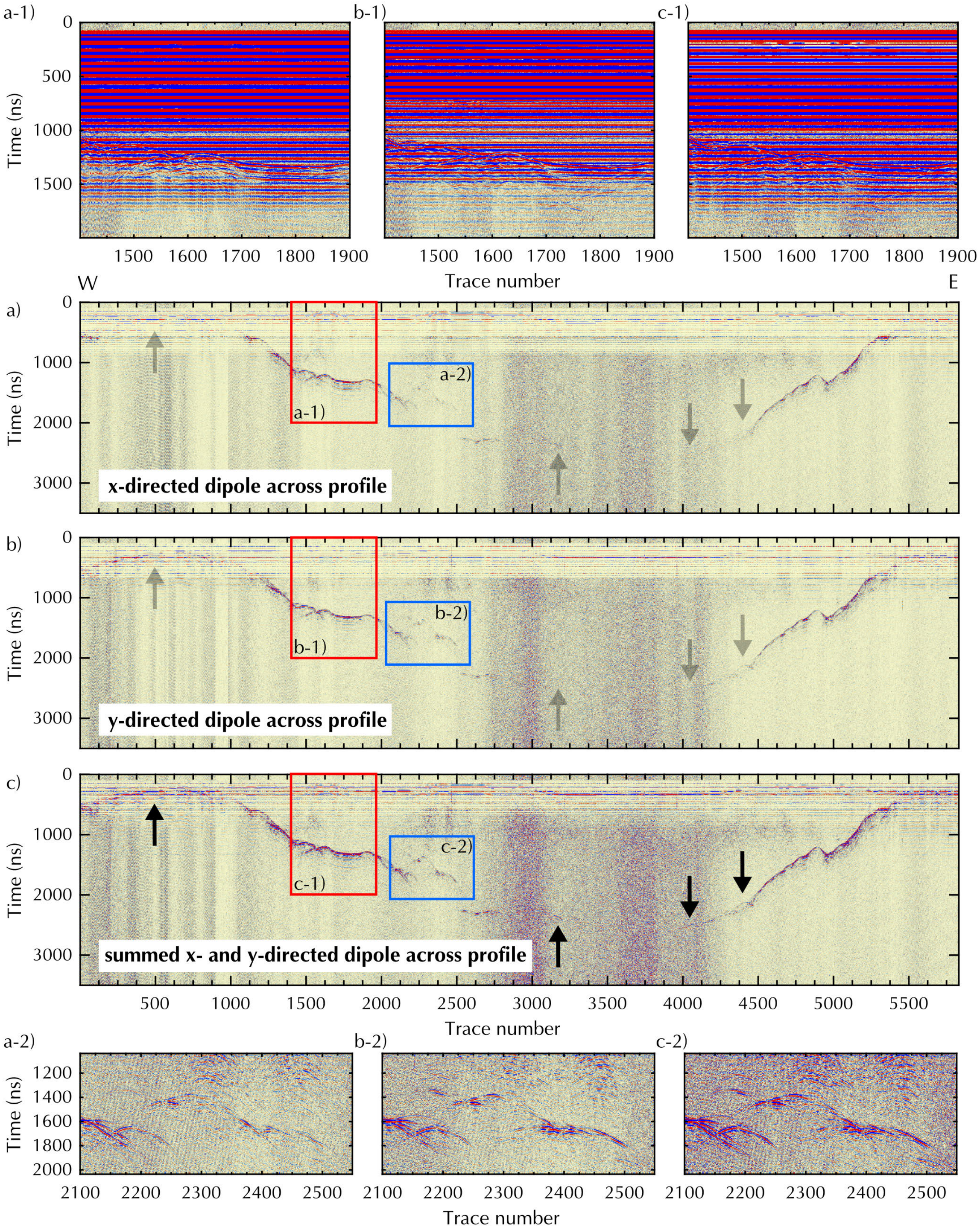

Figure 3.6: Cross profile with only SVD filter applied for x-, y- and summed x- and y-directed dipoles (a-c) on the Plaine Morte Glacier. First enlarged section (a-1 to c-1) displays raw data with ringing (position marked as red rectangle). Second enlarged section (a-2 to c-2) shows area of subsurface uprise to demonstrate enhancement of bedrock reflection due to summing of x- and y-directed dipoles (position marked by blue rectangle). Arrows indicate area of interest.

Table 3.3: Data acquisition parameters

Acquisition parameters	Details
Nominal antenna frequency	25 MHz
Dipole separation	4 m
Sampling rate	4 ns
Trace length	4000 ns
Trace stacking	2

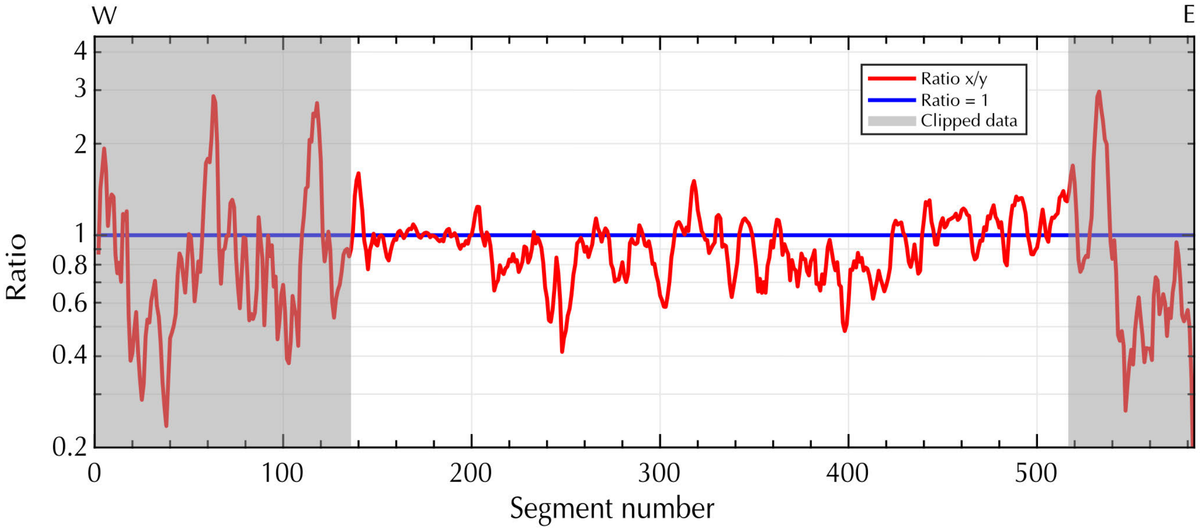

Figure 3.7: Ratio (x/y) of the power content of the x- and y-directed dipole bedrock reflection of the cross profile on Plaine Morte Glacier. Gray areas indicate where the data are predominately influenced by ringing and clipping effects. Y-axis displayed as log-scale. Each segment contains 10 traces.

orthogonal polarization complement each other as seen in the cross profile on Plaine Morte (Figure 3.8d) and the deeper section in the longitudinal profile (Figure 3.9d). Generally, the reflections observed in the summed data appear to be more coherent, which could be related to a certain redundancy of the two polarizations. Thus, summing the traces increases the coherency of the desired bedrock topography signals and suppresses random noise causing an increase in the signal-to-noise ratio.

Scattering effects, caused by air bubbles, water inclusions and debris cover present a severe problem in temperate glaciers. Nobes (1999) and Urbini et al. (2017) noted that scattering from such features could cause directionality-dependent variations. In contrast, by comparing the x-

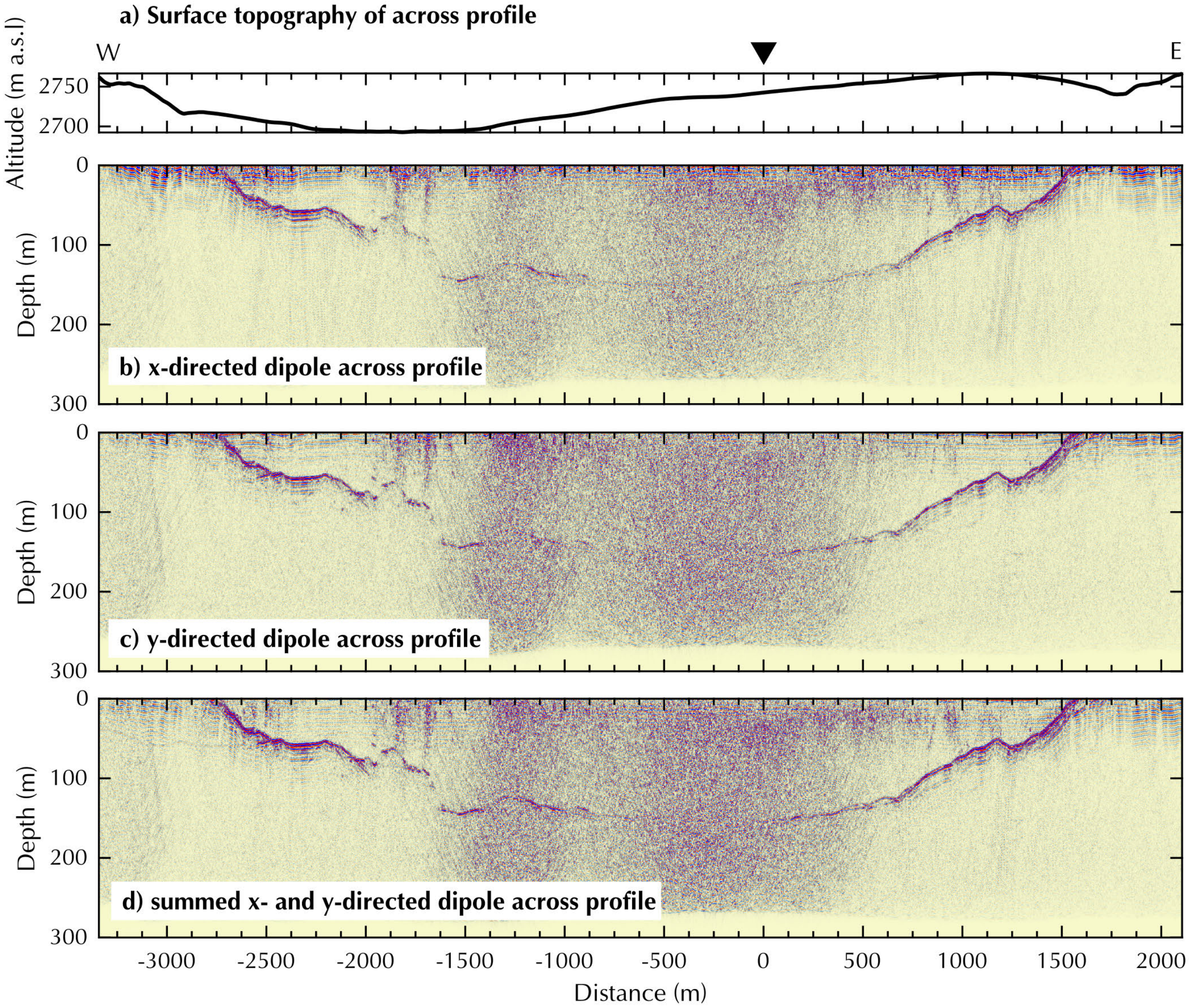

Figure 3.8: Processed cross profile on Plaine Morte Glacier with (a) surface topography, (b) x-, (c) y- and (d) summed x- and y- directed dipoles. Black triangle marks cross-over point. Y-axis exaggeration of profiles 3:1.

and y-directed data for the Oberaletsch cross profile (Figure 3.10), it can be observed that a high amount of scattering rather reduces the amplitude differences of both polarizations and the deviations are enhanced in profiles with less englacial scattering (e.g. Figure 3.11 at 1200 m distance). If background noise or scatter, also caused by crevasses (Bradford et al., 2013), anthropogenic electromagnetic systems or military communications, is present in the single polarization data set, it is likely to be added in the summed x- and y-directed profile as well (e.g. Figure 3.8, -1500 m to 500 m distance). In case of the Oberaletsch Glacier, the scattering can be associated with the

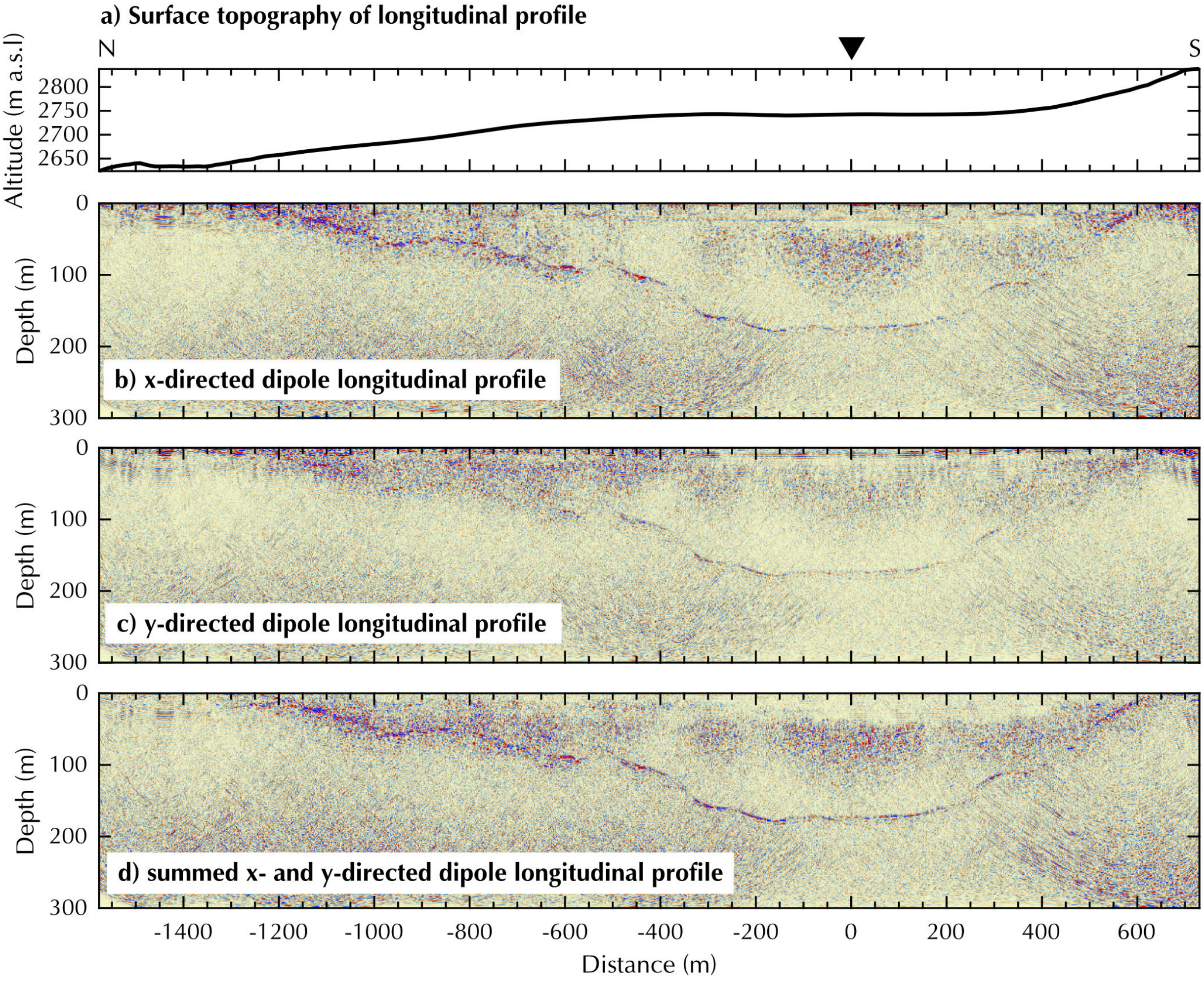

Figure 3.9: Processed longitudinal profile on Plaine Morte Glacier with (a) surface topography, (b) x-, (c) y- and (d) summed x- and y- directed dipoles. Y-axis exaggeration of profiles 1.5:1.

heavily debris-covered surface and the presence of meltwater, since we measured the profiles at the beginning of the summer season. Additionally, we observe several off-plane reflections (Figure 3.11b and c, Figure 3.10b and c at -200 m and - 320 m), which could be associated with a strong undulating subsurface topography or helicopter's vicinity to the surrounding rock walls.

During the past months, we have acquired several hundreds kilometers of data with our new system. Based on our experience, we can offer specific recommendations for optimizing the GPR data quality. A critical component is the length of the rope, which is used to attach the system to the helicopter. A short rope likely increases ringing effects, but the strongest signal distortion

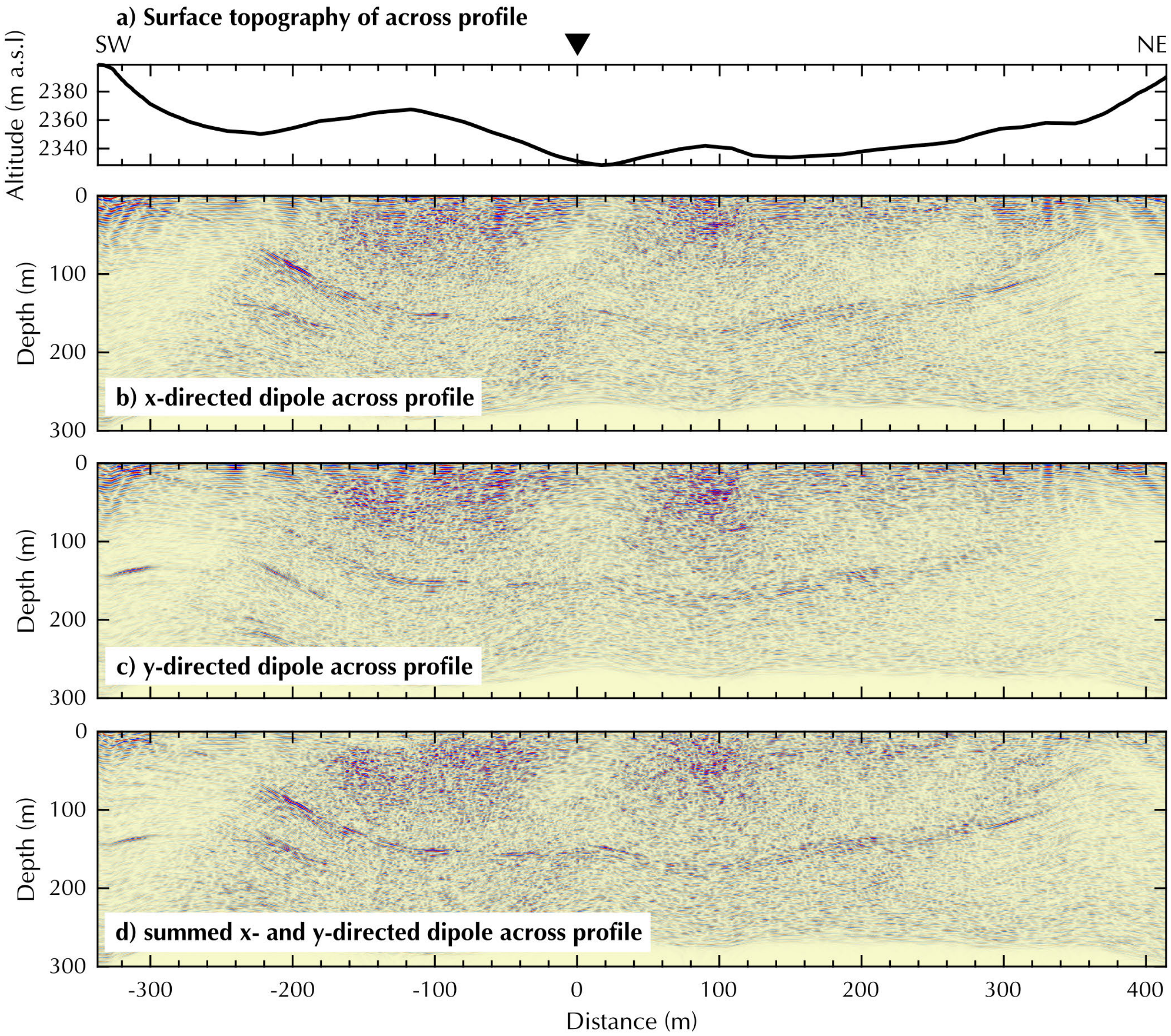

Figure 3.10: Processed cross profile on Oberaletsch Glacier with (a) surface topography, (b) x-, (c) y- and (d) summed x- and y- directed dipoles. Y-axis exaggeration of profiles 1:1.8.

will appear in early portions of the radargrams. They may not obscure bedrock reflections from intermediate and deeper parts of the glaciers. In contrast, a longer rope will decrease the ringing amplitudes, but may lead to a stronger masking of subsurface reflections. An optimal choice is therefore survey dependent. Similar arguments apply to an appropriate choice of the flight height above ground. Lower flight heights allow better coupling to the ground, but will increase the distortion of the bedrock signal due to ringing. We also experienced that the ringing significantly

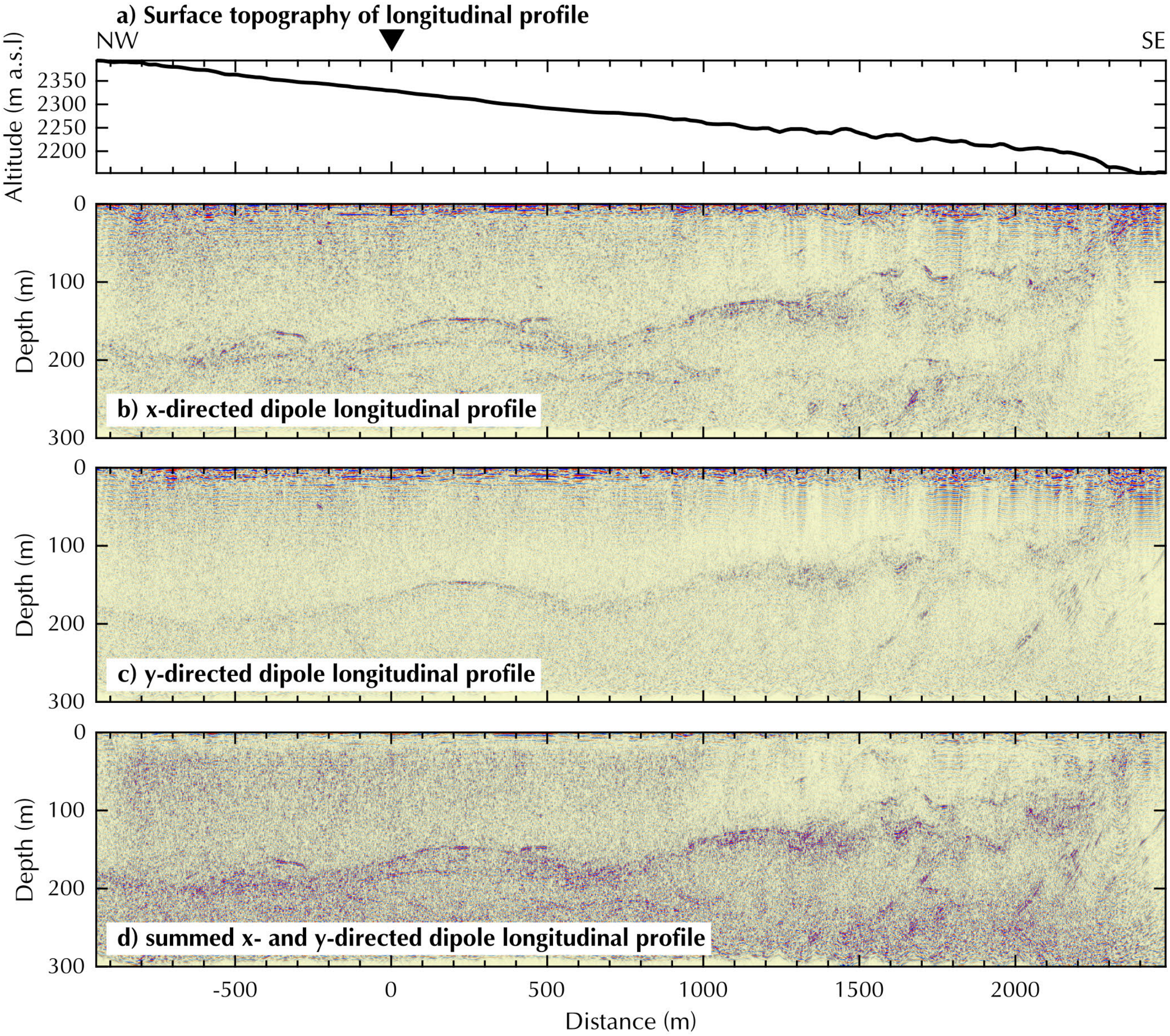

Figure 3.11: Processed longitudinal profile on Oberaletsch Glacier with (a) surface topography, (b) x-, (c) y- and (d) summed x- and y- directed dipoles. Y-axis exaggeration of profiles 3:1.

depends on the type of helicopter. As expected, smaller helicopters generate considerably less ringing, and conversations with transponders should be kept to a minimum to avoid interferences.

Another critical operational parameter is the helicopter speed. Since the dual-polarization system acquires the two data channels in an alternating mode, the acquisition time for a single position is approximately doubled compared to a single-polarization system. Additionally, because of the airborne acquisition and the depth of the glaciers, the data are recorded with a long time window of 4000 ns. To avoid spatial aliasing, the stacking rate has to be low and the helicopter speed should be kept to a maximum velocity of less than 30-40 km h^{-1}, which increases survey costs. Reducing the velocity can be achieved by flying against the wind direction and adapting the flight path trajectory during the survey relative to the surface gradient.

3.6 Conclusions and Outlook

Based on analytical calculations and numerical modeling, we conclude that the radiation pattern of GPR dipoles at low flight altitude ($<$ 40 m above the surface) do not correspond to a full space solution, because the far-field is reached inside the ice body. To overcome these directivity problems of a single pair of GPR antennas, we have developed a novel dual-polarization, helicopter-borne system (AIR-ETH). The benefits of acquiring dual-polarization data and applying the pseudo-scalar approach, in which both channels are summed, were demonstrated with two data sets of temperate Alpine glaciers. We observed that undulating subsurface topography causes varying bedrock amplitudes for both polarizations. Overall, after summing the data the bedrock reflections become more coherent, are visible at greater depth and in steep dipping regions.

The system is built with commercial components and can be reproduced. To maximize depth penetration, we have employed non-shielded 25 MHz antennas (the lowest frequency that can be currently used with our setup), but the system is versatile enough, such that higher frequency antennas could be operated for investigating shallow structures. Ringing effects from the helicopter can be a significant noise source. However, a proper shielding of the relatively large GPR antennas would require a sizeable shielding cover and would add extra weight. More research is required to investigate, if such an option for the AIR-ETH system is feasible. A potential extension of our dual-polarization concept could include true multi-component recording. Not only data recorded in broadside configuration, but additional orthogonal transmitter-receiver combinations could be considered. If desired, non-commercial two-channel real time acquisition systems and novel commercial high-power transmitters can be added to the existing setup. In principle, extending the system with vertical antennas would be possible and would provide a great range of opportunities. Advanced imaging algorithms could be employed to exploit the vectorial nature of GPR data (Lehmann et al., 2000; Streich and Van der Kruk, 2007). This could be particularly beneficial for detecting and handling off-plane reflections in helicopter-borne GPR surveys on plateau and valley glaciers.

3.7 Acknowledgments

Financial support was provided by ETH Zurich, the Swiss Geophysical Commission, and the Swiss Competence Center for Energy Research — Supply of Electricity (SCCER-SoE). Data acquisition has been enabled by the group of Exploration and Environmental Geophysics (EEG), the Laboratory of Hydraulics, Hydrology and Glaciology (VAW) of ETH Zurich and GEOSAT SA, Sion. The Oberaletsch Glacier campaign was funded by Alpiq Holding, Lausanne, Switzerland. We like to thank BRTechnik for building the frame, Christoph Bärlocher, Institute of Geophysics at ETH Zurich for technical support and we acknowledge G. Church for the help during the field campaigns. Processing of our data was facilitated by CREWES MATLAB software (Margrave, 2003). We thank S. H. Faria, H. Pritchard, an anonymous reviewer and E. King for constructive comments that improved the manuscript.

Chapter 4

Glacier thickness estimations and optimized survey design based on joint inversions of data and modeling constraints

Abstract

We have developed the GlaTE (Glacier Thickness Estimation) inversion algorithm to adequately invert for the three-dimensional ice thickness of Alpine glaciers based on physical modeling and observable data constraints. As an input, ground-penetrating radar (GPR) bedrock reflection measurements are used to constrain the absolute thickness while the gradients of a glaciological mass conservation model are integrated to force the overall thickness distribution. To account for parameter and data uncertainties, the constraints are formulated such that they can be merged into a single set of equation. The ice thickness of four distinct Swiss glaciers is calculated successfully and improved in comparison to traditional the mass conservation method. Afterwards, the GlaTE inversion is used to perform sequential optimized survey design for the GPR campaigns on the selected field sites. Only 21-46% of the originally acquired GPR profiles are needed to constrain the inversion to derive an ice thickness with less than a 2 m averaged absolute difference to the comprehensive GlaTE inversion result, which is calculated with the full set of GPR profiles. For narrow valley-shaped glaciers, longitudinal profiles are generally sufficient, while wider saddle and convergence zone should be surveyed with additional cross GPR profiles.

In preparation: Langhammer, L., Bauder, A., Grab, M.and H. Maurer.Glacier thickness estimations and optimized survey design based on joint inversions of data and modeling constraints.

4.1 Introduction

Estimating the amount of glacial ice mass around the globe is crucial for sea-level predictions, securing fresh water recourses and predicting the occurrence of natural hazards related to glaciated environments. To calculate the overall mass and its local distribution, surface and subsurface information of the glacier boundaries are required. While surface parameters, such as the outline and general slope of a glacier can be observed directly with aerial and satellite imagery, the subsurface topography is more difficult to determine. Due to the lack of appropriate subsurface data, glaciological methods have been established to relate surface parameters to the thickness distribution of ice. These methods can be categorized based on their approaches; minimization, mass conserving, shear-stress based or velocity-based (Farinotti et al., 2017).

Generally, the minimization approach utilizes inversion to infer ice thickness from observable surface data and regularization constraints. Starting from an initial model, a forward model is used to update the ice thickness estimates by reducing the difference between the modeled and observed data (e.g. Brinkerhoff et al., 2016; Morlighem et al., 2014).

Mass conserving approaches rely on the principle that ice flux divergence has to be compensated by the climate mass balance and the rate of ice thickness change, when ice is considered to be incompressible. By converting the mass flux, the ice thickness can be calculated (e.g Clarke et al., 2013; Farinotti et al., 2009b; Huss and Farinotti, 2012; Maussion et al., 2018; Morlighem et al., 2011). A detailed summary of this method can be found in Farinotti et al. (2017).

Shear-stress based approaches relate the distributed basal shear stress to the ice thickness (e.g Frey et al., 2014; Linsbauer et al., 2009, 2012) by assuming the shallow ice approximation (e.g Fowler and Larson, 1978). In contrast to the previous methods, the velocity-based approach considers either surface and basal ice flow velocities or depth-averaged profile velocities instead of the specific ice volume flux (e.g Gantayat et al., 2014).

As results of the extensive Ice Thickness Models Intercomparison eXperiment (ITMIX), Farinotti et al. (2017) highlights the wide span of ice thickness estimates calculated by the individual glacier models. None of the individual approaches proofed to be superior. The experiments shows that specific glacier models are capable of representing a selected range of glaciers quite well, but generally, observational data should be incorporated to increase the accuracy of the estimated ice thickness and observational uncertainties should be considered with care.

A widely used type of in-situ, ground-truth subsurface data from glaciers is recorded with ground-penetrating radar (GPR) techniques. By recording the echo of electromagnetic waves reflected from the ice-bedrock interface, ice thickness can be derived directly from GPR measurements (e.g. Nobes, 2014; Plewes and Hubbard, 2001; Watts and Wright, 1981). GPR techniques have the advantage of being logistically inexpensive, they can be operated ground-based and airborne. A full 3D GPR survey of a glacier system would likely provide the most accurate ice thickness distribution. However, spatially unaliased 3D coverage of large areas is impracticable with the current state of technology. Consequently, only a few sections along designated survey profiles are typically illuminated. Additionally, GPR data suffers from inconsistencies due to off-plane reflections (e.g Moran et al., 2000; Woodward and Burke, 2007), noise from other electromagnetic sources (e.g Kim et al., 2007; Rutishauser et al., 2016), GPR antenna orientation effects (e.g Langhammer et al., 2017), lack of penetration depth when water is present in the glacier (e.g Saetrang and Wold, 1986), and method-inherent uncertainties (Martín-Espanõl et al., 2016).

Neither the stand-alone glaciological models, nor the sole GPR data can provide reliable ice thickness estimates of entire glaciers, but by combining both approaches, a fairly realistic results can be achieved. In this work, we aim to establish the GlaTE (Glacier Thickness Estimation) inversion approach constrained by GPR ice thickness measurements, a glaciological mass conservation model to determine the general ice distribution and additional regularization. This requires a minimum amount of surface data (i.e. outline and surface topography) and in contrast to previous approaches, it accounts for observational and physical parameter uncertainties in the inversion process. As ground-true data, we utilize comprehensive helicopter-borne GPR measurements of the bedrock topography (Grab et al., 2018) and the glaciological model is adapted from Clarke et al. (2013).

First, the GlaTE inversion methodology is described and four glacier sites in the Swiss Alps with different shape and surface characteristics are presented as test sides. The results of the GlaTE inversion are compared to ice thickness estimates obtained from interpolated GPR profiles and the output of the glaciological mass conservation model. In a second step, the most relevant GPR profiles for the inversion, which are necessary to produce a detailed bedrock topography, are identified. To predict cost-efficient survey setups for GPR measurements, we make use of sequential optimized experimental design (OED) techniques (Maurer et al., 2010).

4.2 Glacier Thickness Estimation (GlaTE) inversion

The basic idea of the GlaTE inversions is to combine physical modeling constraints with observable data constraints, whereby it is attempted to consider appropriately the uncertainties associated with both of these constraints. They are formulated, such that they can be integrated into a single system of equations, which can be solved with an appropriate algorithm.

The first type of constraints includes the GPR data. They can be written in the form of

$$\boldsymbol{G}\boldsymbol{h}^{est} = \boldsymbol{h}^{GPR}, \tag{4.1}$$

where $\boldsymbol{G}$ is a $\mathrm{N}^{GPR} \times \mathrm{M}$ matrix with ones in its main diagonal and zeros everywhere else (N^{GPR} = the number of GPR data points, M = number of unknown ice thicknesses contained in h^{est}). $\boldsymbol{h}^{GPR}$ is a vector of length N^{GPR} including the GPR-based thickness estimates. Note that the unknown thicknesses $\boldsymbol{h}^{est}$ and the observed thicknesses $\boldsymbol{h}^{GPR}$ must have a common discretization and indexing. This may require to interpolate or extrapolate the original GPR data to the nearest location contained in $\boldsymbol{h}^{est}$.

Next, we consider glaciological modeling constraints. In principle, any of the algorithms proposed in the introduction can be employed. Here, we follow closely the approach described in Clarke et al. (2013). First, the area of interest is subdivided into different flowsheds using the MATLAB Topotoolbox (Schwanghart and Scherler, 2014), and the subsequent procedure is applied to every flowshed individually (see comments in Clarke et al. (2013) for more information on the flowshed subdivision). Within each flowshed, the equilibrium line altitude (ELA) is computed using prescribed mass balance gradients for the accumulation and ablation zone and a digital terrain model (DTM). With these information, the apparent balance rate (Farinotti et al., 2009b) and the ice flux is computed. This allows the basal shear stress τ

$$\tau = \left[\frac{(n+2)(\rho g\, sin\theta)^2 \xi q_\alpha}{2A}\right]^{1/(n+2)} \tag{4.2}$$

and finally the ice thicknesses $\boldsymbol{h}^{mod}$

$$h^{mod} = \frac{\tau}{\rho g\, sin\theta} \tag{4.3}$$

to be computed, where ρ is density, g the gravity acceleration, q the ice flux, ξ the relative creeping contribution of the ice flux, θ is the surface gradient obtained from the DTM, n is the exponent of Glen's flow law and A is the creep rate factor (Gudmundsson, 1999; Hubbard et al., 1998). In addition to the procedures, described in more detail in Clarke et al. (2013), we also apply longitudinal averaging as presented in Kamb and Echelmeyer (1986).

In principle, the glaciological constraints could be incorporated in an equivalent manner into the overall system of equations, as done with the GPR data constraints. However, there are considerable uncertainties in some of the quantities included in Equation 4.2. Therefore, the overall magnitudes of $\boldsymbol{h}^{mod}$ may be significantly over- or underestimated. In contrast, the relative spatial changes of $\boldsymbol{h}^{mod}$ are likely to be more reliable. Consequently, we include the spatial gradients of $\boldsymbol{h}^{mod}$ ($\nabla \boldsymbol{h}^{mod}$) into the corresponding system of equations yielding

$$\boldsymbol{L}\boldsymbol{h}^{est} = \nabla \boldsymbol{h}^{mod}, \tag{4.4}$$

where $\boldsymbol{L}$ is a difference operator of dimension $M \times M$. Further constraints can be imposed via the glacier boundaries that can be determined, for example, from satellite images or ground observations. They are considered in the form of

$$\boldsymbol{B}\boldsymbol{h}^{est} = 0, \tag{4.5}$$

where $\boldsymbol{B}$ is a $\mathrm{N}^{out} \times \mathrm{M}$ matrix (N^{out} number of grid points along the glacier boundaries or outside of glacierized areas) with ones in its main diagonal and zeros everywhere else. Depending on the discretization of the glacier models (i.e. the discretization of h), the constraints described above may allow the resulting system of equations to be solved unambiguously. In most cases there will be still a significant underdetermined component, which precludes a unique solution to be obtained (i.e., there will be many (infinite) solutions that explain the data equally well). This requires regularization constraints to be applied (e.g Menke and Eilon, 2015). A common strategy for regularizing such a problem is to follow Occam's principle, which identifies the "simplest" solution out of the many possible solutions (Constable et al., 1987). Here, we define "simplicity" in terms of structural complexity, that is, we seek a model with minimal structural complexity. This can be achieved via a set of smoothing equations of the form

$$\boldsymbol{S}\boldsymbol{h}^{est} = 0, \tag{4.6}$$

where $\boldsymbol{S}$ is a $M \times M$ smoothing matrix. All the constraints can now be merged into a single system of equations

$$\begin{pmatrix} \lambda_1 \boldsymbol{G} \\ \lambda_2 \boldsymbol{L} \\ \lambda_3 \boldsymbol{B} \\ \lambda_4 \boldsymbol{S} \end{pmatrix} \boldsymbol{h}^{\boldsymbol{est}} = \begin{pmatrix} \lambda_1 \boldsymbol{h}^{GPR} \\ \lambda_2 \boldsymbol{\nabla} \boldsymbol{h}^{mod} \\ \boldsymbol{0} \\ \boldsymbol{0} \end{pmatrix}. \tag{4.7}$$

With the parameters λ_1 to λ_4, the individual constraints can be weighted according to the confidence we have into the individual contributions. The first three sets of constraints have a physical basis, but the smoothing constraints in the fourth set are rather unphysical and are governed by Occam's principle. Therefore, one could be tempted to choose a small value for λ_4, which would make Equation 4.7 solvable. However, it needs to be considered that most of the other constraints are also not expected to provide accurate results. It is difficult to predict the accuracy of the modeling constraints, but the accuracy of the data constraints can typically be quantified. Therefore, λ_4 should be chosen such that $\|\boldsymbol{h}^{est} - \boldsymbol{h}^{GPR}\|^2 \approx \varepsilon^{GPR}$, where ε^{GPR} is the accuracy of the GPR data. If λ_4 is chosen to small, $\|\boldsymbol{h}^{est} - \boldsymbol{h}^{GPR}\|^2 < \varepsilon^{GPR}$, and if λ_4 is chosen too large, $\|\boldsymbol{h}^{est} - \boldsymbol{h}^{GPR}\|^2 > \varepsilon^{GPR}$. We employ a line search procedure for identifying a λ_4 value that satisfies $\|\boldsymbol{h}^{est} - \boldsymbol{h}^{GPR}\|^2 \approx \varepsilon^{GPR}$.

The dimension of this system of equations in 4.7 can be very large, but the matrices $\boldsymbol{G}$, $\boldsymbol{L}$, $\boldsymbol{B}$ and $\boldsymbol{S}$ are extremely sparse. Therefore, sparse matrix solvers, such as the LSQR algorithm (Paige and Saunders, 1982) can be employed for determining $\boldsymbol{h}^{est}$.

4.3 Field sites, data sets and GPR processing

For testing the GlaTE inversion, we investigate the glacier ice thickness at four field sites in the Swiss Alps (Figure 4.1).

The Vadret da Morteratsch (2050-4000 m a.s.l. in 2013, Zekollari et al., 2013), hereby referred to as Morteratsch Glacier (Figure 4.1a), has a typical valley-glacier shape and is located in the Bernina region of Switzerland. Its tributary glacier in the east is the Vadret Pers Glacier. In 2010, the glacier system covered an area of ∼15 km^2 and the Morteratsch Glacier had a length of ∼7.4 km (Bauder, 2015).

The Oberaletsch Glacier (2150-3900 m a.s.l., Figure 4.1b) is located in the Western Swiss Alps with an area of ∼17.5 km^2 in 2011 and a length of ∼9 km (Bauder, 2015). The Oberaletsch is supplied with glacier ice by its tributary glacier in the west, the Beich Glacier. The tongue is heavily debris-covered, because of the supra-glacial material originating from the headwalls in the North.

The Glacier de la Plaine Morte, referred to as Plaine Morte Glacier (2400-3000 m a.s.l., Figure 4.1c) is the largest plateau glacier in the European Alps (Bauder, 2017). The surface slope is shallow with less than 4° and a short glacier tongue exists in the North.

The fourth field site is a cluster of small valley- and cirque-type glaciers on the eastern mountain face of the Zermatt valley (Figure 4.1d) below the Dom peak. From North to South, the glaciers are named Hohbärg Glacier, Festig Glacier, Kin Glacier and Weingarten Glacier. The Hohbärg Glacier is the largest (2800-4500 m a.s.l., Swisstopo, 2018) and longest of the group. In the following, we will refer to this field site as the Dom region.

For all field sites in Figure 4.1, the recorded GPR profiles are shown in red. The GPR data set is a composite of several surveys campaigns. In 2011, the accumulation zone of the Oberaletsch Glacier was measured with the helicopter-borne BGR-P30 system (Rückamp and Blindow, 2012). More recent campaigns were carried out with the dual-polarization helicopter-borne AIR-ETH system (see Chapter 3) on the Plaine Morte Glacier in 2016 and 2017 and on the Morteratsch Glacier and in the Dom Region in 2017. Additionally, a dense grid of GPR profiles was collected in the tongue area of the Oberaletsch Glacier in 2017.

Generally, a longitudinal profile and several across profiles were collected as seen in the Morteratsch Glacier (Figure 4.1a) and in the Dom region (Figure 4.1d). However, we surveyed a regularly

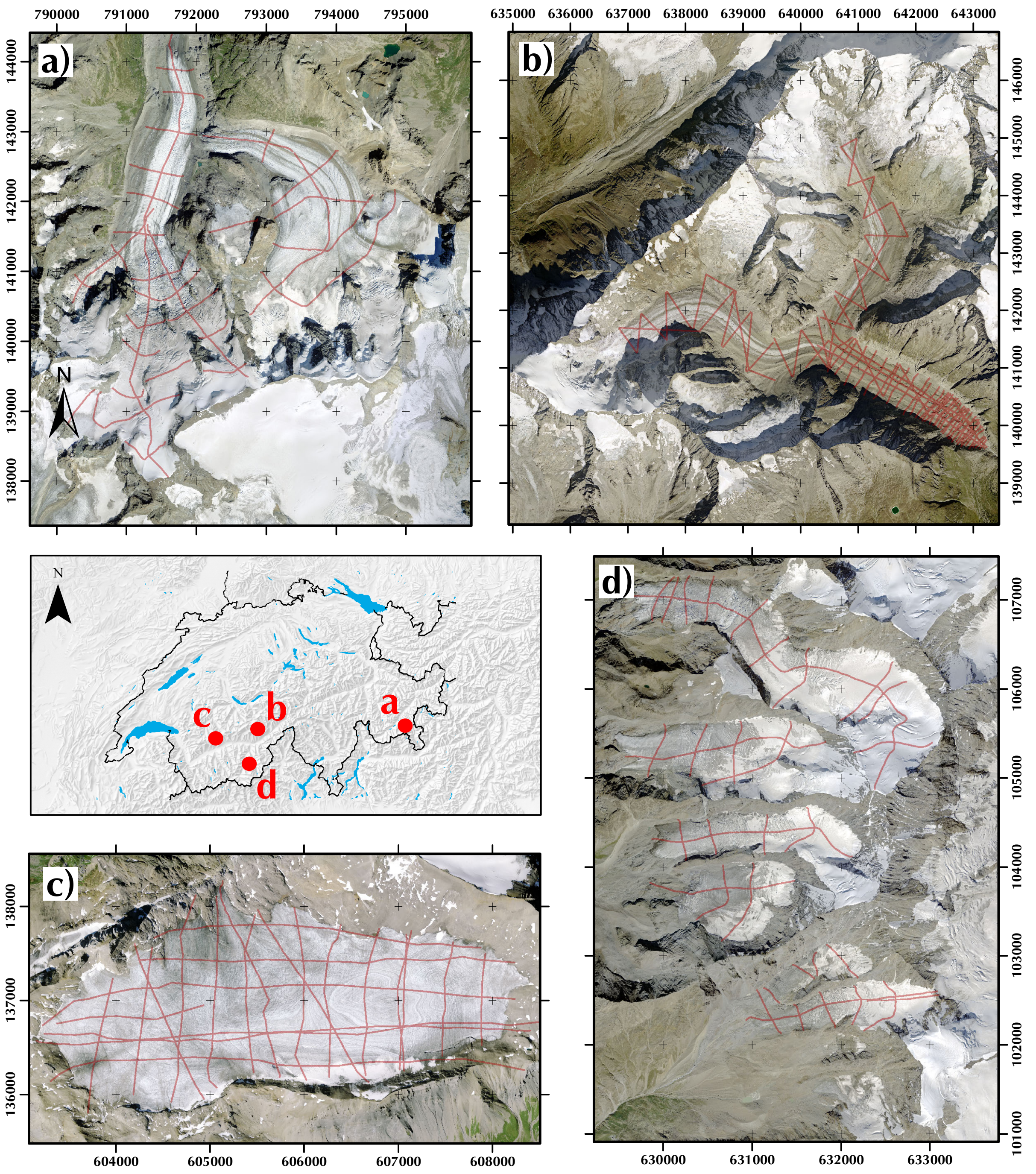

Figure 4.1: Map of the selected survey areas in Switzerland. Location indicated on overview map; middle-left. a) Morteratsch Glacier, b) Oberaletsch Glacier, c) Plaine Morte Glacier and d) the Dom region. Red lines correspond to helicopter-borne GPR profiles. Orthophotos © 2017 swisstopo (JD100042). Coordinate system: CH1903-LV03. Coordinate grid spacing = 1 km.

spaced grid on the Plaine Morte Glacier, because of its plateau shape. The areas at higher altitude of the Oberaletsch Glacier were measured with profiles angular to the flow direction.

All GPR data are processed with an in-house MATLAB-based software package, following partially standard GPR processing routines and other methods particularly adapted to our dual-polarization helicopter-borne GPR system setup. The processing flow consists of dewowing the raw data, data conversion to SEGY-format, removal of ringing noise, merging the dual-polarization channels, bandpass filtering, altitude correction, F-X deconvolution, reverse time migration and picking the bedrock reflection to determine the thickness of the glacier ice. A more detailed description of the processing procedures can be found in Grab et al. (2018) and in Chapter 3. We assume that the recorded reflections in the GPR data are in-plane. If several reflections from potential off-plane regions occur, we presume the stronger and more coherent one to be the primary reflection and therefore the bedrock.

The input data of the glaciological mass conservation model are surface topography and an outline of the individual glaciers. The outline is provided as a shapefile and was last updated in 2008. To work in our inversion scheme, it was converted into a glacier mask file in ASCII-format. We utilized the swissALTID3D (DTM, Digital Terrain Model © 2017 swisstopo (JD100042) as surface topography input. The DTM is generated based on a composite of elevation data points, which were measured in the last years. The most recent version from 2016 was downloaded, down-sampled to 10 m resolution and converted into the ASCII-format as well.

4.4 Performance of the GlaTE inversion

For all the computations with the data sets presented in Section 4.3, we employ the physical parameters summarized in Table 4.1. The weighting parameters λ_1, λ_2 and λ_3 are fixed to 2, 1 and 1, and, as described in Section 4.2, λ_4 are determined with a line search procedure, which typically converged within less than 20 iterations.

For evaluating the results of the GlaTE inversions ($\boldsymbol{h}^{est}$ in Equation 4.7, herein after referred to as comprehensive GlaTE output), we compare them to the ice thickness results (i) generated with interpolated GPR data only ($\boldsymbol{h}^{GPR}$ in Equation 4.1, areal information was obtained by linear inter- and extrapolation) and (ii) calculated with the glaciological mass conservation model ($\boldsymbol{h}^{mod}$ in Equation 4.4). While we were calculating the ice thickness with the glaciological model, we noticed that in some cases the absolute ice thickness deviated considerably from the interpolated GPR-derived thickness. The uncertainties of the glaciological model are summarized in Clarke et al. (2013) and their influence on the ice thickness of the glaciological model output were estimated to be 10 %. This can be attributed to the uncertainties of some of the constants in Table 4.1. The uncertainties are less problematic for the GlaTE inversion, since only the spatial gradients of the

Table 4.1: Physical constants and glaciological parameters for the glaciological mass conservation model, (Clarke et al., 2013; Farinotti et al., 2009b; Gudmundsson, 1999; Hubbard et al., 1998; Kamb and Echelmeyer, 1986). acc. = accumulation, abl. = ablation

Constants and parameters	
Considered surface slope angle θ	1.5° - 60°
Elevation gradient of mass balance rate in acc. zone $d\dot{b}^{+}/dz$	0.005
Elevation gradient of mass balance rate in abl. zone $d\dot{b}^{-}/dz$	0.009
Number of balance zones in flowshed n_b	10
Fraction of ice creep in ice flux ξ	1
Longitudinal coupling length l	2
Glen's flow law exponent n	3
Creep factor constant A	2.4×10^{-15} Pa^{-3} s^{-1}
Ice density ρ	910 kg m^{-3}
Gravity acceleration g	9.81 m s^{-2}

thickness distributions are considered. However, for the comparisons of the models, we scaled and adjusted the glaciological mass conservation model results, such that $mean(\boldsymbol{h}^{GPR}) \approx mean(\boldsymbol{h}^{mod})$. Only the location where GPR data are available, were considered for computing the mean values.

A detailed analysis of the GPR measurements on an Alpine Glacier with the same center frequency as we used for the helicopter-borne GPR surveys in this study can be found in Feiger et al. (2018). Based on their results, the error for the GPR measurements is estimated to be in a range of ±5 m.

The calculated comprehensive GlaTE ice thickness ($\boldsymbol{h}^{est}$) is shown in Figures 4.2c-4.5c. Additionally to the GlaTE inversion results, the figures display the adjusted output of the glaciological model ($\boldsymbol{h}^{mod}$) and the interpolated thickness of the scattered GPR profiles ($\boldsymbol{h}^{GPR}$). The locations of the GPR measurements are indicated with semi-translucent black lines in Figures 4.2b-4.5b.

The comprehensive results for all four field sites calculated with the GlaTE inversion, display an elaborate composite of the constraints applied in the inversion. The maximum thickness of the Morteratsch (Figure 4.2c) and Oberaletsch Glacier (Figure 4.3c) reaches ∼250 m, for the Plaine Morte Glacier ∼200 m (Figure 4.4c) and the deepest areas in the Dom region (∼150 m) can be observed on the Hohbärg Glacier in the North (Figure 4.5c). However, localized discrepancies are visible in the thickness distribution of the comprehensive GlaTE output.. For example, the end of Morteratsch glacier tongue is shallower than calculated with the glaciological model and a gap of zero thickness can be seen in the comprehensive GlaTE output. Similar, the section of

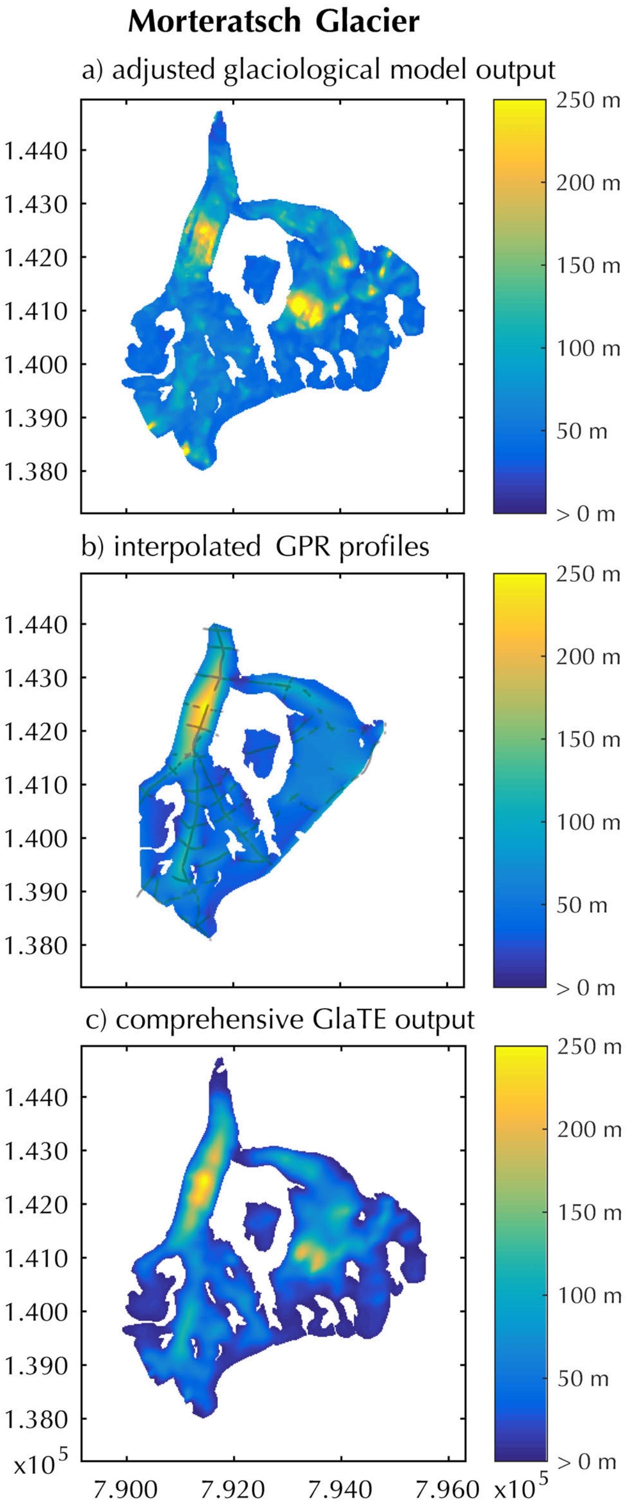

Figure 4.2: Glacier thickness for the Morteratsch Glacier calculated with a) the glaciological model ($\boldsymbol{h}^{mod}$), b) interpolated GPR profiles ($\boldsymbol{h}^{GPR}$) with tracks superimposed semi-transparent in black and c) the GlaTE inversion ($\boldsymbol{h}^{est}$). Only GPR data points with visible bedrock reflection are displayed in (b).

the accumulation zone of the third northern glacier in the Dom region (approximately at 632000, 104000, Figure 4.5c) is detached from the glacier body.

Overall, the ice thickness derived with the glaciological model (Figures 4.2a-4.5a) is more heterogeneous than the thickness interpolated from the GPR profiles and localized maxima appear. These can be observed in the accumulation zone of the Morteratsch (Figure 4.2a) and Oberaletsch Glacier (Figure 4.3a). Specifically in the northernmost glacier in the Dom region (Figure 4.5a), the strongly irregular thickness distribution along the flow line becomes apparent. The position of the thickest sections and their absolute thickness agree generally well with the measured and interpolated GPR thickness, however, in case of the Oberaletsch Glacier a strong disagreement in maximum thickness is visible in the western tributary glacier.

Due to the limited coverage of the GPR profiles, only selected areas restricted by the glacier outline can be interpolated. This is demonstrated in the branched accumulation zones of the Morteratsch (Figure 4.2b) and Oberaletsch Glacier (Figure 4.3b) in the interpolated GPR results. No GPR data were available for these regions. In contrast to the glaciological model output, the GPR-derived thickness distribution is smoother and exhibits elongated thicker zones along the flow lines and in the glacier tongue zone . In case of the Oberaletsch, Figure 4.3b displays the expected thickening in the convergence zone where both glacier arms join. A particularly good agreement of the ice thickness for all three model outputs can be observed for the Plaine Morte glacier. The GPR profiles cover the glacier area sufficiently and the location of shallower and thicker regions is similar.

By comparing the outcome of all three methods, it becomes apparent that regions without available GPR measurement are shallower in the comprehensive GlaTE output compared to the results of the glaciological model. In the accumulation zone of the western Oberaletsch Glacier branch (637000, 141500, Figure 4.3c) a sharp change in ice thickness can be seen between the area where GPR data was available to constrain the GlaTE inversion and the zone solely inferred from the other constraints. For all four field sites, the comprehensive GlaTE output transitions smoother towards zero at the edges of the glacier. Additionally, it can be observed that the ice thickness in the tongue area of the Oberaletsch and the Morteratsch Glacier resembles an expected valley-type shape in contrast to the glaciological model results. The glacier tongue is thicker in the middle closest to the stream line and shallower closer to the glacier border.

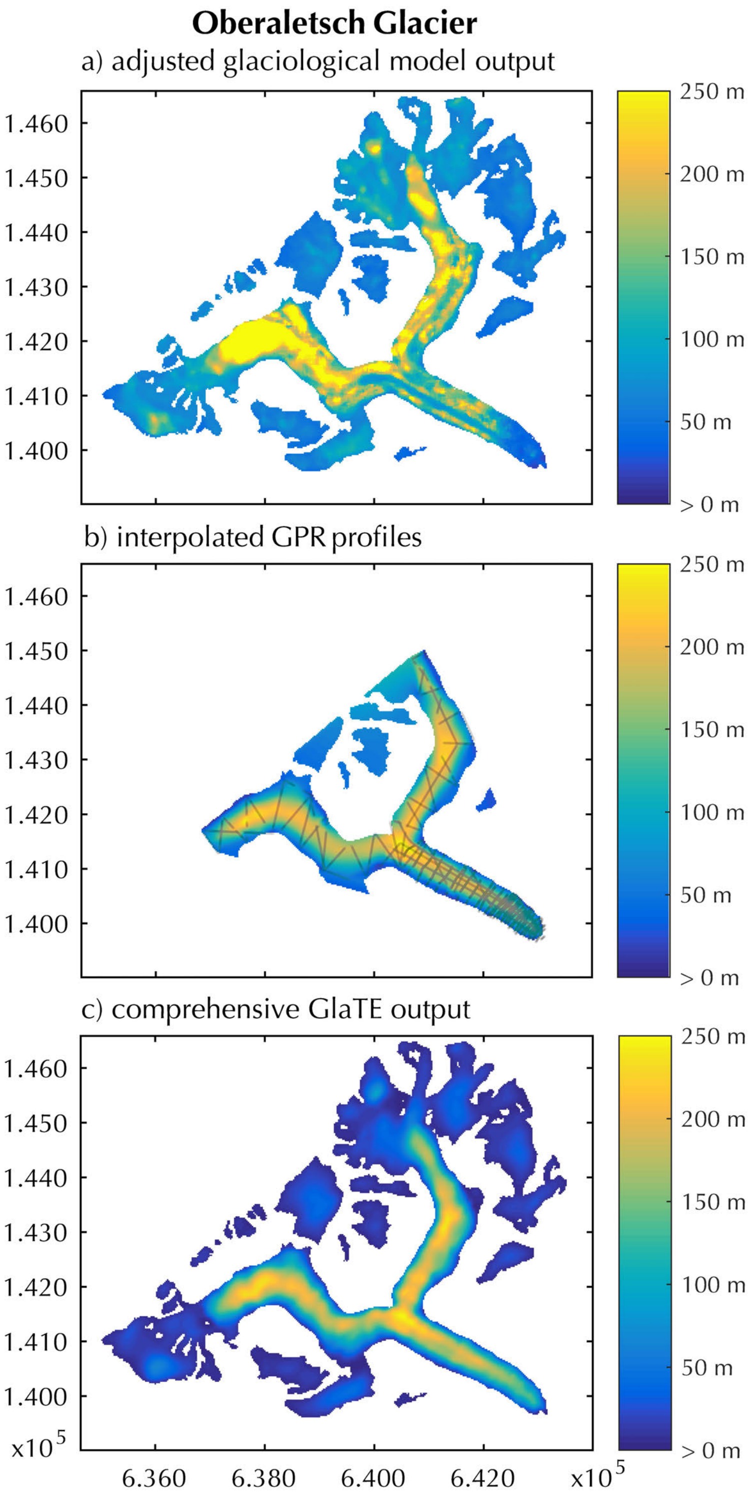

Figure 4.3: Glacier thickness for the Oberaletsch Glacier calculated with a) the glaciological model ($\boldsymbol{h}^{mod}$), b) interpolated GPR profiles ($\boldsymbol{h}^{GPR}$) with tracks superimposed semi-transparent in black and c) the GlaTE inversion ($\boldsymbol{h}^{est}$). Only GPR data points with visible bedrock reflection are displayed in (b).

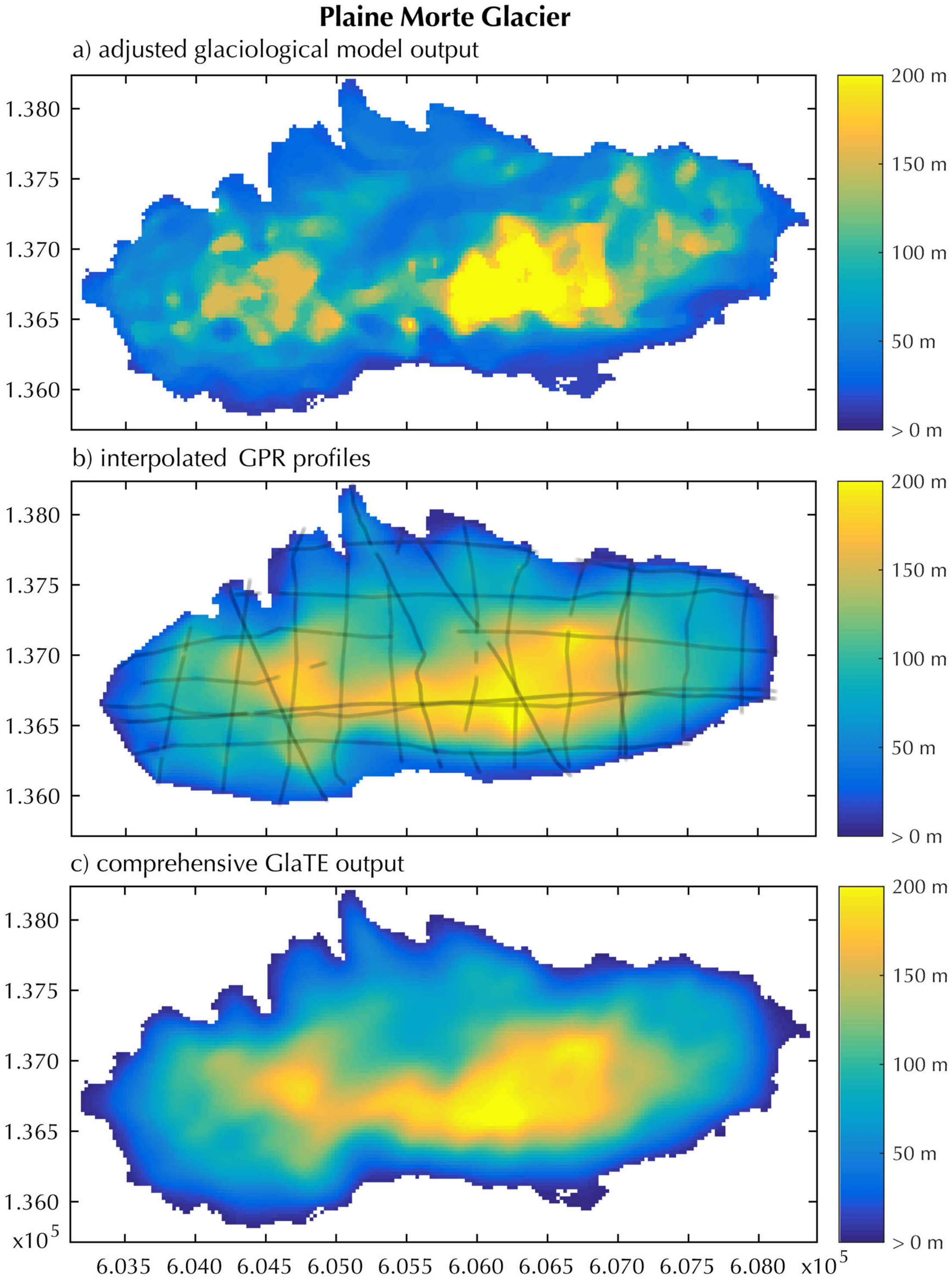

Figure 4.4: Glacier thickness for the Plaine Morte Glacier calculated with a) the glaciological model ($\boldsymbol{h}^{mod}$), b) interpolated GPR profiles ($\boldsymbol{h}^{GPR}$) with tracks superimposed semi-transparent in black and c) the GlaTE inversion ($\boldsymbol{h}^{est}$). Only GPR data points with visible bedrock reflection are displayed in (b).

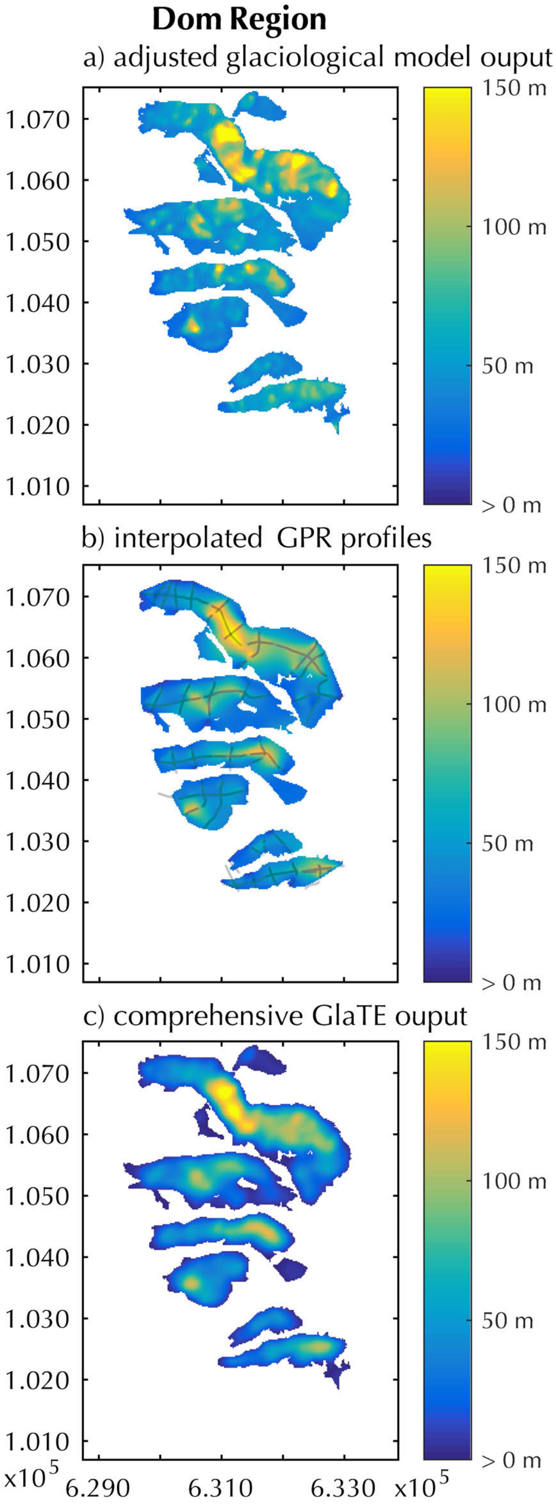

Figure 4.5: Glacier thickness for the Dom region calculated with a) the glaciological model ($\boldsymbol{h}^{mod}$), b) interpolated GPR profiles ($\boldsymbol{h}^{GPR}$) with tracks superimposed semi-transparent in black and c) the GlaTE inversion ($\boldsymbol{h}^{est}$). Only GPR data points with visible bedrock reflection are displayed in (b).

4.5 Sequential optimized experimental survey design

As shown in the results of Section 4.4, the GlaTE inversion algorithm is capable of inverting for the glacier thickness of the selected field sites. On the one hand, the advantage of the inversion is that it incorporates GPR measurements and the subsurface image is becoming more detailed the more GPR data is available. On the other hand, the benefit of the geophysical survey is likely to stagnate with an increasing amount of measurements because subsurface information become redundant. GPR surveys on glaciers are generally time- and cost-consuming so that an optimized survey design can increase the benefit-cost ratio of field campaigns significantly.

By applying optimized experimental design (OED) (e.g Maurer et al., 2010), we can seek for an optimized layout of GPR profiles to minimize cost and maximize the desired information about the subsurface. In the particular case of GPR thickness surveys on Alpine glacier, we aim to infer which potential GPR profiles contain most of the relevant thickness information. An approach for solving the optimization problem is sequential OED. A specific subset of the data can be removed consecutively (Curtis et al., 2004) from a comprehensive data set ($\boldsymbol{h}^{comp}$) so that the difference between the information in the remaining data set and the information in the comprehensive data set is minimized. In another approach, an initial model with few a priori information is updated progressively with new information until redundancies and a saturation of the information content occurs (Stummer et al., 2004). In our study, we will apply the latter method to identify an optimal GPR survey layout. The subsets $\boldsymbol{h}_j^{GPR}$ are GPR profiles taken from the complete GPR data set ($\boldsymbol{h}^{GPR}$) used in Equation 4.1 with j being the number of iterations. Further information about the concept of sequential optimized experimental design (SOED) can be found in Maurer et al. (2010) and Maurer et al. (2017).

We consider the cost to be linear with collected profile kilometers and exclude transition time in between profiles. Additionally, we assume that in each GPR profile the bedrock reflections are visible for all measurement points and therefore, thickness data exists for the entire profile. In the previous section 4.4, all GPR profiles are considered to generate the comprehensive GlaTE inversion output ($\boldsymbol{h}^{comp}$). It is equal to h_N^{est} with N being the total number of available GPR profiles. $\boldsymbol{h}^{comp}$ will be used as a benchmark to validate the information content in the current output ($\boldsymbol{h}_j^{est}$) of the GlaTE inversion calculated with a subset of GPR profiles ($\boldsymbol{h}_j^{GPR}$). In each iteration j = 1,2,...,N, when a profile is added to the GPR data subset, the optimized profile layout has to be selected. The layout consists of a number of previously, subsequently added GPR profiles, which are, once selected, not available for the next iteration anymore. In the process of selecting the desired profiles, all possible profile combinations are calculated and per iteration one optimal set of combinations is chosen.

To solve for the optimized survey layout, we are applying three SOED approaches with the following properties:

1. SOED$_{comp}$: finding k such that $min < |\boldsymbol{h}^{comp} - \boldsymbol{h}_j^{est}| >$
2. SOED$_{prev}$: finding k such that $max < |\boldsymbol{h}_j^{est} - \boldsymbol{h}_{j-1}^{est}| >$
3. SOED$_{weight\times comp}$: finding k such that $min\ (\alpha < |\boldsymbol{h}^{comp} - \boldsymbol{h}_j^{est}| >)$; α = length of the selected GPR profile

k corresponds to the index of the added GPR profile. The averaged ice thickness is defined as $< \boldsymbol{h} >= \frac{1}{M}\sum_{m=1}^{M} h_m$ with m defined as the cells inside the glacier outline. The initial ice thickness output of the GlaTE inversion without added GPR data corresponds to the results of the glaciological mass conservation model ($\boldsymbol{h}^{mod}$).

In SOED$_{comp}$, we are solving for an individual profile k to add to $\boldsymbol{h}_{j-1}^{GPR}$, the GPR data of our previous output of the GlaTE inversion $\boldsymbol{h}_{j-1}^{est}$ so that the averaged absolute difference between the comprehensive GlaTE output $\boldsymbol{h}^{comp}$ and current output $\boldsymbol{h}_j^{est}$ is minimized. By following this strategy, the profiles with the most desirable information content are added.

For SOED$_{prev}$ the profile k is chosen so that the averaged absolute difference between the previous GlaTE output $\boldsymbol{h}_{j-1}^{est}$ and current output $\boldsymbol{h}_j^{est}$ is maximized. This case is the most adequate analogy to an actual survey situation in the field, when GPR profiles are added during the surveying on the glacier to improve the spatial resolution and maximize the information content.

The last approach SOED$_{weight\times comp}$, minimizes the averaged absolute difference as in SOED$_{comp}$ with additionally applying a weighting factor α depending on the length of the added profile. This approach will allow us to test the hypothesis, if shorter profiles (e.g. across profiles) are sufficient and if they should be preferred over longer profiles. By adding the weighting factor, long profiles are penalized.

The decrease of the averaged absolute thickness difference $< |\Delta \boldsymbol{h}| >$ per cumulative profile length for the individual approaches is shown in Figure 4.6. Each marker represents a profile that was added to the profile layout to fulfill the SOED$_{comp}$, SOED$_{prev}$ or SOED$_{weight\times comp}$ requirements. We defined the target difference to be equal to 2 m, which corresponds to the threshold when a GPR profile ensemble is sufficient enough to reproduce the subsurface topography. The total GPR profile length for the Morteratsch Glacier is ~39.5 km, the Oberaletsch Glacier ~64.2 km, the Plaine Morte Glacier ~55.5 km and ~31 km of profile lines were measured in the Dom region. It can be observed that for all three SOED cases, as expected, the averaged absolute difference decreases with added GPR profiles. The target difference is reached after summing 34% of the total GPR profiles length on the Morteratsch Glacier (SOED$_{prev}$), 21% on the Oberaletsch Glacier (SOED$_{comp}$), 46% on the Plaine Morte Glacier (SOED$_{comp}$) and after 30% in the Dom

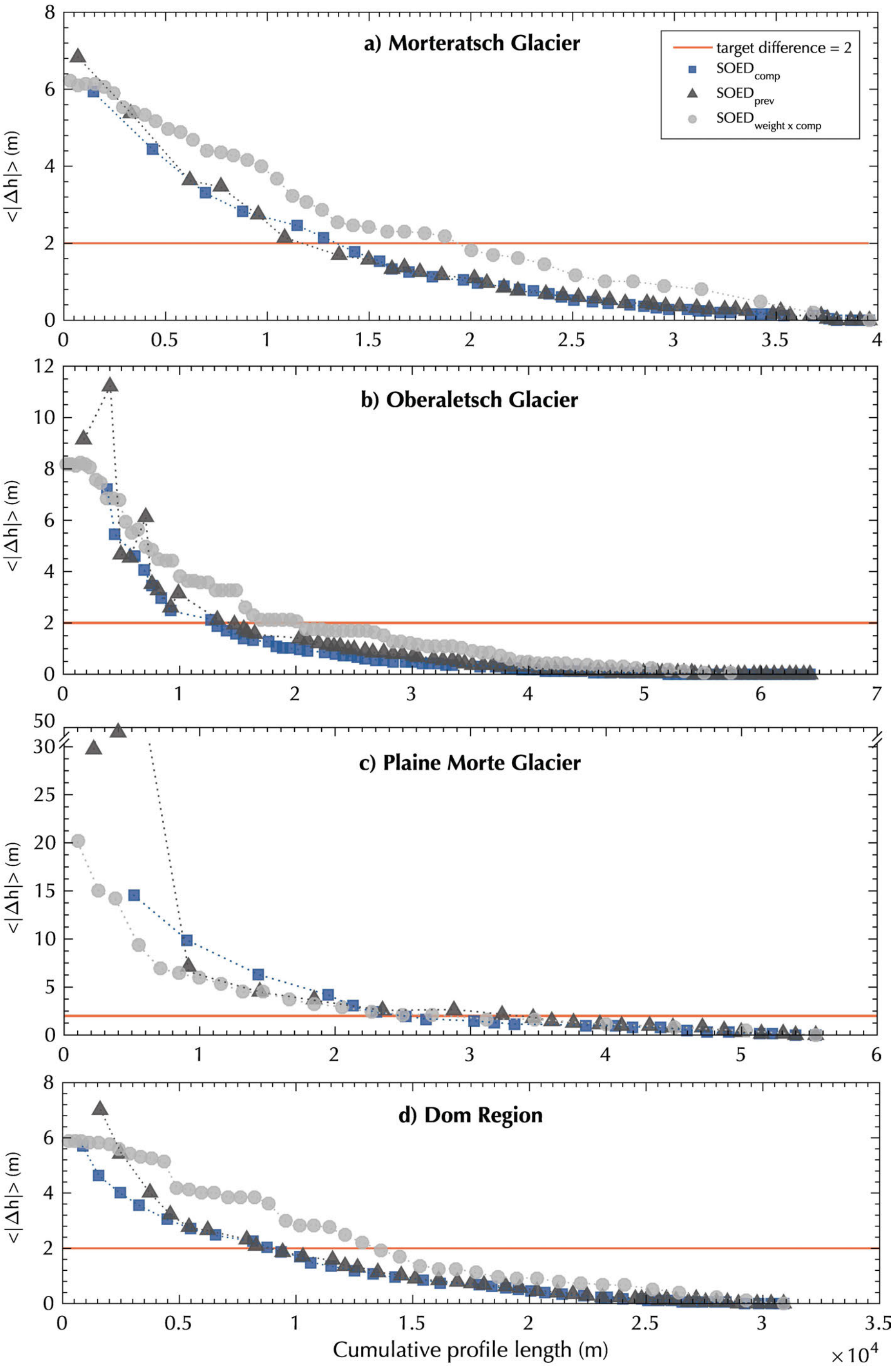

Figure 4.6: Averaged absolute ice thickness difference $<|\Delta \boldsymbol{h}|>$ between comprehensive GlaTE output ($\boldsymbol{h}^{comp}$) and the current GlaTE ice thickness ($\boldsymbol{h}_j^{est}$) per cumulative profile length of the GPR profiles. Individual GPR profiles (markers) are added consecutively depending on sequential optimized experimental design case. a) Morteratsch Glacier, b) Oberaletsch Glacier, c) Plaine Morte Glacier, d) Dom region. Target ice thickness difference is indicated as red line. X- and y-axis range differ for each panel and in (c) the y-axis is clipped.

region (SOED$_{comp}$). The solution of the SOED$_{comp}$ and SOED$_{prev}$ are very similar, while the trend of SOED$_{weight \times comp}$ approach deviates stronger. In contrast to the valley-type glaciers in our test sites, for the Plaine Morte Glacier almost half of the survey grid is necessary to reach the target difference. With its particular plateau shape, more area has to be surveyed to cover its extent. As shown in Figure 4.6, preferring shorter profiles as done in the SOED$_{weight \times comp}$ case does not yield a benefit over the other methods, but rather hinders the optimized experimental survey design.

Based on the previous results, we conclude that the SOED$_{comp}$ approach is sufficient in deriving the optimized experimental survey layout for GPR surveys. For the following analysis, we will consider the existing, field-based GPR profiles of the selected field sites as shown in Figure 4.1. We define the GPR profile layout to be optimal when the target thickness difference in Figure 4.6 is reached. Additionally, we calculated the optimized output $\boldsymbol{h}^{est}_{j_{opt}}$, which corresponds to the ice thickness results calculated with GlaTE inversion and the optimized survey layout. Finally the optimized output is compared to the comprehensive GlaTE output. The results are displayed in Figure 4.7-4.10 with the GPR profiles of the optimized layout numbered in order of selection. In the background of Figure 4.7a-4.10a the ice thickness difference $\Delta \boldsymbol{h}^{opt} = \boldsymbol{h}^{comp} - \boldsymbol{h}^{est}_{j_{opt}}$ is shown to identify which regions in the optimized GlaTE output deviate from the comprehensive one. Likewise, the background in Figure 4.7b-4.10b presents the initial ice thickness difference $\Delta \boldsymbol{h}^{mod} = \boldsymbol{h}^{comp} - \boldsymbol{h}^{mod}$ of the comprehensive GlaTE output and the results of the glaciological model.

For all four field sites, it can be observed that the ice thickness difference $\Delta \boldsymbol{h}^{opt}$ (Figure 4.7a-4.10a) for the optimized case significantly decreases compared to $\Delta \boldsymbol{h}^{mod}$ in Figure 4.7b-4.10b. The sparser, evenly-spaced survey grid on the Plaine Morte Glacier (Figure 4.9a) creates a sufficient coverage of the glacier which results in minimal discrepancies between the comprehensive and optimized GlaTE outputs. Large differences in ice thickness between the comprehensive GlaTE results and the glaciological mass conservation model in Figure 4.9b are strongly decreased with the optimized GlaTE output (Figure 4.9a). The first four selected tracks on the Plaine Morte Glacier are the long cross profiles from East to West with the shorter longitudinal profiles picked later. In contrast, especially longitudinal profiles are selected on the Morteratsch Glacier (Figure 4.7a). The same observation can be made for the Oberaletsch glacier (Figure 4.8a). Longitudinal profiles are also preferably selected in the glacier tongue area of the Oberaletsch Glacier instead of the dense grid of across profiles shown in Figure 4.1b. Compared to the initial ice thickness difference ($\Delta \boldsymbol{h}^{mod}$) on the Oberaletsch Glacier (Figure 4.8b), the optimized GlaTE output reproduces the ice thickness in the accumulation zone well ($\Delta \boldsymbol{h}^{opt}$). Stronger differences can be seen in the eastern branch of the glacier, where only zig-zag profiles are available. In the Dom region (Figure 4.10a), the SOED$_{comp}$ results are similar to the other valley-type glaciers. Due to the existence of several

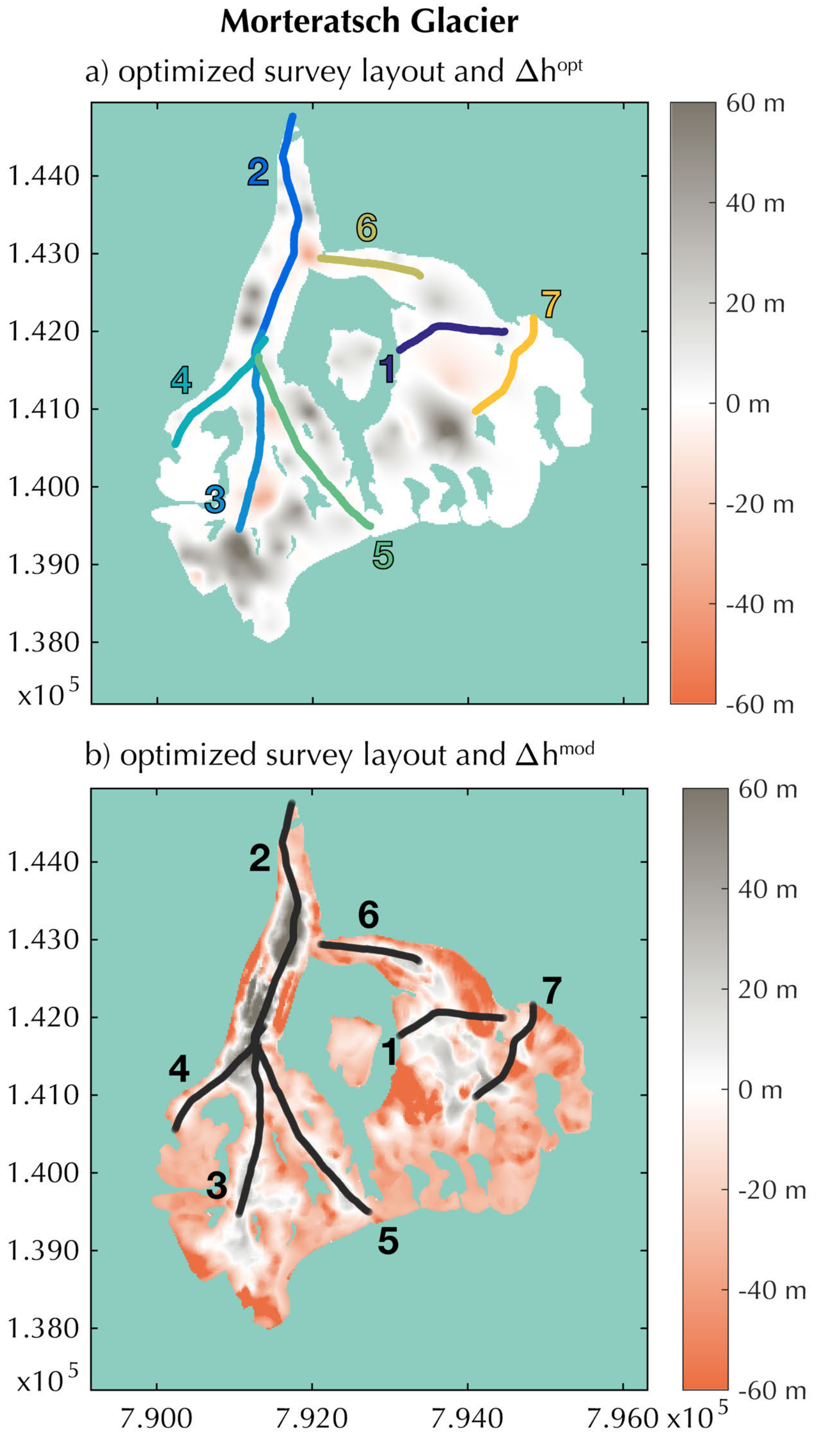

Figure 4.7: Optimized GPR survey layout for the Morteratsch Glacier achieved with SOED$_{comp}$ when target difference is reached in Figure 4.6. GPR profiles (colored in (a) and black in (b)) are numbered in order of selection. Background in (a) is the ice thickness difference $\Delta\boldsymbol{h}^{opt}$ between the comprehensive $\boldsymbol{h}^{comp}$ and the optimized GlaTE output $\boldsymbol{h}^{est}_{j_{opt}}$. Ice thickness difference $\Delta\boldsymbol{h}^{mod}$ between the comprehensive GlaTE results $\boldsymbol{h}^{comp}$ and the glaciological model $\boldsymbol{h}^{mod}$ is displayed in (b).

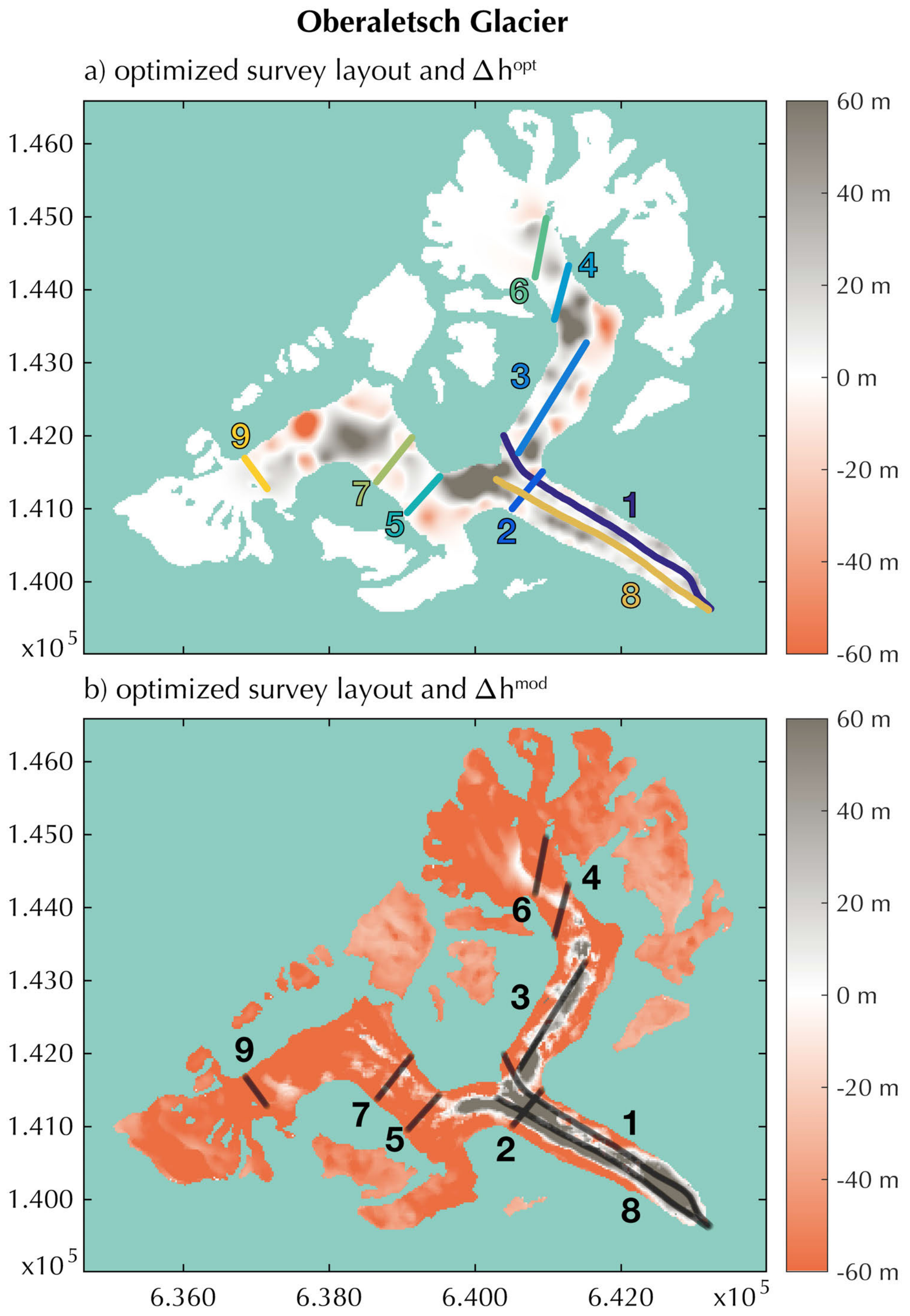

Figure 4.8: Optimized GPR survey layout for the Oberaletsch Glacier achieved with SOED$_{comp}$ when target difference is reached in Figure 4.6. GPR profiles (colored in (a) and black in (b)) are numbered in order of selection. Background in (a) is the ice thickness difference $\Delta\boldsymbol{h}^{opt}$ between the comprehensive $\boldsymbol{h}^{comp}$ and the optimized GlaTE output $\boldsymbol{h}^{est}_{j_{opt}}$. Ice thickness difference $\Delta\boldsymbol{h}^{mod}$ between the comprehensive GlaTE results $\boldsymbol{h}^{comp}$ and the glaciological model $\boldsymbol{h}^{mod}$ is displayed in (b).

smaller glaciers in the region, the GPR profiles are not distributed evenly but rather localized on the glaciers further in the North and the ice thickness differences are greater in the South. Overall, the results inverted with the optimized GPR survey layout showed that the subsurface topography can be approximated very well with a reduced amount of profiles.

4.6 Discussion

The ice thickness results obtained from the GlaTE inversion for all four glacier sites (Figures 4.2-4.5) demonstrate that a glaciological model and GPR thickness data, merged by inversion, outperform the sole application of either of them. The advantage of the GlaTE inversion is that inherent uncertainties of the glaciological model can be balanced by allowing for a thickness discrepancy of the order of the data accuracy. Improving the certainty of glaciological parameters, such as the relationship between the creep and sliding fraction, would enhance the comprehensive GlaTE output further. Morlighem et al. (2011), Morlighem et al. (2014) and Brinkerhoff et al. (2016) investigated the propagation of errors and uncertainties for their mass conservation inversion scheme. On large outlet glacier of the Greenland Ice Sheet the uncertainties increase to 10 % of the ice thickness at large distances from ground-truth measurements, but for the valley-type glacier Storglaciären in Sweden (Brinkerhoff et al., 2016) the uncertainties increases even further due to lack of abundance of GPR data. Morlighem et al. (2014) compared their results with the widely used kriging method (e.g Deutsch and Journel, 1992; Bamber et al., 2013) and concluded that inversion algorithms constrained by ground-truth thickness data are superior to kriging in regions with low data coverage, but for highly covered areas, kriging performs similarly well. The inversion approaches of Morlighem et al. (2014) and Brinkerhoff et al. (2016) differ from the GlaTE inversion since they utilize surface flow velocities, but a detailed analysis of the propagation of uncertainties would facilitate our newly developed approach. In the further development of the GlaTE inversion algorithm, benchmarking our approach against existing methods (Farinotti et al., 2017) or previously published ice thickness results the selected field sites (e.g. Zekollari et al., 2013) can be expected. Generally, the advantage of the GlaTE inversion over traditional glacier models is its extendability with additional data (e.g. surface velocities). This makes it possible to add extra constraints such as surface displacement into the inversion.

Even though a thickness range can be estimated by setting the bounds to the potential upper and lower reflections (Feiger et al., 2018), the inherent uncertainties in GPR data can lower accuracy of the results (Lapazaran et al., 2016). Additionally, bedrock reflections are not necessarily visible in all of the acquired profiles. Off-plane reflections are special features in the radargram and differ from the general uncertainties of GPR measurements. It is beyond the scope of this study to answer the question, if off-plane reflections in the radargram interfere with the desired in-plane

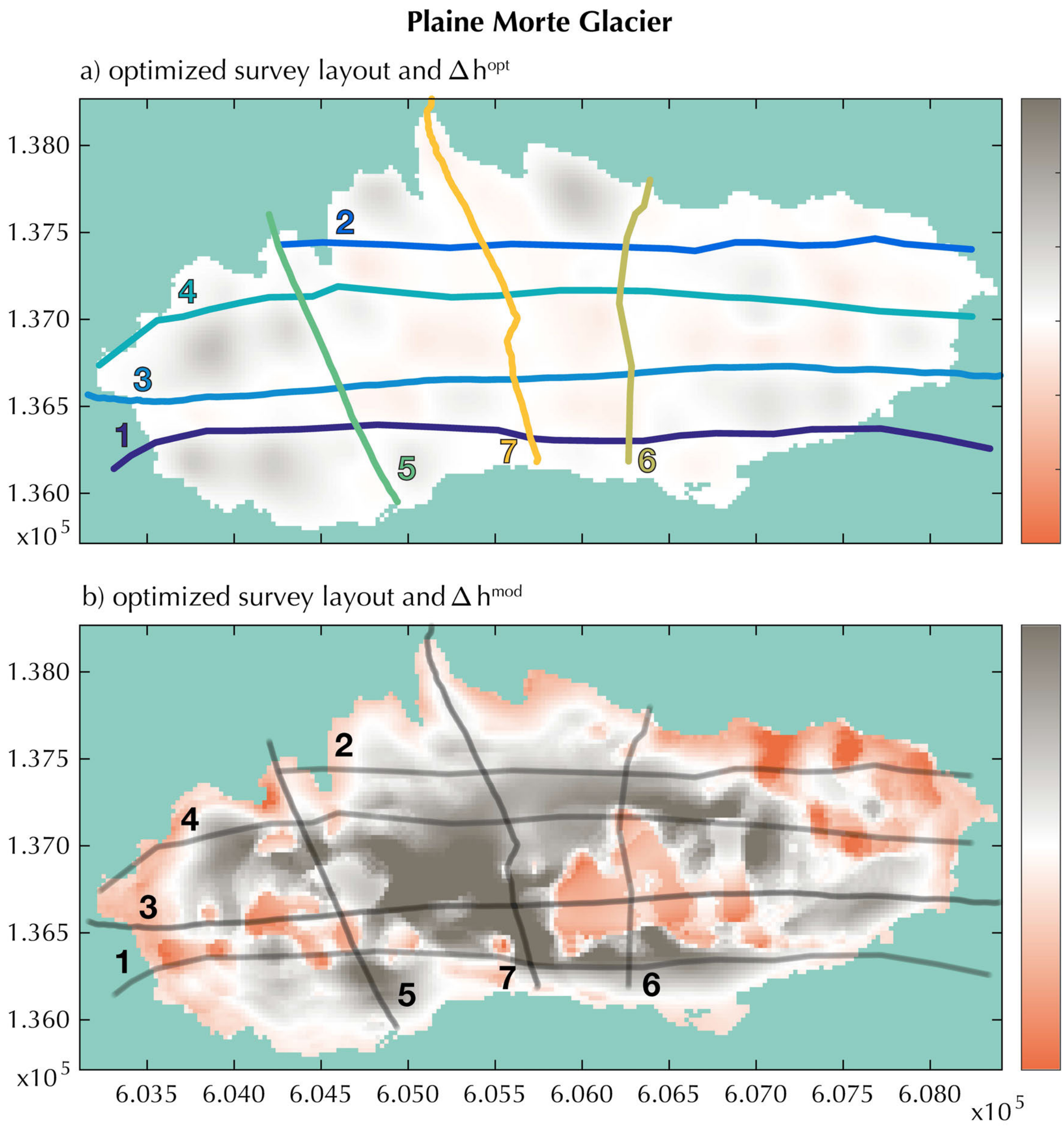

Figure 4.9: Optimized GPR survey layout for the Plaine Morte Glacier achieved with SOED$_{comp}$ when target difference is reached in Figure 4.6. GPR profiles (colored in (a) and black in (b)) are numbered in order of selection. Background in (a) is the ice thickness difference $\Delta\boldsymbol{h}^{opt}$ between the comprehensive $\boldsymbol{h}^{comp}$ and the optimized GlaTE output $\boldsymbol{h}^{est}_{j_{opt}}$. Ice thickness difference $\Delta\boldsymbol{h}^{mod}$ between the comprehensive GlaTE results $\boldsymbol{h}^{comp}$ and the glaciological model $\boldsymbol{h}^{mod}$ is displayed in (b).

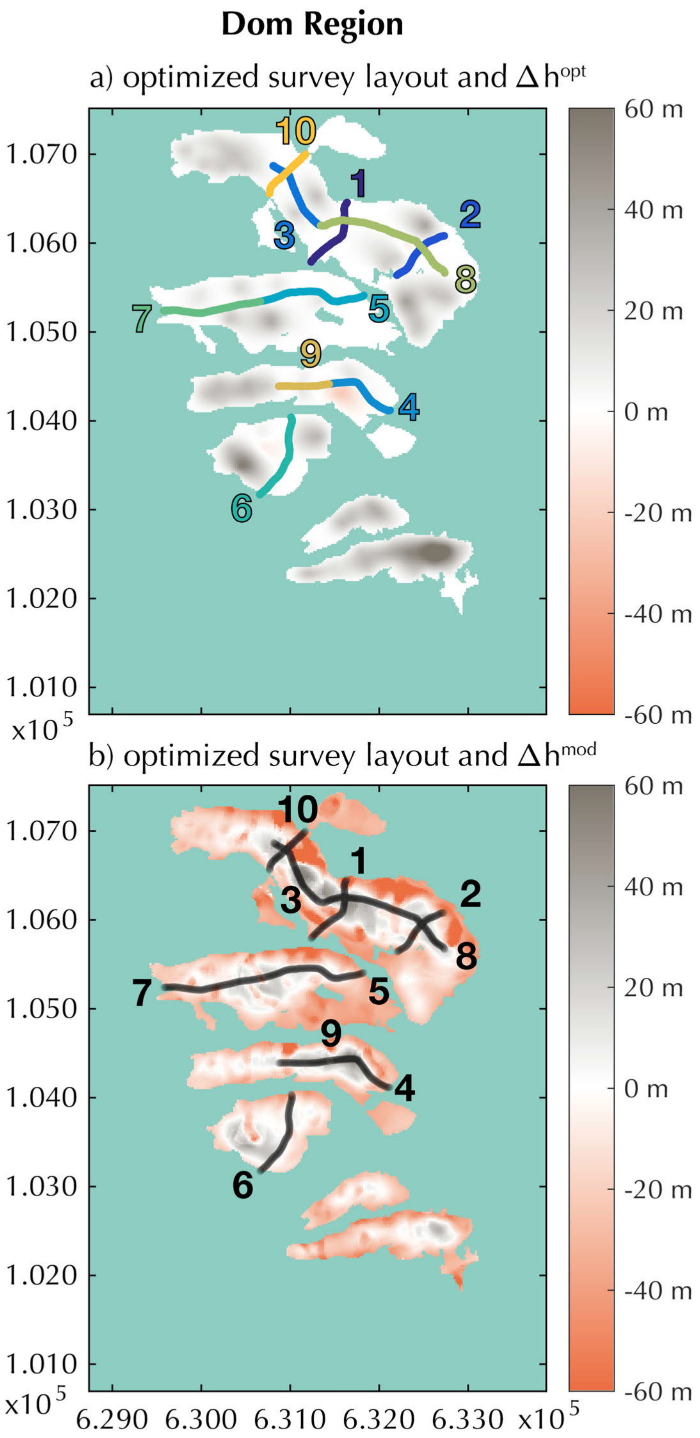

Figure 4.10: Optimized GPR survey layout for the Dom region achieved with SOED$_{comp}$ when target difference is reached in Figure 4.6. GPR profiles (colored in (a) and black in (b)) are numbered in order of selection. Background in (a) is the ice thickness difference $\Delta \boldsymbol{h}^{opt}$ between the comprehensive $\boldsymbol{h}^{comp}$ and the optimized GlaTE output $\boldsymbol{h}^{est}_{j_{opt}}$. Ice thickness difference $\Delta \boldsymbol{h}^{mod}$ between the comprehensive GlaTE results $\boldsymbol{h}^{comp}$ and the glaciological model $\boldsymbol{h}^{mod}$ is displayed in (b).

reflections.

The ice thickness results of the glaciological mass conservation model before the adjustment were troubling, since they occasionally deviated from the GPR-derived ice thickness significantly. By adjusting the absolute thickness closer to the GPR-derived values, we were able to compensate for major disagreements in the data before applying the inversion. However, the eastern accumulation zone of the Oberaletsch Glacier (Figures 4.3c) demonstrates that the adjustment should be further improved. In the specific area, GPR-constraint data points with a large ice thickness are spatially close to areas with no GPR coverage and low ice thickness values so that the gradient is very sharp.

By further investigating the ice thickness results of the Oberaletsch Glacier calculated with the glaciological model (Figure 4.3a) and the GlaTE inversion (Figure 4.3c), it becomes apparent that the glaciological model has difficulties resolving the ice thickness in the tongue area because of the rugged, debris-covered surface. In contrast, due to the high coverage of GPR profiles, the ice thickness is significantly better resolved with the GlaTE inversion. This demonstrates how the GlaTE algorithm enhances the performance of ice thickness output for glaciers with atypical surface conditions, when GPR data is available.

The SOED analysis revealed that a very similar ice thickness in comparison to the comprehensive GlaTE results can be achieved with less than 50 % of the acquired GPR profiles. With the SOED$_{weight \times comp}$, we tested if restricting the survey layout to short GPR profiles is preferential and observed that this is not the case. Generally, no transit time in between the profiles was considered, which is a further argument towards a few longer profiles. Also, no evidence was found that a zig-zag layout along the glacier is beneficial. This can be seen on the Oberaletsch Glacier (Figure 4.8), where mostly longitudinal and perpendicular (i.e. cross) profiles to the flowline were selected with the SOED approach, when they were available. For narrow Alpine glaciers, the result on the Morteratsch Glacier (Figure 4.7) and in the Dom region (Figure 4.10) suggest that longitudinal profiles are very efficient to constrain the ice thickness. In wider sections such as saddle areas and convergence zones additional across profiles are necessary to enhance the ice thickness estimates.

If GPR data is acquired with helicopter support, incorporating the pilots skill and experience with glaciers surveys can be beneficial. Specifically longitudinal profiles can be challenging to fly, since the pilot has to estimate the ascending or descending surface slope in a usually bright, low-contrast environment.

4.7 Conclusion

The GlaTE inversion successfully derived the ice thickness for four test sites in the Swiss Alps. In comparison to the results of the glaciological mass conservation model, deeper sections of the glacier are resolved more accurately, when data constraints such as GPR-derived thickness measurements are available. Applying the GlaTE inversion to atypically shaped glacier such as the Plaine Morte Glacier or glaciers with rugged surface topography increases the quality of ice thickness estimates in contrast to the output of the mass conservation method.

Additionally, we applied our inversion approach to optimize the GPR survey layout on Alpine glaciers. The results of the SOED methods revealed that for three valley-type glaciers less than 35 % and for one plateau-shaped glacier only 46 % of the total acquired GPR profiles are required to estimate the ice thickness sufficiently. Generally, longitudinal profiles are preferred in narrow tongue sections of the glacier and additionally cross profiles are needed in saddle or convergence zones. The overall length of the individual profiles matters less, however, the transition time between far spaced profiles should be considered in survey planning to optimize the survey costs. To increase the impact of ground-truth GPR measurements on ice thickness estimations, profiles in the branched accumulation zones of wider glaciers should be recorded.

To optimize the survey layout prior to a GPR campaign, a basic glacier model could be used as a first attempt to identify the presumably deepest and structurally uneven zones in the glacier subsurface. Afterwards the GPR tracks should be planned according to the individual glacier type. If on-site or automatic processing of the GPR profiles is performed during a campaign, the SOED_{prev} method in conjunction with the GlaTE inversion can be applied to adjust the design of the survey in realtime.

Chapter 5

Conclusions

The overall aim of the work throughout the last four years was to introduce new methods and to develop surveying equipment for establishing a comprehensive overview of the current state of the remaining glacier ice mass in the Swiss Alps. For that purpose, a dual-polarization helicopter-borne GPR system was developed and successfully tested on the majority of large glaciers in Switzerland. We created an extensive GPR data processing and analyzing software package with the focus on treating helicopter-borne GPR data. Based on joint interpretation of GPR profiles and a glaciological mass conservation model, we generated detailed glacier ice thickness maps and defined a best-practice guide for helicopter-borne GPR acquisition on Alpine glaciers.

In Chapter 2, I demonstrated that the alignment of the GPR antenna dipole axes is a vital factor for recording high-quality bedrock reflection data on temperate Alpine glaciers. During the survey campaign on the Otemma Glacier, Switzerland, we operated two commercial GPR systems with three different center frequency dipole antennas to acquire ground-based across and longitudinal profiles. Additionally, the profiles were recorded twice with the dipole antenna axis either parallel or perpendicular to the flow direction of the glacier. As a result, we highlighted that the bedrock reflection amplitudes are strongly dependent on the directional alignment of the antennas; independent of the operated frequency or employed GPR system. GPR data collected with broadside antennas configurations oriented parallel to the glacier flow direction showed on average a three times higher amplitude of the bedrock reflection. A numerical modeling study with homogeneous, isotropic glacier ice and both GPR antenna axis alignments confirmed that the interaction of the dipole radiation pattern in combination with the shape of the bedrock topography governs the bedrock reflection amplitudes. For optimal GPR images of the ice-bedrock interface, the dipole axis should be aligned parallel to the strike direction of the surrounding valley walls, which in the tongue area of a valley glacier also corresponds to the flow direction of the ice. Consequently, the orientation of the GPR dipole antennas should be carefully considered during operational planning and surveying. If the general glacial subsurface topography is unknown e.g. in diverging glacier zones and saddle regions, a multicomponent antenna setup with perpendicular antenna pairs is preferable.

Based on these finding, we tested the feasibility and application of a helicopter-borne GPR system for extensive surveying in the Swiss Alps, which was presented in Chapter 3. To investigate

GPR radiation patterns for airborne GPR measurements, we carried out analytical calculations and considered numerical models. We identified that the radiation pattern of GPR dipoles do not correspond to a full space solution at low flight heights above ground (< 40 m). As a result, we developed a dual-polarization GPR system for helicopter-borne application to overcome the radiation pattern directivity issues as described in Chapter 3. The system consists of two dipole antenna pairs which are mounted perpendicular to each other, the individual pairs are placed in co-polarized, broadside configuration and operated at a low center frequency of 25 MHz. Alongside the GPR hardware, GNSS receivers and a LIDAR were attached to the system's platform. The system is fully reproducible and consists of commercially available components. Additionally, the GPR profile data were processed with optimized processing steps designed for extensive helicopter-borne acquisitions (e.g. Singular value decomposition (SVD) for signal ringing removal, reversed-time migration (RTM) to located subsurface structures accurately). To enhance the GPR data quality and decrease the influence of the directional antenna dependency, we adopted the pseudo scalar approach (Lehmann et al., 2000) by summing the data of both GPR antenna channels. The quality of the bedrock reflection varied for the individual channels due to the undulating subsurface topography, however, summing the GPR signals causes the reflections to be more coherent and steeper dipping reflectors as well as features at greater depth are captured more precisely.

In Chapter 4, we used the collected helicopter-borne GPR ice thickness measurements as a data constrain together with physical model constrains in the GlaTE inversion algorithm to derive a 3D ice thickness model. In comparison to traditional glaciological model the GlaTE inversion estimated the ice thickness more accurately, when the GPR-derived thickness values are defined as a reference. We observed that occasionally the thickness calculated with a glaciological mass conservation model deviated significantly from the GPR-derived ice thickness and therefore had to be adjusted prior to the inversion. Overall data and glaciological parameter uncertainties are accounted for by combining the individual constraints into a single set of equations to solve for the ice thickness with a given range of discrepancy. The inversion algorithm was further used to improve GPR survey layouts on Alpine glaciers. We were able to identify the most important GPR tracks which are necessary to estimate the ice thickness cost-efficiently and to a high degree of certainty by selecting individual GPR profiles with a sequential optimized experimental design algorithm. To optimize the GPR survey layout on Alpine glaciers, the acquisition focus on a few longitudinal profiles along the narrow glacier tongue and additional across profiles in broader upstream regions or converging flow zones.

From 2000 to 2017, 2033 km of GPR profiles were measured with 681 km alone in the last two years (Grab et al., 2018). In this project, we successfully produced a state of the art airborne GPR acquisition system, which is an indispensable tool to aid present and future research endeavors in the field of glaciology, geophysics, hydrology and geology. The created data base of glacier ice thickness measurements and the new inversion algorithm should be used to create a comprehensive estimation of the total glacier ice mass in the Swiss Alps to facilitate an update and refinement of the glacier inventory from 2009 (Farinotti et al., 2009a).

Chapter 6

Outlook

Even though we successfully developed and operated the dual-polarization helicopter-borne GPR system and the associated processing and modeling routines, I see several opportunities to further improve the system. In the following, I offer several recommendations to make the system and its applications more versatile.

6.1 Improvements of helicopter-borne GPR system

6.1.1 Technical modifications:

- Due to the increasing technological process, new commercial system components are available already. Recently, the manufacturer, who produced our GPR receiver, developed a new receiver model including 16 bit to 32 bit real-time sampling. Applying this new technology would allow for a higher stacking rate of GPR traces, which is a limiting factor in our acquisition. So far, we have been stacking with a factor of 2 for the helicopter-borne surveys to ensure a dense spatial sampling. The new system allows for higher stacking and therefore better penetration depth by reducing random noise. Or it could be used to increase the flight speed during the acquisition while keeping the same stacking rate. The flight speed of the helicopter can vary significantly during the surveys and usually keeping the speed below 40 km/h is challenging for the pilots.

- True multicomponent antenna setups include both cross and co-polarized configurations. So far, we acquired basic co-polarized GPR data with two perpendicular antenna sets, because we aim to have a spatial sampling below 2 m. By adding two cross-polarized transmitter-receiver channels, the time for measuring a specific location doubles. To address this issue, the helicopter could fly slower, which is rarely feasible, because the aerodynamic lift of the helicopter becomes unstable at a speed of less than 40 km/h. A further option could be the reduction of the time window. We adjust the time window according to the predicted glacier thickness, but for thick glacier systems, reducing the time window is not an option. A solution could be the faster recording of the data with an enhanced receiver as mentioned above and a comprehensive GPR multi-channel system with adjustable antenna frequency input. In the early stages of the helicopter-borne GPR system development, we utilized a multicomponent switch belonging to our commercial GPR hardware. However, it was destroyed in a crash of the helicopter-borne system and could not be re-manufactured. A combination of co- and cross polarized GPR data would enable us to perform a detailed attribute analysis of the subsurface (e.g. McClymont et al., 2008).

- Detecting off-plane reflections in the GPR profiles reliably remains an open problem. Adding a third, vertical antenna pair would enable us to truly explore the vectorial nature of the GPR wave-propagation, which could potentially localize off-plane reflections from the surrounding valley walls (Lehmann et al., 2000; Streich et al., 2006). Until now, we did not attempt an extension of the helicopter-borne GPR frame in the vertical direction, because of safety and logistical concerns.

- Our helicopter-borne GPR system is a prototype assembled from different commercially available hardware components. Additionally, we rely on an external company to store and process the GNSS data. As a consequence, GPR and GNSS data are stored and processed independently until both data sets are merged at a later stage. Assimilating the GPR setup, GNSS receiver and Laser altimeter into one consistent system would improve data and hardware standardization.

- Another adjustment can be made by applying a variety of different center frequency GPR antennas. The system has been tested with a 25 MHz antenna setup, but for penetrating deeper glaciers surveying with lower frequencies ($<$ 15 MHz) is advisable. The drawback of applying lower frequency antennas is their physical size, which will require an extension of the frame of the helicopter-borne GPR system beyond the length and width of 4 m. In contrast, higher frequency antennas are shorter and could be more easily attached to the frame. This would enable us to target shallower subsurface structures and to resolve them in more detail.

- We surveyed several larger glaciers in the Swiss Alps with the helicopter-borne GPR system, but no dedicated testing of the maximum penetration depth of the system has been carried out. Knowing the limitations of the system is specifically of interest when we are able to operate lower frequency antennas and target very thick glaciers (e.g. Great Aletsch Glacier) for airborne surveys.

- In Chapter 3, Figure 3.6 a-1 to c-1 shows the strong distortion of the received GPR signal due to ringing noise. Even though, our manual GPR processing can include wave form interpolation and selected single value decomposition (Ammann, 2017; Grab et al., 2018) to recover information from the shallower section of the subsurface, antenna shielding against ringing effects caused by the helicopter could prevent the distortion in the first place. However, antenna shielding is known to affect the antenna radiation pattern significantly, which would be undesirable for multi-component analyses, as described earlier.

- Although, the GPR system is developed for airborne applications, it could be attached to other aerial vehicles such as Unmanned Aircraft Systems (UAVs). In the near future, the current technological progress will increase the payload of drones and reduce the weight of GPR systems so that the development of an unmanned airborne GPR system could become feasible and affordable.

6.1.2 Processing routines

- Currently, we are relying on semi-automated processing of the recorded GPR data. For example, the bedrock reflection picking is performed by individuals with subjective decisions. To decrease manual labor and ensure a more objective processing, automation of the last bedrock picking step could be beneficial. It could be supported by image recognition software or self-learning algorithms.

- To further analyze the GPR data, signal attributes (e.g. instantaneous amplitude, instantaneous frequency etc.) could provide various information about the surface structure and bedrock properties. Coherency of the bedrock reflection could be a potential attribute, which indicates major reflection events (McClymont et al., 2008).

- Extra processing steps, such as applying a signal envelope routine could improve the overall detection of bedrock reflections in the GPR sections.

- Coherency-based attributes could be used for a more sophisticated combination of both transmitter and receiver channels in contrast to the summing of the data as described in Chapter 3. When both channels are summed, scattering and interfering noise are added as well. By applying attribute-based merging of the GPR traces of individual channels, high-quality and low-noise content of the GPR signal may be prioritized.

- Full-waveform inversion (FWI) could be a possible method to investigate features of particular interest, such as high backscatter zones or sections near the ice-bedrock interface.

- Lehmann et al. (2000) demonstrated that it is possible to distinguish between in- and off-plane reflections in ground-based surveys by cross-correlating co- and cross-polarized 2D GPR data sets. If the previously mentioned true multicomponent acquisition with four channels is applied, the Lehmann et al. (2000) processing approach could help to distinguish in- and off-plane reflections in our helicopter-borne GPR data. Another approach to solve these uncertainties could involve numerical waveform modeling. Initial investigations revealed that ray-based methods are inappropriate to describe the wave propagation and the amplitudes recorded in helicopter-borne GPR surveys.

- Modeling glaciers in their full extent is computationally expensive with finite-difference algorithms. More advanced algorithms and sufficient computational resources are needed in the future.

- Due to extensive measurement campaigns specifically in the last two years (Grab et al., 2018), not all GPR survey data set have been processed so far. Additional personnel should be employed to help with the extensive manual labor.

6.2 Future applications of helicopter-borne GPR

6.2.1 Survey design

- Based on the results of the sequential optimized experimental survey design study in Chapter 4, we should reconsider our planning routines prior to surveying the remaining glaciers in Switzerland. With the excess of an extensive amount of glacier outlines and high resolution DTMs, an unconstrained glaciological model could be used to identify regions of interest e.g. deep zones or rugged subsurface topography. Afterwards, the GPR profiles could be planned accordingly with a focus on longitudinal tracks in narrow glacier tongues and extended across profiles in converging flow regions.

- We extensively tested the helicopter-borne GPR system in the Swiss Alps, but it could be applied in higher elevation terrain such as the Himalayan range or the Andes as well to support local glaciological, geophysical or hydrological research. Ice caps and polar outlet glaciers of ice sheets are potential measuring sites as well. In contrast to airplane systems, helicopter-borne GPR systems, are applicable in steep and narrow regions.

- None-glaciated environments are additional potential survey sites e.g. rock glaciers (Merz et al., 2015), debris flows and rock slides (Frankenhauser, 2014), waste deposits, mining sites and sedimentary deposits.

6.2.2 Glacier investigations

- Verifying our glacier thickness results is necessary to validate our conceptual approach. Hence, the GlaTE inversion algorithm should be benchmarked against existing glaciological models as summarized in ITMIX - Ice Thickness Models Intercomparison eXperiment (Farinotti et al., 2017). Integrating our GPR data base into already existing models can improve our understanding about the fundamental differences of varying glaciological models and narrow down the best practice suitable for the Swiss Alpine glaciers.

- To increase the accuracy of our GPR-glacier-inversion model additional input data sets (e.g. surface displacement velocities, ice-bedrock interface conditions for sliding estimation) and complexity should be added.

- To date, the glacier thickness was modeled with an outline data set from 2008. The Swiss Federal Office of Topography (Swisstopo, 2018), will publish an updated version for all Swiss glaciers in the near future. Since the majority of the Alpine glaciers are retreating at high rates, our glacier thickness results should be revisited when the new outline data are available.

- In this work, I focused primarily on detecting the bedrock reflection in our GPR profiles. However, the comprehensive data set can also be used to investigate englacial features and structures such as water flow paths and pockets, ice crystal anisotropy (Hellmann et al., 2018), reflection bands (Rutishauser et al., 2016) and the ice-bedrock interface properties and sediment structures (Church et al., 2018).

- In the future, our data should be made publicly available, for example in the global data base of the World Glacier Monitoring Service (WGMS, 2018). This way, a wide range of research fields interested in Alpine environments (e.g. Geomorphology, Tectonics, Hydrology, Meteorology) could benefit from the comprehensive GPR ice thickness data set. Policy makers and governmental institutions could be provided with viable information to support future decisions processes.

References

Ammann, F. 2017. “Processing Improvements for Helicopter Borne GPR Measurements”. Master thesis, ETH Zurich.

Annan, A. P. 2009. “Electromagnetic Principles of Ground Penetrating Radar”. Chap. 1 in *Ground Penetrating Radar Theory and Applications*, ed. by H. M. Jol, 1–40. Amsterdam: Elsevier.

– . 2005. “Ground penetrating radar”. In *Near surface-geophysics*, ed. by D. K. Butler, 357–438. Tulsa, USA: Society of Exploration Geophysicists.

– . 1973. “Radio interferometry depth sounding. Part 1. Theroretical discussions”. *GEOPHYSICS* 38 (3): 557–580.

Arcone, S. A. 1995. “Numerical studies of the radiation patterns of resistively loaded dipoles”. *Journal of Applied Geophysics* 33 (1–3): 39–52.

Bamber, J. L., J. A. Griggs, R. T. W. L. Hurkmans, J. A. Dowdeswell, S. P. Gogineni, I. Howat, J. Mouginot, J. Paden, S. Palmer, E. Rignot, and D. Steinhage. 2013. “A new bed elevation dataset for Greenland”. *The Cryosphere* 7 (2): 499–510.

Bamber, J. L., and R. Kwok. 2004. “Remote-sensing techniques”. Chap. 4 in *Mass Balance of the cryosphere*, ed. by J. L. Bamber and A. J. Payne, 59–113. Cambridge: Cambridge University Press.

Bauder, A. 2015. *The Swiss glaciers 2009/2010 and 2010/2011 - Glaciological Report 131/132.* Tech. rep. ryospheric Commission (EKK) of the Swiss Academy of Sciences (SCNAT).

– . 2016. *The Swiss glaciers 2011/2012 and 2012/2013 - Glaciological Report 133/134.* Tech. rep. Cryospheric Commission (EKK) of the Swiss Academy of Sciences (SCNAT).

– . 2017. *The Swiss Glaciers 2013/2014 and 2014/2015 - Glaciological Report 135/136.* Tech. rep. Cryospheric Commission (EKK) of the Swiss Academy of Sciences (SCNAT).

Bauder, A., M. Funk, and G. H. Gudmundsson. 2003. “The ice-thickness distribution of Unteraargletscher, Switzerland”. *Annals of Glaciology* 37 (1): 331–336.

Benn, D. I., and D. J. A. Evans. 2010. *Glaciers and Glaciation.* 2nd. London: Hodder Education.

Blindow, N. 2009. “The University of Münster Airborne Ice Radar (UMAIR): Instrumentation and first results of temperate and polythermal glaciers”. In *EGU General Assembly Conference Abstracts*, 11:13619. Wien, Austria.

Blindow, N., C. Salat, and G. Casassa. 2012. “Airborne GPR sounding of deep temperate glaciers - Examples from the Northern Patagonian Icefield”. In *14th International Conference on Ground Penetrating Radar (GPR)*, 664–669. Shanghai, China.

Blindow, N., C. Salat, V. Gundelach, U. Buschmann, and W. Kahnt. 2011. “Performance and calibration of the helicoper GPR system BGR-P30”. In *6th International Workshop on Advanced Ground Penetrating Radar (IWAGPR)*, 1–5. Aachen, Germany: IEEE.

Bradford, J. H., D. F. Dickins, and P. J. Brandvik. 2010. “Assessing the potential to detect oil spills in and under snow using airborne ground-penetrating radar”. *Geophysics* 75 (2): G1–G12.

Bradford, J. H., J. Nichols, J. T. Harper, and T. Meierbachtol. 2013. “Compressional and EM wave velocity anisotropy in a temperate glacier due to basal crevasses, and implications for water content estimation”. *Annals of Glaciology* 54 (64): 168–178.

Bradford, J. H., J. Nichols, T. D. Mikesell, and J. T. Harper. 2009. “Continuous profiles of electromagnetic wave velocity and water content in glaciers: an example from Bench Glacier, Alaska, USA”. *Annals of Glaciology* 50 (51): 1–9.

Braun, L. N., M. Weber, and M. Schulz. 2000. “Consequences of climate change for runoff from Alpine regions”. *Annals of Glaciology* 31 (1): 19–25.

Brinkerhoff, D. J., A. Aschwanden, and M. Truffer. 2016. “Bayesian Inference of Subglacial Topography Using Mass Conservation”. *Frontiers in Earth Science* 4:8.

Casassa, G., J. L. Rodríguez, and N. Blindow. 2014. “Airborne GPR on high Andean glaciers - First results from 6000 m altitude”. In *Proceedings of the 15th International Conference on Ground Penetrating Radar*, 728–733. Brussels, Belgium: IEEE.

Church, G., A. Bauder, H. Maurer, and M. Grab. 2018. “High-resolution helicopter-borne ground penetrating radar survey to determine glacier base topography and the outlook of a proglacial lake”. In *17th International Conference on Ground Penetrating Radar*. Rapperswil, Switzerland.

Clarke, G. K. C., F. S. Anslow, A. H. Jarosch, V. Radić, B. Menounos, T. Bolch, and E. Berthier. 2013. “Ice Volume and Subglacial Topography for Western Canadian Glaciers from Mass Balance Fields, Thinning Rates, and a Bed Stress Model”. *Journal of Climate* 26 (12): 4282–4303.

Constable, S. C., R. L. Parker, and C. G. Constable. 1987. “Occam’s inversion: A practical algorithm for generating smooth models from electromagnetic sounding data”. *GEOPHYSICS* 52 (3): 289–300.

Conway, H., B. Smith, P. Vaswani, K. Matsuoka, E. Rignot, and P. Claus. 2009. “A low-frequency ice-penetrating radar system adapted for use from an airplane: test results from Bering and Malaspina Glaciers, Alaska, USA”. *Annals of Glaciology* 50 (51): 93–97.

Cook, J. 1960. “Proposed mono-cycle very-high-frequency radar for air-borne snow and ice measurement”. *Transaction of the American Institution for Electrical Engineering* 79 (1): 588–594.

Cuffey, K. M., and W. S. B. Paterson. 2010. *The physics of glaciers.* 4th. Amsterdam: Elsevier.

Curtis, A., A. Michelini, D. Leslie, and A. Lomax. 2004. “A deterministic algorithm for experimental design applied to tomographic and microseismic monitoring surveys”. *Geophysical Journal International* 157 (2): 595–606.

Deutsch, C. V., and A. G. Journel. 1992. *GSLIB: Geostatistical Software Library and User’s Guide.* New York: Oxford University press.

DeWalle, D. R., and A. Rango. 2008. *Principles of snow hydrology.* 1st. New York: Cambridge University Press.

Diamanti, N., and A. P. Annan. 2013. “Characterizing the energy distribution around GPR antennas”. *Journal of Applied Geophysics* 99:83–90.

Dobhal, D. P. 2014. “Glacier”. In *Encyclopedia of Snow, Ice and Glaciers*, ed. by J. Shroder, V. Singh, and U. Haritashya, 376–377. Springer.

Drews, R., O. Eisen, I. Hamann, S. Kipfstuhl, a. Lambrecht, D. Steinhage, F. Wilhelms, and H. Miller. 2009. “Layer disturbances and the radio-echo free zone in ice sheets”. *The Cryosphere Discussions* 3 (1): 307–321.

Drews, R., O. Eisen, D. Steinhage, I. Weikusat, S. Kipfstuhl, and F. Wilhelms. 2012. “Potential mechanisms for anisotropy in ice-penetrating radar data”. *Journal of Glaciology* 58 (209): 613–624.

Dunse, T., T. V. Schuler, J. O. Hagen, T. Eiken, O. Brandt, and K. A. Hogda. 2009. “Recent fluctuations in the extent of the firn area of Austfonna, Svalbard, inferred from GPR”. *Annals of Glaciology* 50 (50): 155–162.

EDA Präsenz Schweiz. 2017. *Geografie – Fakten und Zahlen: https://www.eda.admin.ch/ aboutswitzerland/ de/ home/.* Visited on 05/30/2018.

Eisen, O., A. Bauder, M. Lüthi, P. Riesen, and M. Funk. 2009. “Deducing the thermal structure in the tongue of Gornergletscher, Switzerland, from radar surveys and borehole measurements”. *Annals of Glaciology* 50 (51): 63–70.

Eisenburger, D., H. Lentz, and M. Jenett. 2008. “Helicopter-Borne GPR Systems: a Way From Ice Thickness Measurements To Geological Applications”. In *IEEE International Conference on Ultra-Wideband*, 3:161–165. Hannover, Germany: IEEE.

Engheta, N., C. H. Papas, and C. Elachi. 1982. “Radiation patterns of interfacial dipole antennas”. *Radio Science* 17 (6): 1557–1566.

Evans, S. 1963. "Radio techniques for the measurement of ice thickness". *Polar Record* 11:406–410.

Evans, S., D. J. Drewry, and G. d. Q. Robin. 1972. "Radio-echo sounding in Antarctica, 1971-1972". *Polar Record* 16 (101): 207–12.

Farinotti, D., D. J. Brinkerhoff, G. K. C. Clarke, J. J. Fürst, H. Frey, P. Gantayat, F. Gillet-Chaulet, C. Girard, M. Huss, P. W. Leclercq, A. Linsbauer, H. Machguth, C. Martin, F. Maussion, M. Morlighem, C. Mosbeux, A. Pandit, A. Portmann, A. Rabatel, R. Ramsankaran, T. J. Reerink, O. Sanchez, P. A. Stentoft, S. Singh Kumari, W. J. J. van Pelt, B. Anderson, T. Benham, D. Binder, J. A. Dowdeswell, A. Fischer, K. Helfricht, S. Kutuzov, I. Lavrentiev, R. McNabb, G. H. Gudmundsson, H. Li, and L. M. Andreassen. 2017. "How accurate are estimates of glacier ice thickness? Results from ITMIX, the Ice Thickness Models Intercomparison eXperiment". *The Cryosphere* 11 (2): 949–970.

Farinotti, D., M. Huss, A. Bauder, and M. Funk. 2009a. "An estimate of the glacier ice volume in the Swiss Alps". *Global and Planetary Change* 68 (3): 225–231.

Farinotti, D., M. Huss, A. Bauder, M. Funk, and M. Truffer. 2009b. "A method to estimate the ice volume and ice-thickness distribution of alpine glaciers". *Journal of Glaciology* 55 (191): 422–430.

Farinotti, D., S. Usselmann, M. Huss, A. Bauder, and M. Funk. 2012. "Runoff evolution in the Swiss Alps: projections for selected high alpine catchments based on ENSEMBLES scenarios". *Hydrological Processes* 26 (13): 1909–1924.

Feiger, N., M. Huss, S. Leinss, L. Sold, and D. Farinotti. 2018. "The bedrock topography of Gries- and Findelengletscher". *Geographica Helvetica* 73 (1): 1–9.

Finger, D., G. Heinrich, A. Gobiet, and A. Bauder. 2012. "Projections of future water resources and their uncertainty in a glacierized catchment in the Swiss Alps and the subsequent effects on hydropower production during the 21st century". *Water Resources Research* 48 (2): W02521.

Fischer, M., M. Huss, C. Barboux, and M. Hoelzle. 2014. "The New Swiss Glacier Inventory SGI2010: Relevance of Using High-Resolution Source Data in Areas Dominated by Very Small Glaciers". *Arctic, Antarctic, and Alpine Research* 46 (4): 933–945.

Forte, E., M. Dossi, M. C. Fontana, and R. R. Colucci. 2014. "4-D quantitative GPR analyses to study the summer mass balance of a glacier: a case history". In *Proceedings of the 15th International Conference on Ground Penetrating Radar*, 352–356. IEEE.

Fountain, A. 2014. "Temperate Glaciers". In *Encyclopedia of Snow, Ice and Glaciers*, ed. by J. Shroder, V. Singh, and U. Haritashaya, 1145. Springer.

Fowler, A. C., and D. A. Larson. 1978. “On the flow of polythermal glaciers - I. Model and preliminary analysis”. *Proceedings of the Royal Society of London A: Mathematical, Physical and Engineering Sciences* 363 (1713): 217–242.

Frankenhauser, K. 2014. “Geophysical Slope Characterization Using GPR and ERT in an Active Debris Flow Catchment”. Master Thesis, ETH Zürich.

Frey, H., H. Machguth, M. Huss, C. Huggel, S. Bajracharya, T. Bolch, A. Kulkarni, A. Linsbauer, N. Salzmann, and M. Stoffel. 2014. “Estimating the volume of glaciers in the Himalayan-Karakoram region using different methods”. *The Cryosphere* 8 (6): 2313–2333.

Gabbi, J., D. Farinotti, A. Bauder, and H. Maurer. 2012. “Ice volume distribution and implications on runoff projections in a glacierized catchment”. *Hydrology and Earth System Sciences* 16 (12): 4543–4556.

Gabbud, C., S. Rüttimann, N. Micheletti, J. Irving, and S. Lane. 2015. “Analysis of subglacial hydrodynamics and ice dynamics through combined terrestrial laser scanning and ground penetrating radar survey”. In *EGU General Assembly Conference Abstracts*, 17:9040. Wien, Austria.

Gacitúa, G., J. A. Uribe, R. Wilson, T. Loriaux, J. Hernández, and A. Rivera. 2015. “50 MHz helicopter-borne radar data for determination of glacier thermal regime in the central Chilean Andes”. *Annals of Glaciology* 56 (70): 193–201.

Gantayat, P., A. Kulkarni, and J. Srinivasan. 2014. “Estimation of ice thickness using surface velocities and slope: case study at Gangotri Glacier, India”. *Journal of Glaciology* 60 (220): 277–282.

Garambois, S., C. Vincent, A. Legchenko, and E. Thibert. 2015. “A combined GPR and SNMR monitoring of a drained intraglacial water pocket located into the polythermal glacier of Tete Rousse”. In *2015 8th International Workshop on Advanced Ground Penetrating Radar (IWAGPR)*, 1–4. Florence, Italy.

Geophysical Survey Systems Inc. 2016. *http://www.geophysical.com/*. Visited on 02/01/2016.

– . 2017. *http://www.geophysical.com/*. Visited on 08/14/2017.

Giannopoulos, A. 2005. “Modelling ground penetrating radar by GprMax”. *Construction and Building Materials* 19 (10): 755–762.

Godio, A., and R. B. Rege. 2016. “Analysis of georadar data to estimate the snow depth distribution”. *Journal of Applied Geophysics* 129:92–100.

Grab, M., A. Bauder, F. Ammann, L. Langhammer, S. Hellmann, G. Church, L. Schmid, L. Rabenstein, and H. Maurer. 2018. “Ice volume estimates of Swiss glaciers using helicopter-borne GPR – an example from the Glacier de la Plaine Morte”. In *17th International Conference on Ground Penetrating Radar.* Rapperswil, Switzerland.

Graham, A. G. C. 2011. “Ice Sheet”. In *Encyclopedia of snow, ice and glaciers*, ed. by J. Shroder, V. Singh, and U. Haritashya, 592–607. Springer.

Grimm, R. E., D. E. Stillman, and J. A. MacGregor. 2015. “Dielectric signatures and evolution of glacier ice”. *Journal of Glaciology* 61 (230): 1159–1170.

Gudmundsson, G. H. 1999. “A three-dimensional numerical model of the confluence area of Unteraargletscher, Bernese Alps, Switzerland”. *Journal of Glaciology* 45 (150): 219–230.

Haeberli, W., and M. Beniston. 1998. “Climate Change and Its Impacts on Glaciers and Permafrost in the Alps”. *Ambio* 27 (4): 258–265.

Hagen, J. O., and N. Reeh. 2004. “In situ measurements technigues: land ice”. Chap. 1 in *Mass Balance of the Cryosphere: Observations and modelling of contemporary and future changes*, ed. by J. L. Bamber and A. J. Payne, 11–43. Cambridge: Cambridge University Press.

Harrison, C. 1970. “Reconstruction of subglacial relief from radio echo sounding records”. *GEOPHYSICS* 35 (6): 1099–1115.

Hellmann, S., P.-L. Giertzuch, M. Grab, A. Bauder, and H. Maurer. 2018. “Enhancing crosshole GPR data by analysing travel time differences of reciprocal tomographic measurements”. In *Near Surface Geoscience Conference & Exhibition 2018 - 24th European Meeting of Environmental and Engineering Geophysics*, in press.

Hirt, C. 2014. “GOCE’s view below the ice of Antarctica: Satellite gravimetry confirms improvements in Bedmap2 bedrock knowledge”. *Geophysical Research Letters* 41 (14): 5021–5028.

Hubbard, A., H. Blatter, P. Nienow, D. Mair, and B. Hubbard. 1998. “Comparison of a three-dimensional model for glacier flow with field data from Haut Glacier d’Arolla, Switzerland”. *Journal of Glaciology* 44 (147): 368–378.

Huss, M., and D. Farinotti. 2012. “Distributed ice thickness and volume of all glaciers around the globe”. *Journal of Geophysical Research* 117 (F4): F04010.

Jouvet, G., M. Huss, M. Funk, and H. Blatter. 2011. “Modelling the retreat of Grosser Aletschgletscher, Switzerland, in a changing climate”. *Journal of Glaciology* 57 (206): 1033–1045.

Kamb, B., and K. A. Echelmeyer. 1986. “Stress-Gradient Coupling in Glacier Flow: I. Longitudinal Averaging of the Influence of Ice Thickness and Surface Slope”. *Journal of Glaciology* 32 (111): 267–284.

Kennett, M., T. Laumann, and C. Lund. 1993. “Helicopter-borne radio-echo sounding of Svartisen, Norway”. *Annals of Glaciology* 17:23–26.

Kim, J.-H., S.-J. Cho, and M.-J. Yi. 2007. “Removal of ringing noise in GPR data by signal processing”. *Geosciences Journal* 11 (1): 75–81.

Krellmann, Y., and G. Triltzsch. 2012. “HERA-G — A new helicopter GPR based on gated stepped frequency technology”. In *14th International Conference on Ground Penetrating Radar*, 156–159. Shanghai, China.

Lampe, B., and K. Holliger. 2005. “Resistively loaded antennas for ground-penetrating radar: A modeling approach”. *GEOPHYSICS* 70 (3): K23–K32.

Lampe, B., K. Holliger, and A. G. Green. 2003. “A finite difference time domain simulation tool for ground-penetrating radar antennas”. *GEOPHYSICS* 68 (3): 971–987.

Langhammer, L., L. Rabenstein, A. Bauder, and H. Maurer. 2017. “Ground-penetrating radar antenna orientation effects on temperate mountain glaciers”. *Geophysics* 82 (3): H15–H24.

Lapazaran, J., J. Otero, A. Martín-Espanõl, and F. J. Navarro. 2016. “On the errors involved in ice-thickness estimates I: ground-penetrating radar measurement errors”. *Journal of Glaciology* 62 (236): 1008–1020.

Lehmann, F., D. E. Boerner, K. Holliger, and A. G. Green. 2000. “Multicomponent georadar data: Some important implications for data acquisition and processing”. *GEOPHYSICS* 65 (5): 1542–1552.

Leica Geosystems. 2016. *http://www.leica-geosystems.com*. Visited on 02/10/2016.

Li, J., J. Paden, C. J. Leuschen, F. Rodriguez-Morales, R. D. Hale, E. J. Arnold, R. Crowe, D. Gomez-Garcia, and P. Gogineni. 2013. “High-Altitude Radar Measurements of Ice Thickness Over the Antarctic and Greenland Ice Sheets as a Part of Operation IceBridge”. *IEEE Transactions on Geoscience and Remote Sensing* 51 (2): 742–754.

Linsbauer, A., F. Paul, and W. Haeberli. 2012. “Modeling glacier thickness distribution and bed topography over entire mountain ranges with GlabTop: Application of a fast and robust approach”. *Journal of Geophysical Research: Earth Surface* 117 (F3).

Linsbauer, A., F. Paul, M. Hoelzle, H. Frey, and W. Haeberli. 2009. “The Swiss Alps without glaciers - a GIS-based modelling approach for reconstruction of glacier beds”. *Proceedings of Geomorphometry*: 243–247.

Linsbauer, A., F. Paul, H. Machguth, and W. Haeberli. 2013. “Comparing three different methods to model scenarios of future glacier change in the Swiss Alps”. *Annals of Glaciology* 54 (63): 241–253.

Maisch, M., A. Wipf, B. Denneler, J. Battaglia, and C. Benz. 2000. “Die Gletscher der Schweizer Alpen: Gletscherhochstand 1850, Aktuelle Vergletscherung, Gletscherschwundszenarien”. *Schlussbericht NFP 31* (Zurich, Switzerland): 373.

Margrave, G. F. 2003. “Numerical methods of exploration seismology with algorithms in Matlab”. PhD thesis, The University of Calgary.

Martín-Espanõl, A., J. Lapazaran, J. Otero, and F. J. Navarro. 2016. “On the errors involved in ice-thickness estimates III: error in volume”. *Journal of Glaciology* 62 (236): 1030–1036.

Matsuoka, K., D. Power, S. Fujita, and C. F. Raymond. 2012a. “Rapid development of anisotropic ice-crystal-alignment fabrics inferred from englacial radar polarimetry, central West Antarctica”. *Journal of Geophysical Research* 117 (F03029): 1–16.

Matsuoka, K., J. A. MacGregor, and F. Pattyn. 2012b. “Predicting radar attenuation within the Antarctic ice sheet”. *Earth and Planetary Science Letters* 359-360:173–183.

Maurer, H., and A. Bauder. 2013. “Helicopter-borne ground penetrating radar investigations on temperate alpine glaciers”. In *Processing SEG workshop on Cryosphere Geophysics.* Boise, USA.

Maurer, H., A. Curtis, and D. E. Boerner. 2010. “Recent advances in optimized geophysical survey design”. *GEOPHYSICS* 75 (5): 75A177–75A194.

Maurer, H., A. Nuber, N. K. Martiartu, F. Reiser, C. Boehm, E. Manukyan, C. Schmelzbach, and A. Fichtner. 2017. “Chapter One - Optimized Experimental Design in the Context of Seismic Full Waveform Inversion and Seismic Waveform Imaging”. In *Advances in Geophysics*, ed. by L. Nielsen, 58:1–45. Advances in Geophysics. Elsevier.

Maussion, F., A. Butenko, J. Eis, K. Fourteau, A. H. Jarosch, J. Landmann, F. Oesterle, B. Recinos, T. Rothenpieler, A. Vlug, C. T. Wild, and B. Marzeion. 2018. “The Open Global Glacier Model (OGGM) v1.0”. *Geoscientific Model Development Discussions* 2018:1–33.

McClymont, A. F., A. G. Green, R. Streich, H. Horstmeyer, J. Tronicke, D. C. Nobes, J. Pettinga, J. Campbell, and R. Langridge. 2008. “Visualization of active faults using geometric attributes of 3D GPR data: An example from the Alpine Fault Zone, New Zealand”. *GEOPHYSICS* 73 (2): B11–B23.

Menke, W., and Z. Eilon. 2015. “Relationship Between Data Smoothing and the Regularization of Inverse Problems”. *Pure and Applied Geophysics* 172 (10): 2711–2726.

Merz, K., H. Maurer, T. Buchli, H. Horstmeyer, A. G. Green, and S. M. Springman. 2015. “Evaluation of Ground-Based and Helicopter Ground-Penetrating Radar Data Acquired Across an Alpine Rock Glacier”. *Permafrost and Periglacial Processes* 26:13–27.

Moran, M. L., R. J. Greenfield, S. A. Arcone, and A. J. Delaney. 2000. “Delineation of a complexly dipping temperate glacier bed using short-pulse radar arrays”. *Journal of Glaciology* 46 (153): 274–286.

Moran, M. L., R. J. Greenfield, and S. A. Arcone. 2003. “Modeling GPR radiation and reflection characteristics for a complex temperate glacier bed”. *GEOPHYSICS* 68 (2): 559–565.

Morlighem, M., E. Rignot, J. Mouginot, H. Seroussi, and E. Larour. 2014. “High-resolution ice-thickness mapping in South Greenland”. *Annals of Glaciology* 55 (67): 64–70.

Morlighem, M., E. Rignot, H. Seroussi, E. Larour, H. Ben Dhia, and D. Aubry. 2011. “A mass conservation approach for mapping glacier ice thickness”. *Geophysical Research Letters* 38 (19).

Müller, F., T. Caflisch, and G. Müller. 1976. *Firn und Eis der Schweizer Alpen: Gletscherinventar.* Tech. rep. Geographisches Institut der ETH Zürich.

Murray, T., G. W. Stuart, M. Fry, N. H. Gamble, and M. D. Crabtree. 2000. “Englacial water distribution in a temperate glacier from surface and borehole radar velocity analysis”. *Journal of Glaciology* 46 (154).

Nobes, D. C. 2014. “Ground Penetrating Radar Measurements Over Glaciers”. In *Encyclopedia of Snow, Ice and Glaciers*, ed. by V. Singh, P. Singh, and U. Haritashya, 490–503. Springer.

– . 1999. “The directional dependence of Ground Penetrating Radar response on the accumulation zones of temperate Alpine glaciers”. *First Break* 17 (7): 249–259.

Nobes, D. C., and A. P. Annan. 2000. “"Broadside" versus "end-fire" radar response: some simple illustrative examples”. In *Eighth International Conference on Ground Penetrating Radar*, 4084:696–701. Gold Coast, Australia.

Oerlemans, J., B. Anderson, A. Hubbard, P. Huybrechts, T. Johannesson, W. H. Knap, M. Schmeits, A. P. Stroeven, R. S. W. Van de Wal, and J. Wallinga. 1998. “Modelling the response of glaciers to climate warming”. *Climate dynamics* 14 (4): 267–274.

Paige, C. C., and M. A. Saunders. 1982. “LSQR: An Algorithm for Sparse Linear Equations and Sparse Least Squares”. *ACM Transactions on Mathematical Software (TOMS)* (New York, NY, USA) 8 (1): 43–71.

Paul, F., C. Huggel, and A. Kääb. 2004. “Combining satellite multispectral image data and a digital elevation model for mapping debris-covered glaciers”. *Remote Sensing of Environment* 89:510–518.

Pfammatter, R., and M. Piot. 2014. *Situation und Perspektiven der Schweizer Wasserkraft.* Tech. rep. 1. Wasser Energie Luft - Schweizerischer Wasserwirtschaftsverband.

Plewes, L. A., and B. Hubbard. 2001. “A review of the use of radio-echo sounding in glaciology”. *Progress in Physical Geography* 25 (2): 203–236.

Polom, U., C. Hofstede, A. Diez, and O. Eisen. 2014. “First glacier-vibroseismic experiment – results from cold firn of Colle Gnifetti”. *Near Surface Geophysics* 12:493–504.

Radarteam Sweden AB. 2017. *http://www.radarteam.se/*.

Rebetez, M., and M. Reinhard. 2007. “Monthly air temperature trends in Switzerland 1901–2000 and 1975–2004”. *Theoretical and Applied Climatology* 91 (1): 27–34.

Reynolds, J. M. 2011. *An Introduction to Applied and Environmental Geophysics*. 2nd. Wiley-Blackwell.

Richardson, S. D., and J. M. Reynolds. 2000. “An overview of glacial hazards in the Himalayas”. *Quaternary International* 65:31–47.

Rückamp, M., and N. Blindow. 2012. “King George Island ice cap geometry updated with airborne GPR measurements”. *Earth System Science Data* 4 (1): 23–30.

Rutishauser, A. 2013. “Analysis of different helicopter-borne GPR systems on temperate alpine glaciers”. Master thesis, ETH Zurich.

Rutishauser, A., H. Maurer, and A. Bauder. 2016. “Helicopter-borne ground-penetrating radar investigations on temperate alpine glaciers: A comparison of different systems and their abilities for bedrock mapping”. *Geophysics* 81 (1): WA119–WA129.

Ryser, C., M. Lüthi, N. Blindow, S. K. Suckro, M. Funk, and A. Bauder. 2013. “Cold ice in the ablation zone: Its relation to glacier hydrology and ice water content”. *Journal of Geophysical Research: Earth Surface* 118 (2): 693–705.

Saetrang, A., and B. Wold. 1986. “Results from the Radio Echo-Sounding on Parts of the Jostedalsbreen Ice Cap, Norway”. *Annals of Glaciology* 8:156–158.

Schaefli, B., B. Hingray, and A. Musy. 2007. “Climate change and hydropower production in the Swiss Alps: quantification of potential impacts and related modelling uncertainties”. *Hydrology and Earth System Sciences Discussions* 11 (3): 1191–1205.

Schwanghart, W., and D. Scherler. 2014. “Short Communication: TopoToolbox 2 – MATLAB-based software for topographic analysis and modeling in Earth surface sciences”. *Earth Surface Dynamics* 2 (1): 1–7.

Sensors & Software. 2016. *http://www.sensoft.ca/*. Visited on 02/01/2016.

– . 2017. *http://www.sensoft.ca/*.

Shi, L., C. T. Allen, J. R. Ledford, F. Rodriguez-Morales, W. A. Blake, B. G. Panzer, S. C. Prokopiack, C. J. Leuschen, and S. Gogineni. 2010. "Multichannel Coherent Radar Depth Sounder for NASA Operation Ice Bridge". In *2010 IEEE International Geoscience and Remote Sensing Symposium*, 1729–1732. Honolulu, USA.

Sigurðsson, O. 2018. *Glacier Sketch - Solheimajokull https:// www.discover-the-world.co.uk/ study-trips/ iceland/ solheimajokull-geography-case-study.* Visited on 05/25/2018.

Steenson, B. 1951. "Radar methods for the exploration of glaciers". Unpublished Ph.D. thesis, Californian Institute of Technology, Pasedena, USA.

Streich, R. 2007. "Accurate 3-D imaging of ground-penetrating radar data based on exact-field radiation patterns". PhD Thesis, ETH Zürich.

Streich, R., and J. Van der Kruk. 2007. "Accurate imaging of Multicomponent GPR data based on exact radiation patterns". *IEEE Transactions on Geoscience and Remote Sensing* 45 (1): 93–103.

Streich, R., J. Van der Kruk, and A. G. Green. 2006. "Three-dimensional multicomponent georadar imaging of sedimentary structures". *Near Surface Geophysics* 4 (1): 39–48.

Stummer, P., H. Maurer, and A. G. Green. 2004. "Experimental design: Electrical resistivity data sets that provide optimum subsurface information". *GEOPHYSICS* 69 (1): 120–139.

Swisstopo. 2018. *https://www.swisstopo.admin.ch/de/home.html.* Visited on 06/20/2018.

Takei, I. 2007. "Dielectric relaxation of ice samples grown from vaporphase or liquid-phase water". In *Physics and Chemistry of Ice: proceedings of the 11th International Conference on the Physics and Chemistry of Ice*, ed. by W. F. Kuhs, 577. Bremerhaven, Germany: The Royal Society of Chemistry.

Urbini, S., A. Zirizzotti, J. Baskaradas, I. Tabacco, L. Cafarella, A. Senese, C. Smiraglia, and G. Diolaiuti. 2017. "Airborne Radio Echo Sounding (RES) measures on Alpine Glaciers to evaluate ice thickness and bedrock geometry: preliminary results from pilot tests performed in the Ortles Cevedale Group (Italian Alps)." *Annals of Geophysics* 60 (2): 226.

Van den Broeke, M. R. 1997. "Momentum, heat, and moisture budgets of the katabatic wind layer over a midlatitude glacier in summer". *Journal of Applied Meteorology* 36 (6): 763–774.

Van der Kruk, J. 2004. "Three-dimensional GPR imaging in the horizontal wavenumber domain for different heights of source and receiver antennae". *Near Surface Geophysics* 2 (1): 25–31.

– . 2001. "Three-dimensional imaging of multi-component ground penetrating radar data". PhD Thesis, Delft University of Technology.

Van der Kruk, J., C. P. A. Wapenaar, J. T. Fokkema, and P. M. van den Berg. 2003. “Improved Three-Dimensional Image Reconstruction Technique for Multi-Component Ground Penetrating Radar Data”. *Subsurface Sensing Technologies and Applications* 4 (1): 61–99.

Waite, A. H., and S. J. Schmidt. 1962. “Gross errors in height indi- cation from pulsed radar altimeters operating over thick ice or snow”. *Proceedings of the Institute of Radio Engineers (IRE)* 50:1515–1520.

Watts, R. D., and D. L. Wright. 1981. “Systems for measuring thickness of temperate and polar ice from the ground or from the air.” *Journal of Glaciology* 27 (97): 459–469.

WGMS. 2018. *https://wgms.ch/*. Visited on 06/22/2018.

Woodward, J., and M. J. Burke. 2007. “Applications of Ground-Penetrating Radar to Glacial and Frozen Materials”. *Journal of Environmental and Engineering Geophysics* 12 (1): 69–85.

Zamora, R., D. Ulloa, G. Garcia, R. Mella, J. A. Uribe, J. Wendt, A. Rivera, G. Gacitúa, and G. Casassa. 2009. “Airborne radar sounder for temperate ice: Initial results from Patagonia”. *Journal of Glaciology* 55 (191): 507–512.

Zekollari, H., P. Huybrechts, J. Fürst, O. Rybak, and O. Eisen. 2013. “Calibration of a higher-order 3-D ice-flow model of the Morteratsch glacier complex, Engadin, Switzerland”. *Annals of Glaciology* 54 (63): 343–351.